universität wien

DISSERTATION

Titel der Dissertation

Bose-Einstein condensation of metastable helium-4 for quantum entanglement experiments

verfasst von

Mateusz Kotyrba, MSc

angestrebter akademischer Grad

Doktor der Naturwissenschaften (Dr. rer.nat.)

Wien, 2015

Studienkennzahl lt. Studienblatt:	A 791 411
Dissertationsgebiet lt. Studienblatt:	Physik
Betreuerin / Betreuer:	o. Univ. Prof. DDr.h.c. Anton Zeilinger

To Katarzyna.

Zusammenfassung

Gegenstand dieser Arbeit ist die experimentelle Realisierung eines Bose-Einstein Kondensats (BEK) mit Helium-4 Atomen. Wegen der elektronischen Struktur des Helium-Atoms müssen die standard Einfangstechniken der neutralen Atomen gegenüber anderer atomaren Spezies angepasst werden, um das Bose-Einstein Kondensat aus Helium zu erzeugen. Helium muss in den metastabilen Zustand angeregt werden, dann wird der Atomstrahl kollimiert und abgebremst. Wir fangen ca. 10^9 Atome in einer magneto-optischen Falle. Um die Atome weiter kühlen zu können, werden sie in eine reine magnetische Falle übertragen. Doppler-Kühlung kühlt die Atome in der Magnetfalle weiter, und erhöht die Phasenraumdichte. Der entartete Quantenzustand wird durch Verdampfungskühlung der Helium Atome erreicht. Der Übergang zum BEK findet bei ca. $T_c = 1.4\,\mu\mathrm{K}$ statt und meistens erzeugen wir Kondensate mit ein paar 10^6 Atomen.

Im Vergleich zu den anderen Atomsorten hat metastabiles Helium eine einzigartig hohe interne Energie (19.8 eV), die für eine Detektion von einzelnen Atomen ausgenutzt werden kann. Ein Detektor, der diese hohe Energie ausnutzt, besteht aus Mikrokanalplatte in Kombination mit einer Verzögerungsleitung. Wir haben einen solchen Detektor in unserer Vakuumkammer erfolgreich eingebaut, und haben damit die Atomwolke charakterisiert. Der Detektor kann die Atome mit hoher Effizienz aufzeichnen und im Vergleich zu anderen Helium Experimenten hat er die höchste Auflösung. Bestehend aus vier Quadranten mit unabhängiger Ausleseelektronik, die die Aufzeichnung von gleichzeitgen Ereignissen ermöglichen, ist der Detektor besonders für Experimente, die analog zum Feld von Quantenoptik realisiert werden, geeignet. Ein Musterbeispiel ist die Erzeugung von verschränkten Teilchen im Impuls Freiheitsgrad.

Der vorgestellte experimentelle Vorgang in dieser Dissertation stellt einen wichtigen Schritt in der Herstellung von Impulsverschränkten Atomen dar. Dieser Aufbau wird den Weg für Materiewellen Experimente, die die Besonderheiten der Quantenkorrelationen ausnutzen, bahnen. Wir erwarten, dass unserer Aufbau eine direkte Demonstration von Impulsverschränkung im Sinne des Gedankenexperiments von Einstein, Podolski und Rosen ermöglicht.

Abstract

In this thesis, I report on the realisation of a Bose-Einstein condensate (BEC) of metastable helium-4 atoms. Due to the electronic structure of helium atoms, standard trapping techniques of neutral atoms have to be adapted to generate a helium BEC. Helium has to be excited to its metastable state in a dc-discharge source, afterwards the atomic beam is collimated and slowed. We then trap several 10^8 atoms in a magneto-optical trap. For subsequent evaporative cooling, the atoms are transferred into a magnetic trap. In the magnetic trap Doppler cooling reduces further the temperature of the cloud and increases its phase-space density. Degeneracy is achieved after forced radio-frequency evaporation. The transition to the BEC occurs around a temperature of $T_c = 1.4\,\mu\mathrm{K}$ and we routinely produce condensate consisting of typically a few 10^6 atoms.

Compared to all other atomic species metastable helium has an extraordinarily large internal energy (19.8 eV) which can be used for single-atom detection. A detector that utilises energy from impinging particles is called a microchannel-plate detector. Such a detector was installed in the system and was used for characterisation of our cloud. It can detect helium atoms with high efficiency and state-of-the-art resolution. Consisting of four quadrants with independent read-out electronics that allow for true simultaneous detection of atoms, the detector is especially suited to perform experiments with ultra-cold atoms that are analogue to quantum optics experiments. One of these would be generation of momentum entangled atoms.

The experimental steps presented in this thesis represent a significant step towards production of momentum entangled atoms that will pave the way to matter-wave experiments exploiting the peculiarities of quantum correlations. We expect our setup to allow for the direct demonstration of momentum entanglement in a scenario equivalent to the Einstein, Podolsky and Rosen gedankenexperiment.

Acknowledgements

During the years at IQOQI I had pleasure to meet many exceptional people. While some of them directly contributed to my work, others have made life outside the lab worth living.

First of all I would like to thank my family, my wife Katarzyna for her patience and understanding for my work. She is the one who always stood by my side for good or bad. My parents, Elżbieta and Marian, and my sisters, Joanna, Małgorzata and Karolina who aided me to heal my wounds, provided me with Silesian delicacies and were always ready to help me.

I would like to express my gratitude Prof. Anton Zeilinger for teaching me the ways of looking at physics and his enthusiasm towards it. I value every discussion we had, about physics or general matters of life. The faith he had in every one of us to achieve our goals is what made us believe that we actually might. I would like to thank Markus Arndt, who even though was not directly involved in the project provided us with advices and cared for us as for his own students.

Many thanks go to the helium crew, its first members Maximilian Ebner, Florian Leupold and Michael Keller, with whom I had pleasure building the machine, as well as to the new members Mario Rusev and Mariusz Semczuk who joined us recently and brought fresh energy to drive it forward. I am extremely grateful to Mandip Singh who joined us as a postdoc in the crucial moment of the project. He is an exceptional teacher and a great scientist. The time he spent with us was invaluable.

I would like to thank all of the IQOQI members for the amazing work atmosphere that they created, fellow students from University of Vienna and CoQuS with whom I had many discussions over the bubbling golden liquid. I am extremely thankful to our invaluable technician Roland Blach whose imagination is infinite and who made wonders in the machine shop.

This work would not have been possible without the funding support of the University of Vienna, Austrian Academy of Sciences (ÖAW) and the Austrian Science Fund (FWF) which funded CoQuS Doctoral Programme (Grant No. W 1210) and Special Research Programme (SFB F 4007).

At last, I would like to thank all of the Liechtenstein family—Aulde, Ela, Magdalena, Petra, Rina, Fabio and Kerem—for all the memorable parties, dinners and movies nights. I owe a lot to Okinawa Sushi that provided me with necessary nourishment at any time of night or day, when time was scarce and I did not have time to cook.

Contents

CHAPTER 1

Introduction

At the beginning of the 20th century two revolutionary theories were formulated. On one hand there was the theory of relativity and on the other quantum mechanics. The beginning of quantum mechanics is marked by the pioneering work by Planck trying to explain black-body radiation by discrete portions of energy. His idea was then developed further by Einstein who introduced a concept of a light quantum—a photon—and he applied it to the explanation of the photoelectric effect for which he received the 1921 Nobel Prize in Physics. The idea of energy quantisation has been further developed by Niels Bohr who applied it to the model of atom, thereby explaining the stability of atoms as well as existence of atomic spectral lines. In 1924, based on the Compton effect, Louis de Broglie formulated a hypothesis that all objects—including matter—have a wavelength and can interfere. In the following years, the Pauli exclusion principle was formulated and Bose-Einstein and Fermi-Dirac statistics were derived. At this point a consistent mathematical formulation was needed. It was developed independently by Heisenberg and Schrödinger.

Even though nowadays many devices that we use, e.g. ticket vending machines, smartphones, GPS satellites etc., make use of quantum physics, the full potential of this field has not been exploited yet. Quantum entanglement in particular promises to deliver new technology with its applications in metrology, information science and communication. Entanglement was identified as a fundamental feature of the foundations of quantum mechanics in the seminal paper by Einstein, Podolsky and Rosen (EPR) [1] and by Schrödinger [2, 3]. After John Bell had introduced in 1964 [4]—based on the EPR paper—the notion of local realism, it became apparent that the EPR paper is in conflict with quantum mechanics. It was then possible to test the validity of quantum mechanics using various systems [5–7]. The most significant discovery happened in the 1990s when entanglement was identified as an important ingredient in many quantum information protocols [8]. All this has resulted in the burgeoning field of quantum information science. Entanglement has been proven in numerous systems, e.g. ions [9, 10], superconducting qubits [11], hot [12] and cold atomic ensembles [13] and photons [14]. However, the original states as proposed by Einstein, Podolsky and Rosen, still await their experimental realisation. The EPR argument involves entanglement, both of position and momentum, of freely moving massive particles. As suggested by Perrin et al. [15], the realisation of such states should be possible using Bose-Einstein condensate (BEC) of metastable helium and single-atom detection techniques.

The Bose-Einstein condensate (BEC) was discovered in 1925 when Bose and Einstein predicted that at extremely low temperatures identical particles with integer spin will

collapse into a single quantum state forming a new state of matter. Following the development of the necessary experimental laser-cooling techniques, the first realisation of a BEC came about 70 years after the inception of the idea [16–18]. Since then the field of dilute atomic gases has grown substantially and has opened up the possibility of novel research in many areas of physics. Among numerous developments, it has enabled studies of condensed-matter phenomena in an extremely controlled fashion, for example, the transition from the superfluid to the Mott insulator phase [19], the BEC-BCS crossover that probes different interaction regimes [20–22] and quantum atom optics [15, 23, 24]. While most of these experiments were limited to the observation of collective properties of the ensemble, more recent detection techniques allow for resolving single sites in optical lattices [25–27] or even the detection of individual atoms from an atomic cloud [28–30]. The detection of individual atoms can be easily realised in noble gases where due to the high internal energy of metastable states (several eV compared to about 10^{-10} eV of kinetic energy in a BEC) it is relatively easy to efficiently detect single particles. In particular, BECs of metastable helium (He*) [31–33] have extended the field of atomic physics experiments to the single-particle level [28, 34–36]. Single-atom detection opens the path to performing matter-wave analogues [37–39] of some of the pioneering photon-entanglement experiments [14, 40, 41]. These experiments are based on four-wave mixing (FWM) in an atomic ensemble and correspond to spontaneous parametric down-conversion (SPDC) for photons. SPDC serves as a source for numerous photon entanglement experiments in the field of quantum computation and quantum communication. FWM in the atomic case has been realised within BECs [24, 42, 43], and it was shown that together with single-atom detection it exhibits correlations that outperform the classical ones, as reported by Kheruntsyan et al. [44]. Building on these experiments, it should be possible to create and analyse the EPR states for atoms and thus realise a long-standing quest for matter-wave interferometry. By analogy to the photon case, we expect that such states will open up a whole plethora of groundbreaking experiments for atoms with additional new features resulting from the possibility to switch between Bose and Fermi statistics and, most notably, gravitational effects that arise due to the mass of the particles.

In this thesis, I present the required experimental steps for the realisation of a Bose-Einstein condensate of metastable helium-4 atoms. This condensate is a necessary step towards a realisation and detection of momentum entangled states based on a proposal by Kofler et al. [39] (see the schematics in Fig. 1.1) and which has been extended in a PhD thesis of Maximilian Ebner [45] to accommodate diffraction slits directly in the BEC cloud. It is expected that the FWM process leads to momentum entangled particles which would be a three-dimensional analogue of the Einstein, Podolsky and Rosen (EPR) gedankenexperiment [39]. The EPR state involves entanglement of massive particles in their external degrees of freedom. Not only will its realisation be a useful tool for a direct comparison with the photon entanglement experiments, but also it could potentially boost the sensitivity of matter-wave interferometers. From there on, specific features of matter such as the Fermi statistics and its strong sensitivity to gravity will extend the playground of entanglement beyond the possibilities of photonics.

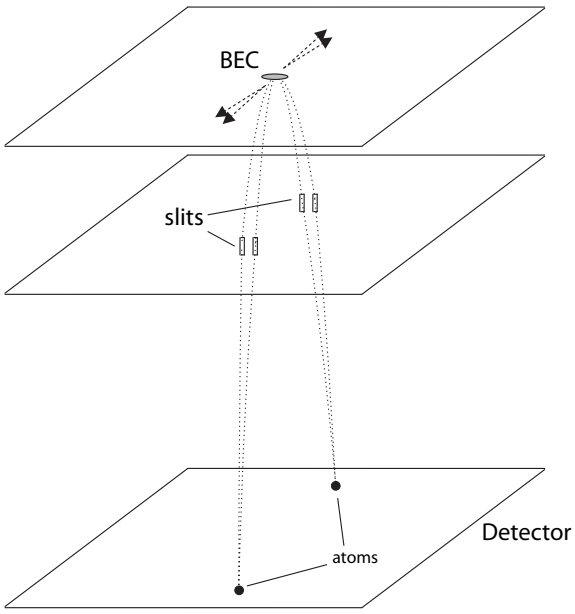

FIGURE 1.1. A general schematics of the detection of atomic correlations (adapted from Ref. [39]). A pair of entangled atoms is generated in the BEC via a four-wave mixing process, falls onto a single-particle detector through a pair of slits that erase their which-path information.

1.1. Outline of the thesis

Since helium in its ground state has no optically available transitions, laser cooling can only be performed in the metastable triplet state (2^3S_1). This state has a lifetime of more than two hours (7900 s [46, 47]) and a high internal energy (19.8 eV). The advantage of this energy is that helium has excellent single-particle detection capabilities. In a collision process such a high internal energy can be easily transferred to the partner, at the same time de-exciting metastable helium atom to the ground state. A detector that takes advantage of this feature is called a micro-channel plate (MCP) detector and it allows for a single-particle detection.

Typical helium BEC experiment consists of a source where the metastable atoms are created and collimated, a slowing stage and an experimental chamber where the atoms are trapped and cooled to the degeneracy. Yet the heart of each helium setup is the MCP detector that is positioned typically several cm below the trap. Our experimental setup combines optical detection and an MCP detector. The latter is crucial for single-atom detection and eventual quantum correlation measurements. To achieve this, it is designed for high count rate, good resolution and the possibility of true simultaneous detection with its four independent quadrants, a novel feature that will be especially useful for experiments in schemes with number squeezed states and a highly directional output.

The next chapter describes the experimental setup for the cooling and trapping of metastable helium. Firstly, metastable atoms are produced in a liquid-helium cooled dc-discharge source. After subsequent collimation and cooling of the atoms, the achievement

of a magneto-optical trap (MOT) containing typically 10^9 atoms is described. Apart from the full characterisation of the MOT cloud, a two-body loss rate coefficient in the presence of laser light is determined. There is an extensive description of a magnetic trap that is crucial for performing ultracold-atom experiments. The detection section presents proper fit functions for the thermal (and BEC) clouds from the absorption images as well as from a microchannel-plate detector.

Chapter 3 elucidates the required additional cooling steps. Firstly, loading of the atoms into a magnetic trap from the MOT is described. It is followed by a 1D cooling of a sample of 8×10^8 atoms to almost the Doppler temperature of 120 µK. An optimisation of evaporative cooling that allows us to reach quantum degeneracy concludes the chapter.

Reaching the Bose-Einstein condensate is described in Chapter 4, where a brief theoretical description is given. In addition, the means to prove the degeneracy are given while observing the evolution of the cloud in the time-of-flight measurement. We observe the transition to a BEC at a temperature around 1 µK and typically achieve a few 10^6 atoms in the degeneracy. Measurements of the decay of the condensate are given. Additionally, since the BEC is a coherent matter wave, its outcoupling has been performed by means of radio-frequency pulses. This free falling matter wave (sometimes referred to as an "atom laser") is then observed on the MCP detector.

CHAPTER 2

Experimental setup and related theory

This chapter describes extensively the experimental setup that is necessary to create the Bose-Einstein condensate of metastable helium-4. The metastable atoms are produced in a dc-discharge source after which they are slowed and captured in the science chamber in the magneto-optical trap. Typically a few 10^9 atoms are then cooled to a temperature of 1.5 mK. We will describe the powerful single-particle detection technique of the cloud utilising a micro-channel plate detector as well as the relevant fit functions. This chapter contains also details concerning the creation of the ultra-high vacuum, the laser system, magnetic trap and experimental control.

2.1. Helium

This section describes the most important properties of helium that were relevant for the experiments discussed in this thesis.

Helium is the second lightest element and the simplest multielectron atom. It is a noble gas which means that it is inert. It has two stable isotopes: bosonic ^{4}He and fermionic ^{3}He. Helium-4 is the isotope with the natural abundance of 99.99986% and the rest belongs to ^{3}He [48]. Helium-4 is produced primarily by distillation of natural gas deposits. Most of helium supply comes from the US (80%) and Algeria (16%). Due to its low melting point (−272.2 °C) it is commonly used in refrigeration technology, especially as a coolant in superconducting magnets. It is also used as a shielding gas in welding, as protective gas in controlled atmospheres and for lift in balloons. Even though helium-3 is abundant in earth crust, it is sourced from a decay of tritium.

An experimental setup that was built in this thesis was designed to use a ^{4}He isotope. Due to the fact that the spin of the nucleus vanishes, $I = 0$, there is no hyperfine splitting of the ground state in the energy level structure (see Fig. 2.1). This results in no need for a "repumper" laser, whose purpose is to maintain electrons in a cyclic transition. The spectroscopic properties of helium that are important for laser cooling and trapping are shown in Fig. 2.1.

Helium in its ground singlet state 1^1S_0 has no optically available transitions; thus, laser cooling can only be performed in the triplet state 2^3S_1. This state is a lowest lying excited state which is metastable (He*) with a lifetime of $\tau = 7900$s [46, 47]. The reason for such a long lifetime is that the de-excitation to the ground state is doubly forbidden, due to the fact that the parity does not change and that it is a $J = 1 \to J' = 0$ transition. In the metastable state helium atoms have 19.8 eV of internal energy. This energy is released upon a collision with any atom (or surface), at the same time deexciting metastable helium

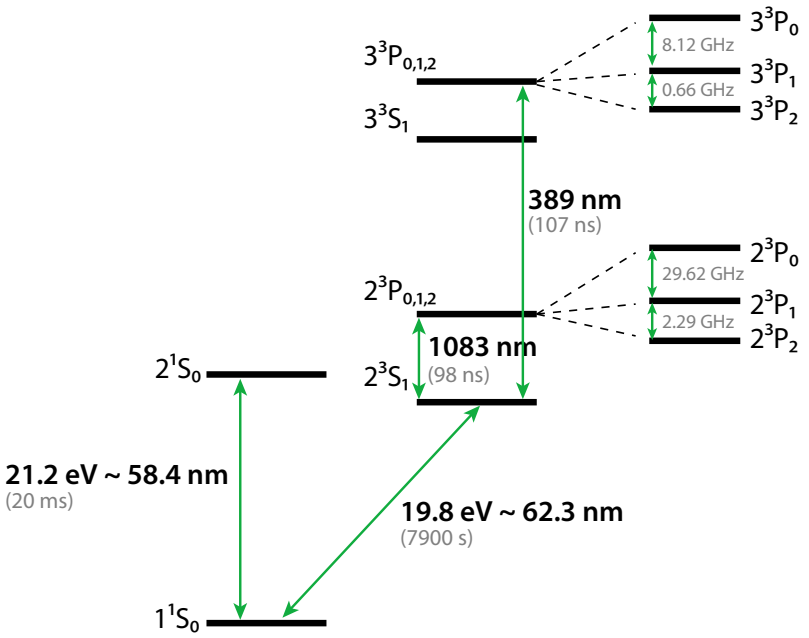

FIGURE 2.1. Selected energy levels of the ^{4}He atom. The spectroscopy data is taken from [49] and [50].

atom to the ground state. This can be seen as an advantage over other elements, because it can be used to detect single helium atoms using a different method than optical imaging.

However, high internal energy has its disadvantages. If a metastable helium atom collides inelastically with another particle, whose ionisation energy is less than the internal energy of He* (19.8eV), then the He* decays to the ground state and the other atom is ionised. This ionisation process was predicted in 1927 by Penning [51], and is often referred to as a Penning ionisation. It was demonstrated by Herschbach et al. [52] that in order to suppress Penning ionisation between two metastable atoms one has to spin polarise the atomic ensemble. Spin polarisation what in the case of He* corresponds to transferring the atoms to the $m_J = +1$ magnetic sublevel. As it turns out, suppression of Penning ionisation was one the vital steps towards achievement of a BEC in metastable helium.

Figure 2.1 shows the energy diagram of the lowest lying states in ^{4}He. The main transition used in the dissertation was $2^3S_1 - 2^3P_2$ with a vacuum wavelength of 1083.33 nm [53]. The natural linewidth of this transition is $^{1083}\Gamma = 2\pi \times 1.6248\,\text{MHz}$ and the saturation intensity $^{1083}I_s = \pi hc\,{}^{1083}\Gamma/(3\lambda^3) = 1.6703\,\text{W/m}^2$. The other important transition is between 2^3S_1 and 2^3P_2 states with a vacuum wavelength of 388.975 nm. This transition has a linewidth of $^{388}\Gamma = 2\pi \times 1.49\,\text{MHz}$ and the saturation intensity $^{389}I_s = 33.1\,\text{W/m}^2$. Scattering properties, which are very important for a thermalisation during an evaporative cooling process, between two spin-polarised helium atoms are very good. The scattering length was found to be $a_{11} = 7.512\,\text{nm} \approx 142a_0$ (where $a_0 = 53\,\text{pm}$ is the Bohr radius) [54]. The mass of ^{4}He is 4.002 603 254 153(64) amu or $6.646\,477\,7(5) \times 10^{-27}$ kg [55].

2.2. Atomic beam line

Helium in its ground state, unlike alkali-earth atoms like lithium [56], sodium [57], potassium [58], rubidium [16] or caesium [59], does not have any transition that would be feasible for laser cooling. Thus, Bose-Einstein condensation of helium has only been achieved with helium in its lowest lying excited, metastable triplet state, 2^3S_1 [31, 32, 60]. From this state there exist two cycling transitions to 2^3P_2 and 3^3P_2 states that facilitate laser cooling. To drive these transitions one needs lasers with 1083 nm and 389 nm wavelength, respectively. The crucial component of any metastable helium experiment is a source where helium atoms are transferred to the metastable 2^3S_1 state. The description of the source is the subject of the following section.

2.2.1. Source of metastable helium atoms

Due to selection rules there are no allowed electric dipole and quadrupole transitions between the 2^3S_1 triplet state and the singlet 1^1S_0 ground state [61]. This makes the highly energetic state (19.8 eV above the ground state) hard to excite but also very long lived, that is, metastable. The radiative lifetime of almost 7900 s [47, 62] allows us to consider this state as the effective ground state, with two laser-accessible closed transitions. These transitions allow for optical manipulation of He^* atoms.

We have built a supersonic, cold-cathode, dc-discharge source that yields high flux and continuous output, as described in [63]. As in the design of Kawanaka et al. [64], the metastable atoms are produced by electron impact in a reverse flow scheme, in which the gas flow at the discharge position is opposite to the output direction of the source, which helps to reduce the velocity of the emitted atoms (Fig. 2.2).

Cryostat and the vacuum chamber

The vacuum chamber, in which metastable atoms are prepared, is divided into two sections:

- a source chamber shown in Fig. 2.2: Its main purpose is to excite helium to the metastable state and preselect atoms with the relevant velocity components;
- a collimation chamber shown in Fig. 2.4: In this chamber high vacuum is maintained and the atomic beam is collimated. Additional metal plates are used to deflect ions and electrons away from the atomic beam. It also provides access to detectors for troubleshooting purposes as the flux can be measured and we can observe the fluorescence of the beam.

These two chambers are pumped by two turbo-molecular pumps described in Sec. 2.3. Additionally, a 4 K cold-finger cryostat (Vericold[1], VT4-500) has been installed in the source chamber. The cold finger of the cryostat is connected to the copper block, in which a tungsten needle is located, via braided copper wires. We are measuring the temperature of the cryostat in three places using calibrated temperature sensors (two PT100 sensors and one CerOx sensor). Two of them are placed on the first and second stages of the cryostat, whereas the CerOx one is positioned on the copper part holding the nozzle (see

[1]Now, part of Oxford Instruments.

Fig. 2.2 for clarity) as close to the discharge region as possible[2]. The cryostat reduces the atomic velocity to $600\,\mathrm{m\,s^{-1}}$ (see Fig. 2.3). Additionally, it reduces the pressure in the chamber by an order of magnitude.

The utilisation of glass components seen in Fig. 2.2 results from the fact that according to Paschen's law, the breakdown voltage in the case of helium reaches its minimum of $100\,\mathrm{V\,cm^{-1}}$ around 1 mbar [65]. As the pressure at the back of the source is around 1 mbar and the operating voltage is 2 kV, the presence of any conducting surfaces would initiate unwanted discharge.

To ensure an undisturbed operation we are using commercially available ultra-pure helium (Air Liquide AlphaGaz with 99.9999% purity).[3]

Needle

The dc discharge takes place between a tungsten needle and a stainless steel plate. It is important to choose the proper tungsten alloy, as it is needed for high output, uninterrupted source operation and lower maintenance of the source.

Due to the fact that tungsten rods are extensively used in the welding industry, their alloys are widely available. We tested pure tungsten rods, a few lanthanated tungsten alloys WL10, WL15 and WL20 (with 1%, 1.5% and 2% of lanthanum oxide, respectively) as well as an E3® alloy that, like WL15, contains 1.5% of lanthanum oxide, but additionally a 0.08% admixture of zirconium dioxide and 0.08% of yttrium oxide. Compared with pure tungsten, the addition of admixtures increases the maximum current-carrying capacity by approximately 50% for a given electrode size. All admixtured needles promise to deliver a more stable arc than pure tungsten ones, though we observed that this is not always the case. For example, while the E3® is easier to ignite than the other alloys and the current capacity is higher than any other tested alloy, it was very hard to maintain discharge in a proper "regime"[4], which renders it unsuitable for our application. Higher current capacity allows for lowering the discharge voltage, which in turn reduces the load on the cold finger. The differences between tested WL alloys were minor. Due to the discharge instability we discarded E3® from our selection and we decided to pick WL20 to use in our source, as its discharge proved to have the highest current at the same voltage applied to the needle.

As it turns out, proper sharpening of the tip of the needle is also relevant. Since we want to achieve high electrical field density at the end of the needle the tip has to be pointed. This also allows the discharge arc to be more focused. The method of grinding of the tip is important as well. The grinding of the tungsten rod has to be done along the rod (and not radially) to ensure that the grind marks run along the length of the electrode. Doing so reduces the presence of ridges on the tungsten that could make the

[2] All source temperatures mentioned in this thesis refer to the temperature measured with this sensor.

[3] Even though we are using high purity helium, some nitrogen gets into the system and sticks onto the cold finger of the cryostat. Thus to remove it and ensure undisturbed operation the source has to be heated to 60 K every night. The cold finger (2nd stage of the cryostat) is connected to the copper part via a copper braid.

[4] This term can only be characterised qualitatively. The characteristic of this discharge is a bright, blue-white glow that can be seen in front of the nozzle. As a result, we observe a high flux of metastable helium.

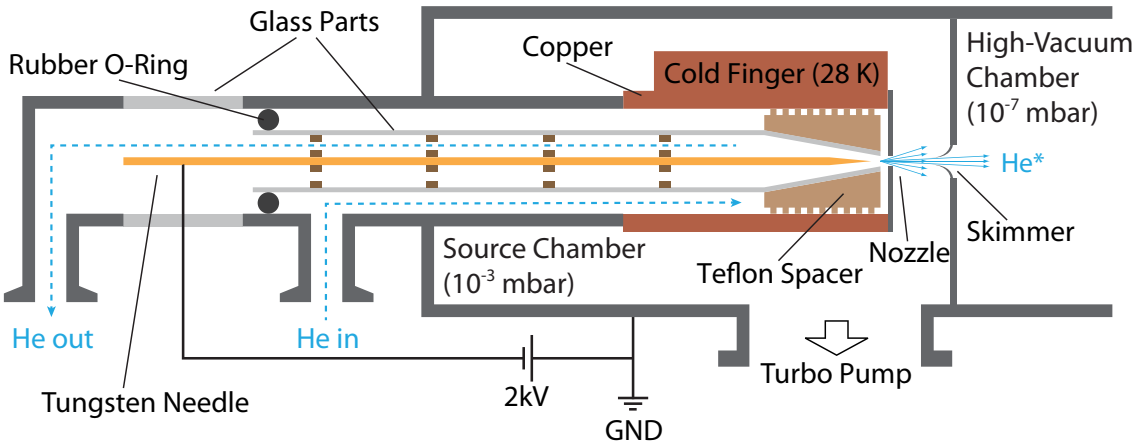

FIGURE 2.2. A schematic diagram of the metastable helium source. Helium enters the vacuum system and flows to the front of the vacuum tube where a helically-grooved teflon spacer ensures good contact with a copper tube cooled by a cryostat. A part of the atoms is excited in an electric discharge between the tungsten needle and nozzle. While a fraction of the atoms enters the high-vacuum chamber after supersonic expansion through the nozzle and spatial filtering by a skimmer, the rest gets pumped out at the back of the source. Ceramic spacers align the tungsten needle in the glass tube; glass vacuum parts prevent parasitic discharge (c.f. Sec. 2.3 for more details). The end of the needle is mounted on a linear translation stage (not drawn) to be able to change the position of the needle with respect to the nozzle. Two rubber o-rings seal the direct path from the inlet to the outlet. The copper part that holds the nozzle is connected to the 2nd stage of the cryostat via a braid made out of copper to be able to position the nozzle with respect to the skimmer.

arc wandering. To avoid contamination of the material, grinding has to be done with a grinding wheel specially designated for tungsten.

The needle is glued onto Teflon spacers that centre it inside of the vacuum tube, and its end is mounted on a linear translation stage that controls the position of the needle with respect to the nozzle. The needle position is responsible for the ignition and the stability of the discharge [63]. The needle is connected in series with a 500 kΩ resistor that stabilises the discharge and a power supply (Iseg HPn 60-506) delivers the high voltage to the needle.

Operation

Helium enters the vacuum system through a needle valve (3 mbar inlet pressure). The gas flows between a glass tube and a steel tube to the cold finger. The cold finger is held at a temperature of approximately 16 K to reduce the kinetic energy of the helium by contact cooling. The cold atoms then pass a strong electric field between a tungsten needle kept at −2 kV and a grounded nozzle, where they are ionised by field ionisation and a plasma is created. While some of the gas expands supersonically through a 0.5 mm wide nozzle[5], the rest of the gas flows back through the glass tube and is pumped out of the system. Through collisions of the helium ions with energetic free electrons, neutral helium atoms in electronically excited states are created. Through various electronic cascades, only a fraction ($10^{-5} - 10^{-4}$ [66, 67]) of the atoms ends up in the energetically lowest triplet state of helium 2^3S_1. In the $\sim$ 1.5 cm expansion region between the nozzle and the skimmer the collision rate drops significantly and the atoms that got excited to the metastable state stay there. A conically shaped skimmer with a 0.5 mm wide opening selects a small fraction of a solid angle of the atomic beam. Thus, together with photons, ions and helium atoms in other internal states, a fraction of these metastables gets transmitted to the high vacuum chamber (10^{-7} mbar when operating).

The main design parameters of a He* source for cold atom experiments are atomic flux and velocity. While the former should be as high as possible, the latter should be as low as possible. The low velocity ensures a short distance for the subsequent deceleration and thereby increases the capture efficiency of the magneto-optical trap (MOT). Since in a discharge source a higher flux is mainly achieved by intensifying the plasma (either by increasing the helium inflow or the discharge voltage), this also causes more heating and thereby higher velocities of the atoms. Some of the He* sources reported in the literature are run at room temperature [68] while others are cooled with liquid nitrogen [69] or even liquid helium [70, 71]. Our design for the first time uses a closed-cycle two-stage pulse-tube cooler that cools our source to temperatures significantly below liquid nitrogen temperatures (< 20 K during operation) while still being able to deliver a significant cooling power of about 2 W at those temperatures. With this, we can tune the discharge parameters to generate an atomic beam with a flux in the range of $(1 \times 10^{14}$–$8 \times 10^{14})$ atoms sr^{-1} s^{-1} and velocities between 450 m/s and 1000 m/s. The beam intensities were measured with a Faraday cup detector (FC1 in Fig. 2.8) in which electrons are ejected upon collision with a stainless steel plate by the high internal energy of the He* atoms. In order to determine

[5]The diameter of the nozzle is crucial to get a discharge in a proper "regime" [63].

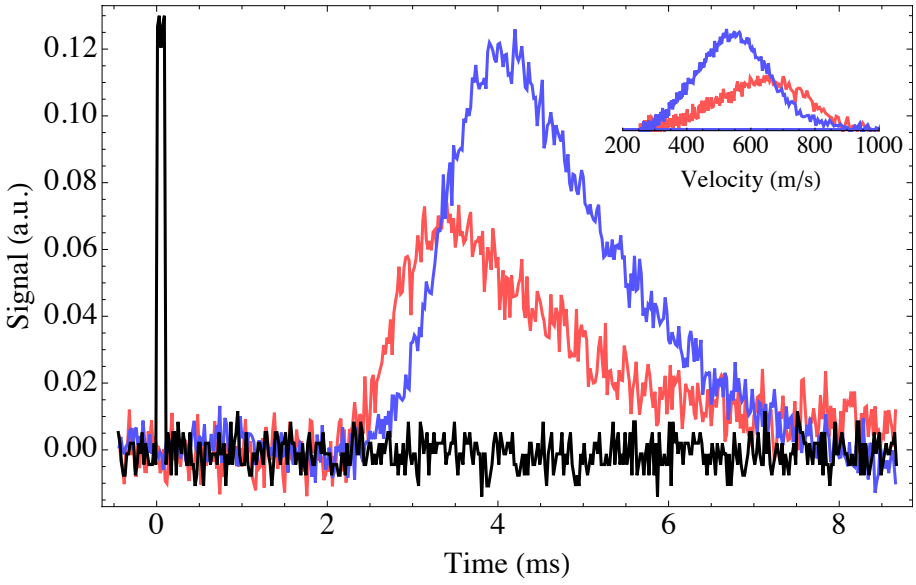

FIGURE 2.3. Measurement using time-of-flight technique of the velocity distribution of He* source at a discharge current of 2 mA. Data was taken before cool-down of the source at 60 K (red curve) and after cool-down at 22 K (blue curve). Time is measured with respect to the light pulse (black curve). The temperatures are readings from the sensor closest to the discharge region. Inset shows the same data represented in a velocity space.

the velocities, we used the second Faraday cup detector (FC2 in Fig. 2.8) located at the very end of the atomic-beam line. To determine the velocity distribution a time-of-flight technique was used (see Fig. 2.3, for sample curves). There are three main contributions that affect the mean velocity of the atomic beam:

- The temperature on the cold finger of the cryostat and the available cooling power. While the latter is fixed the former depends on the heat load, i.e. the temperature of the plasma and the power applied to the heat resistor;
- The temperature of the plasma. It is hard to deterministically control it, as we do not have any possibility to directly measure it. The temperature depends on both the applied voltage to the needle and the amount of helium at the inlet;
- The supersonic expansion after the skimmer, that can be controlled by changing the pressure in the source chamber. However, for a given pumping speed the pressure in the chamber is practically fixed;

Since the last contribution is fixed and the first two contributions are coupled, the main adjustments to the atomic velocity are done by changing voltage and helium inlet pressure.

We usually operate our source at 4×10^{14} atoms $\mathrm{sr}^{-1}\,\mathrm{s}^{-1}$ and a peak velocity of 600 m/s by applying a discharge voltage of −2 kV and adjusting the helium inlet pressure to around 3 mbar. These values allow us to load a magneto-optical trap (see Sec. 2.6) with sufficient number of atoms for further cooling.

2.2.2. Collimation

In order to intensify and collimate the atomic beam, we use two-dimensional laser cooling. A laser beam is reflected between the surfaces of two mutually perpendicular mirror pairs, that are slightly inclined with respect to the atomic beam axis (shown in Fig. 2.4). In this way, effectively a curved wavefront of the laser light is created. This curvature prevents atoms from falling out of resonance, due to the Doppler shift, after change of the direction of the velocity, as would have been the case with plane waves. This would increase the capture angle of the collimation [72] $\beta = L/R$, with the collimation length L and the radius of curvature R of the beam path.

Effectively only the atoms that are perpendicular to the laser beam follow its curvature, thus following a circular trajectory. Assuming that the centrifugal force does not exceed the radiation pressure force, we can estimate a limit on how small R can be. For high laser intensity ($I \gg I_s$, where $I_s = 0.17\,\mathrm{mW/cm^2}$ is the saturation intensity of the atomic transition) we can estimate the minimal radius of the wavefront

$$R_{min} \geq \frac{m\lambda v^2}{\pi\hbar\Gamma}, \tag{2.1}$$

where $\hbar$ is Planck's constant divided by 2π, m is helium-4 mass, λ is the wavelength of the light and $\Gamma/(2\pi) = 1.62\,\mathrm{MHz}$ is the natural line width of the $2^3\mathrm{S}_1 - 2^3\mathrm{P}_2$ transition.

We use two orthogonal laser beams that are linearly polarised and are resonant with the $2^3\mathrm{S}_1 - 2^3\mathrm{P}_2$ transition of He*. They enter the vacuum chamber at a capture angle of about 20 mrad as close to the skimmer as possible to capture as many atoms as possible. Then the beams are reflected between the mirror pairs over length $L = 16\,\mathrm{cm}$ at which end they are blocked. This geometry corresponds to a radius of curvature $R \approx 7\,\mathrm{m}$. The diameter of the laser beams is 6 mm, their intensity is $500\,I_s$.

The atomic beam passes between two metal plates kept at a potential difference of 1 kV to deflect ions and electrons from the beam. While this was implemented as a precaution to minimise collisions of metastable atoms with charged particles in the beam, the influence on the loading rate of the trap turned out to be negligible. Nonetheless, to optimise and measure the flux of the atomic beam, it is necessary to deflect charged particles from the beam as their contribution to the measurement signal can be up to an order of magnitude higher than the one from the metastable atoms.

The beam can be detected either using the fluorescence of the atoms at 389 nm ($2^3\mathrm{S}_1 \rightarrow 3^3\mathrm{P}_2$ transition) or Faraday cup detectors. The fluorescence imaging can be performed in a cube just before the Zeeman slower (marked with FI in Fig. 2.8) using a resonant light sheet at an angle of 45°. The Faraday cup detectors are installed in both collimation and the experimental chambers and can be precisely positioned in the beam path using a linear translation stage. Their locations are marked with FC in Fig. 2.8. Using collimation, we observe a 30-fold increase in the atomic flux on FC1, that is comparable to the other helium experiments [68, 69, 72, 73]. We thereby reach a flow of metastable atoms at *FC2* exceeding 1.5×10^{11} atoms/s.

The atomic beam traverses straight to the Zeeman slower (described in Sec. 2.2.3) through a 6 mm opening in a mechanical shutter (Vincent Associates, Uniblitz LS6TF)

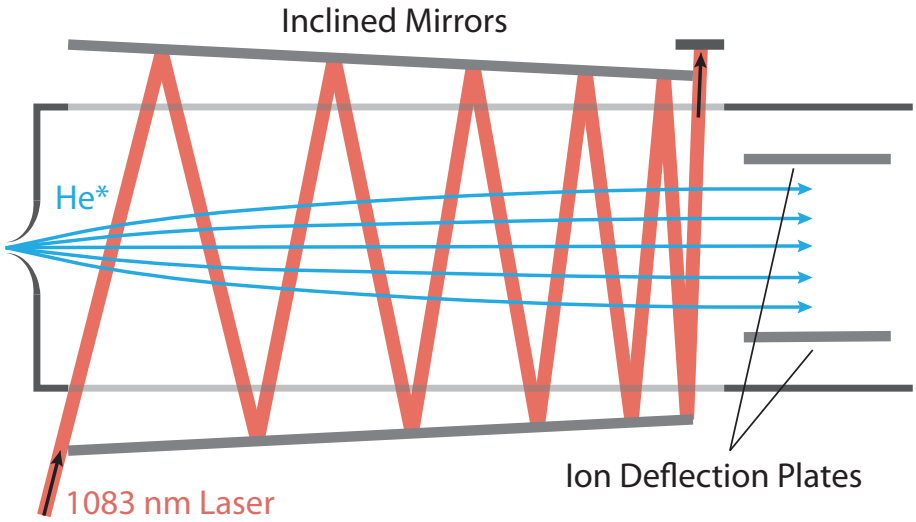

FIGURE 2.4. Scheme of the laser beam alignment between one pair of the collimation mirrors. A 6 mm wide laser beam is reflected twelve times between two mirrors that are inclined at a small angle to increase the capture velocity. By this method the He* atoms are transversally cooled and a collimated beam of metastable helium atoms is obtained. Dimensions are not to scale, the angles are greatly exaggerated.

that can block the beam on a µs timescale. However, this barely improves the vacuum in the experimental chamber (see Sec. 2.3). Instead of deflecting the beam, we decided to block the unwanted atoms by a gate valve (VAT Mini UHV Gate Valve), that was placed at the Zeeman slower flange. This valve operates on a timescale of a second which is fast enough compared to the lifetime of the magnetic trap. We are thereby not losing metastable atoms, the alignment of the laser beams and of the vacuum chamber with respect to the rest of the setup is straightforward, and we are operating the magnetic trap, basically, at the base pressure. The beam-line shutter is mounted on the same vacuum feedthrough as the FC1 right behind the ion deflection plates. In order to be able to maintain an ultra-high vacuum in the trapping chamber (see Sec. 2.3) we had to insert a differential pumping tube at the front of the slower. This helps to maintain three orders of magnitude pressure difference between these two chambers (c.f. Table 2.1) while the gate valve is open.

2.2.3. Zeeman slower

Even though the helium atoms are precooled in the source, the longitudinal velocity of the atomic beam exceeds by far the capture range of our magneto-optical trap. Thus, the common technique of Zeeman slowing [74, 75] is used to decelerate the atoms from $v \approx 800\,\mathrm{m/s}$ to less than $100\,\mathrm{m/s}$.

The atoms are slowed by a resonant, counter-propagating laser. In order to compensate for the change in Doppler shift during deceleration, a spatially varying magnetic field is

created with a tapered solenoid, which causes a position-dependent shift of the Zeeman sublevels [74]. The optimal field should have the profile of [76]

$$B(x) = B_0 + B_t\sqrt{1 - \frac{x}{x_0}}, \tag{2.2}$$

where x_0 is the length of the slower and

$$B_0 = \frac{\hbar}{\mu_B}(\Delta + \delta), \tag{2.3}$$
$$B_t = \frac{\hbar}{\mu_B}kv_0,$$

are the bias and taper fields, respectively, with the Bohr magneton μ_B, $\hbar$ Planck's constant divided by 2π, laser detuning Δ (without taking the Doppler or Zeeman shift into account), target detuning δ, wave vector $k = 2\pi/\lambda$ and initial velocity v_0. The simplest design would be to have $\Delta = 0$. At this detuning one would need to have an increasing (or decreasing) magnetic field profile. An increasing magnetic field profile is not desirable as the field at the very end of the slower would be very high and would disturb the operation of the magnetic trap by influencing the stability[6] and the position of the magnetic trap. Secondly, there is a level crossing at 563 G between $2^3\mathrm{P}_2$, $m = 2$, and $2^3\mathrm{P}_1$, $m = 0$, sublevels that would cause losses due to the decay to the metastable singlet state $2^1\mathrm{S}_1$ [77]. Moreover, since the slowing beam passes centrally through the trapping region, it would have been resonant with the atoms and the MOT cloud would have been deformed. For the last two reasons the reversed configuration of the magnetic field (i.e. a decreasing field) would also not work. Hence, with these design constraints we decided model a slower that would work at $\Delta/(2\pi) = -370$ MHz. This implied that the magnetic field had to have a zero crossing, thus care had to be taken that the magnetic field gradient would be small enough not to lose atoms due to Majorana-spin flips (see Sec. 2.7 for further details).

To optimise the field, we model the coil system with individual windings distributed such that the desired field is matched. The exact optimisation algorithm can be found in Florian Leupold's Diploma thesis [78]. One would like to construct a slower whose end is as close to the MOT as possible, though, the number of layers of windings is limited on one side by the distance between two viewports in the science chamber (see Fig. 2.8 and Fig. 2.31), and on the other hand by an outer diameter of the vacuum tube, which in our case is 34 mm. In principle, one could make the tube smaller, but then the field in the centre would be less uniform. Our design decelerates atoms that are located up to 10 mm off axis, which is especially important compared to the initial beam size of 3 mm. In total, the Zeeman slower consists of 1.7 km enamelled rectangular wire (2.5 mm × 1.1 mm) wound onto a 1.36 m long vacuum tube. The advantage of the rectangular wire is that it allows for much better winding and the loop density is higher than with the circular wire. While our slower is 30% shorter than the experiments working with a liquid nitrogen [79], it could have been even shorter as shown by Dedman et al. [75]. However, as the slower is longer than necessary it also has a higher velocity acceptance. Seventeen double layers of windings in two sections with opposite magnetic field direction achieve a sufficiently strong

[6]Current stability in the Zeeman slower is not crucial, thus usually the current supplies are not stabilised.

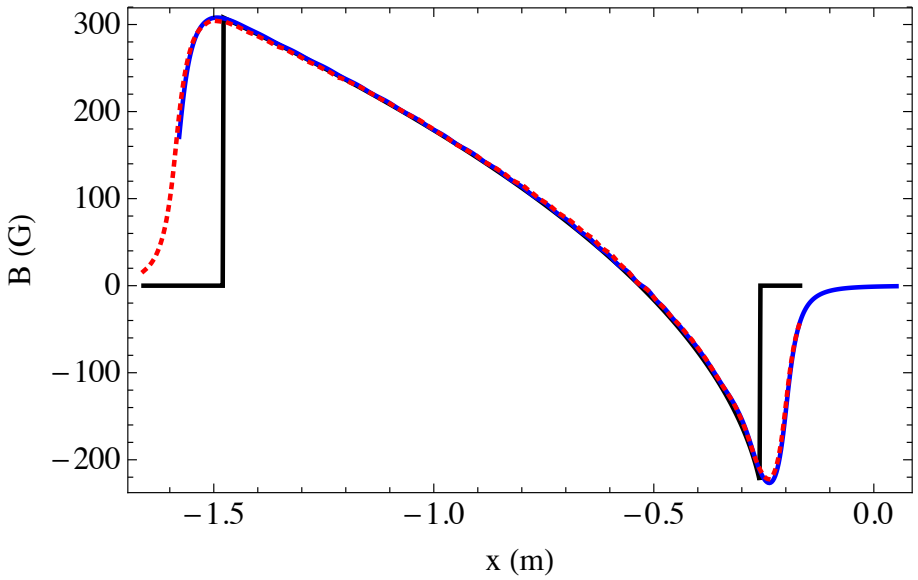

FIGURE 2.5. Magnetic field (black, solid line) for the ideal Zeeman slower, simulated field (blue, solid line) and experimentally measured field (red, dashed line). The origin of the x-axis is located at the centre of the atom trap in the science chamber.

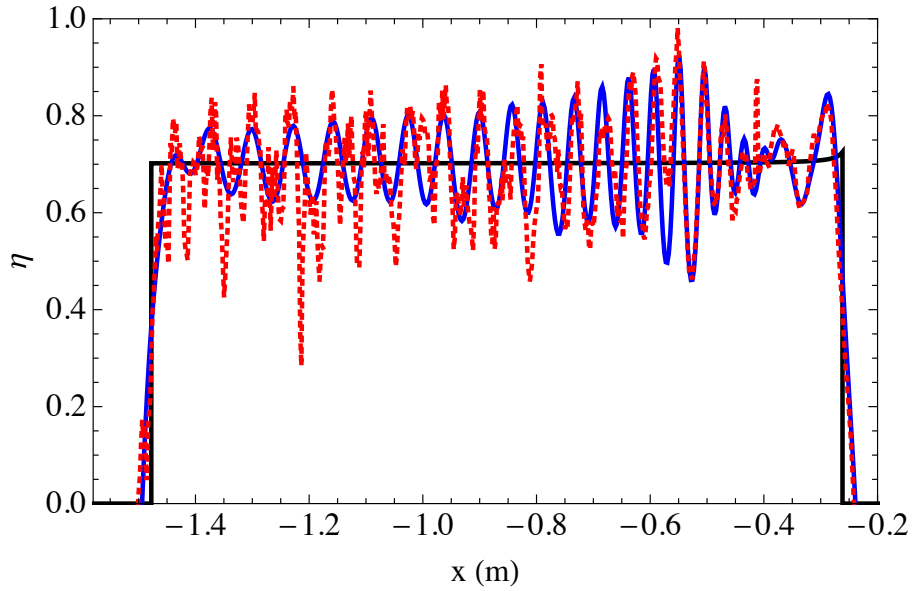

FIGURE 2.6. The ideal (black, solid line), simulated and measured effective deceleration η of the slowing process. The measured efficiency (red, dashed line) oscillates around the theoretically expected efficiency (blue, solid line) due to the discrete steps of individual layers of the solenoid.

magnetic field at a current of 2 A without the need for active water cooling. The magnetic field profile has been measured with a Hall probe (Lakeshore HMNA-1904-VR) that was guided through the tube and found to be consistent with the model. The measurement along the axis of the slower together with the target field is depicted in Fig. 2.5.

While the field of an ideal Zeeman slower has a smooth coil variation along the axis which results in a constant deceleration, a real solenoid is made out of individual windings with steps at the end of each layer. At these steps, the magnetic field changes faster than what would be required for constant deceleration. To take this into account, a position-dependent effective deceleration $\eta(x)$ of the Zeeman slowing can be calculated [75],

$$\eta(x) = \frac{2m\mu_{\text{eff}}}{\hbar^2 k_L^3 \Gamma} \frac{dB(x)}{dx} \left(\frac{\mu_{\text{eff}} B(x)}{\hbar} - \delta_0 \right). \tag{2.4}$$

As can be seen in Fig. 2.6, the effective deceleration of the slower oscillates according to the layer structure. However, the measured data deviate from the simulated ones as the steps of individual windings in the solenoid are not a perfect step function. The atoms are decelerated as long as they remain resonant. Once the resonance condition is lost, the atoms will not get back into resonance and are not slowed any further. It is, therefore, practical to make the slower a little longer than theoretically necessary. A length of the solenoid of 1.36 m gives an average efficiency of 0.7 and guarantees $\eta \leq 1$ everywhere along the trajectory of the atoms through the tube.

The solenoid for the Zeeman slower is split into two sections that are driven by a standard laboratory power supply (Thurlby Thandar Instruments PL330QMD). These coils create a magnetic field in two opposite directions. Figure 2.7 shows the influence of the two slowing sections on the velocity distribution of the atomic beam. The velocity of the atomic beam after the Zeeman slower was measured with a resonant laser beam that was tilted to be sensitive to the velocity component along the Zeeman-slower axis. By scanning the laser frequency we probed the velocity distribution of the atomic beam. When the first solenoid is switched on, the axial velocity of the atoms is reduced in this measurement from 900 m/s to 400 m/s, and the second section reduces the axial velocity further to speeds that can be captured by the MOT, typically about 80 m/s. Due to the residual magnetic field that is present in the magnetic trap centre, the second section of the Zeeman slower is switched off after the loading of the MOT. It is done using insulated-gate bipolar transistor (IGBT) with the same control circuit as the offset coils (see Sec. 2.7.3), which additionally stabilises the current.

Atoms that are initially in $m = -1$ and $m = 0$ sublevels get pumped to $m = +1$ just after scattering of a few photons. As the atoms scatter more and more photons the atomic beam becomes wider, which is known as transversal heating of the beam. This is not so pronounced when the atoms are fast, but it is considerable at the end of the slower. Thus, the end of the slower should be located as close to the trap as possible. In our case due to the physical constraints the distance between the end of the coils and the MOT is 20.5 cm.

In order to slow the atoms, we use similar parameters for the laser as used by other groups with He^* BECs. Namely, the frequency of a laser beam at 1083 nm is red-detuned by −370 MHz with respect to the unshifted atomic transition (c.f. Sec. 2.4). The beam is

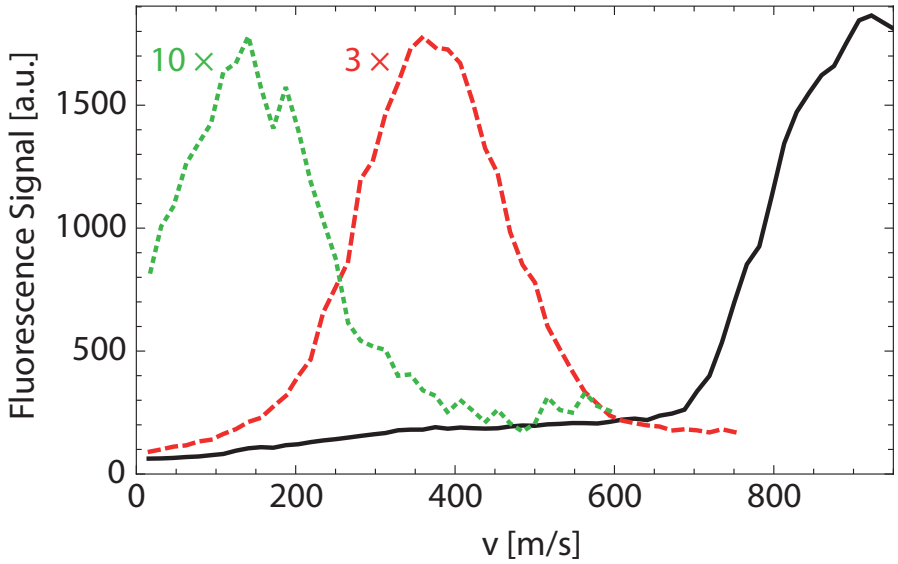

FIGURE 2.7. Example of the atomic beam deceleration when: no magnetic field is present (black solid curve); current is flowing only in the first section of the Zeeman slower (red dashed curve); current is flowing in both sections of the slower (green dotted curve). The velocity of the atomic beam after the Zeeman slower was measured with a resonant laser beam that was tilted to be sensitive to the velocity component along the Zeeman-slower axis. By scanning the laser frequency we probed the velocity distribution of the atomic beam. Without Zeeman slowing, the atoms have a peak velocity of about 900 m/s in this measurement, the first Zeeman slower section slows the atoms down to less than 400 m/s and the second section brings the velocity down to captureable values. For the purpose of the measurement the field of the second section was reduced by half such that the atoms exiting the Zeeman slower were not too dilute. Due to transversal heating within the Zeeman slower, the atomic beam expands, which leads to a decrease in fluorescence signal. For better comparison of the velocity distributions the results of the slowed atoms are therefore enlarged by a factor of 3 (red dashed curve) and a factor of 10 (green dotted curve), respectively.

circularly polarised[7] and would induce $\Delta m = +1$ and $\Delta m = -1$ transitions in the first and second stage, respectively. The beam has an initial diameter[8] of 36 mm and is focused behind the skimmer of the source. This way the component perpendicular to the atomic beam axis counteracts, at least to some extent, the transversal heating.

2.3. Vacuum chamber

In the experiment we are using Pfeiffer Vacuum turbo molecular pumps and a titanium sublimation pump (TSP) from Vacom. Additionally, in the source chamber a 4 K cold-finger cryostat has been installed, though its main purpose is not to improve the vacuum. The cryostat lowers the pressure both in the source as well as collimation chambers. An overview of pressures in the vacuum chamber with the helium load is given in Table 2.1. Both turbo molecular pumps in the source and collimation chambers are backed by multi stage roots dry vacuum pump (adixen[9] ACP 15) with a maximum pumping speed of 14 m^3/h. Whereas all other turbo pumps are backed by a small turbo pump. In the collimation region we are able to achieve high vacuum, whereas at the other end of the Zeeman slower we have an ultra-high vacuum (UHV). These two vacuum regimes are connected by a relatively large opening (34 mm) of the Zeeman slower tube. To prevent the deterioration of pressure in the trapping chamber conduction between them has to be minimised. We have achieved this by putting a 15 cm long stainless steel tube with a 3.5 mm bore at the entrance of the Zeeman slower, that serves as a differential pumping tube. Its outer diameter has been matched with the inner diameter of the Zeeman slower vacuum tube.

In the experiment we are using a stainless-steel vacuum chamber with the exception of the area at the back of the needle where all the vacuum parts are made out of glass (as seen in Fig. 2.2) to prevent discharge in undesirable positions. According to Paschen's law, the breakdown voltage, in case of helium, reaches its minimum of 200 V around 4 mbar cm [65]. As the pressure at the back of the source is around 1 mbar and the operating voltage is 2 kV the unwanted discharge can be very easily initiated if conducting surfaces are present.

The trapping chamber (Trinos Vakuum[10], detailed in Fig. 2.31) is made out of 316LN stainless steel, chosen for its low magnetic permeability (< 1.005) and ability to retain hardness at higher temperatures, especially after repeated bakeouts. Low magnetic permeability is important in avoiding the eddy currents in the chamber during repeated switching of the high currents in the experimental sequence. The main chamber can be divided into two separate chambers with a gate valve (VAT XHV all-metal gate valve):

- the experimental chamber where the atoms are captured and cooled to the BEC;
- the detector chamber where the delay line detector is located.

An additional gate valve that is located between the collimation chamber and the Zeeman slower allows for isolation of individual sections of the experiment without the need to

[7] In this manuscript we will use a convention labelling radiation that induces σ^+ (σ^-) transition, $\Delta m = +1$ ($\Delta m = -1$), as σ^+ (σ^-) circularly-polarised light.

[8] Unless indicated otherwise, the beam diameter in this thesis is given as $1/e$.

[9] Now belongs to Pfeiffer Vacuum.

[10] Now owned by Pfeiffer Vacuum.

TABLE 2.1. Pressure along the beam line with the helium load present (unless otherwise noted) and characteristics of the turbomolecular pumps (Pfeiffer Vacuum) used in the experiment, labelled as in Fig. 2.8. An adixen ACP 15 (V5SATSBFEF) is the backing pump for P1 and P2, while P3 — P7 are backed by P8.

vacuum section (pump label)	pressure (mbar)	pump type	pumping speed*(for N_2) in l/s
source chamber (P1)	$< 10 \times 10^{-4}$	HiPace 400, cold finger	355
collimation chamber (P2)	2×10^{-8}	HiPace 400	355
Zeeman slower (P3,P4)	N.A.	HiPace 300	260
experimental chamber (P5, P6)	5×10^{-11}†	HiPace 700, TSP	685, 3.5‡
detector chamber (P7)	6×10^{-11}§	HiPace 300	260
backing of P3-P7 (P8)	3×10^{-4}	HiPace 10	10

* from the data sheet

† without helium load

‡ the pumping speed of the titanium sublimation pump (TSP) depends on the area covered with titanium, thus the pumping speed is given in litres per cm^2

§ only if the gate valve is open, otherwise it is in low 10^{-10} mbar (see details in text)

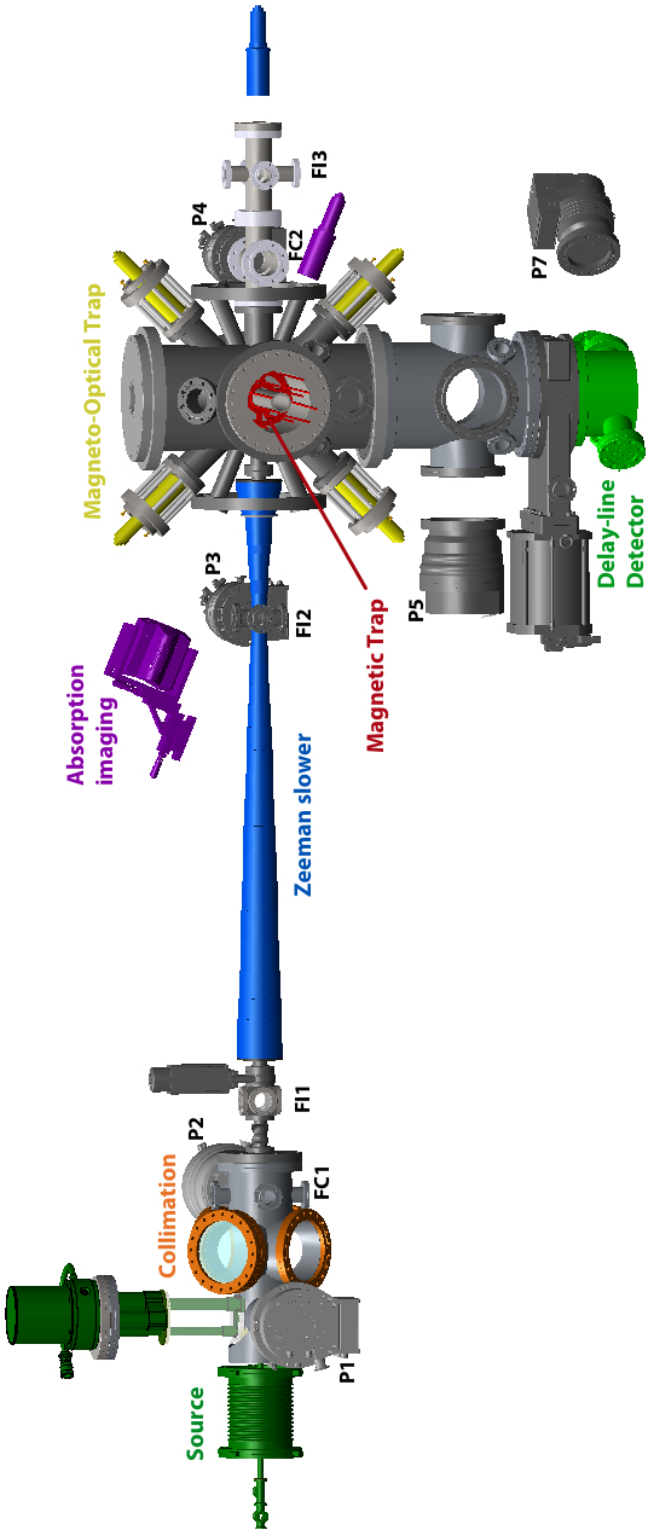

FIGURE 2.8. Overview of the vacuum system (starting from the left): The atoms are initially excited in the source (helium inlet tube and closed-cycle cryostat marked in dark green). The atoms get collimated by laser beams that enter through the windows drawn in orange and are decelerated in the Zeeman slower (highlighted in blue, as well as the telescope for the slowing laser beam). Four of the telescopes for the magneto-optical trap lasers are displayed in yellow (the two along the y-direction are not shown). Bose-Einstein condensation is achieved within the magnetic trap (coils shown in red) after forced evaporative cooling by radio frequency. The atoms can be imaged by absorption imaging (EMCCD camera and telescope in purple) or impact onto the single-particle resolving delay-line detector (located in the vacuum vessel in light green). The figure is drawn to scale but some components are not displayed. FC marks the positions where the two installed Faraday cup detectors can be inserted into the atomic beam path; the possible access points for fluorescence imaging of the atomic beam are marked with FI.

pressurise the UHV, whose bakeout and pump down to 5×10^{-11} mbar can take around two weeks.

The experimental chamber has three turbo-molecular pumps connected (two Pfeiffer Vacuum HiPace 300 and a Pfeiffer Vacuum HiPace 700), that are positioned as in Fig. 2.8. These pumps, after a two-weeks long bakeout, enabled reaching a pressure of 5×10^{-10} mbar. During bakeout the experimental chamber has been heated up to 200 °C, whereas the detector chamber to 150 °C and the Zeeman slower to 100 °C[11]. Further lowering of the pressure has been achieved by using a titanium sublimation pump (Vacom Vacuum TSP). The TSP filaments are positioned directly under the re-entrant flange (as in Fig. 2.31) such that the largest area of the chamber gets sputtered with titanium and there is no vacuum viewport in a direct geometrical line of sight of the filaments[12]. Furthermore, of the utmost importance is keeping the micro-channel plate and the delay-line detector away from titanium. This is achieved by closing the gate valve during the utilisation of the TSP. With a source turned off, this is enough to bring the pressure down to 5×10^{-11} mbar. This low pressure in the region of the trap is a crucial prerequisite to minimise the probability of collisions between trapped atoms and molecules from the background gas. These measures allow for a long storage time of the trapped atoms.

The detector chamber is evacuated using a turbomolecular pump (Pfeiffer Vacuum HiPace 300). It prevents pressure degradation while closing the gate valve due to the degassing of the micro-channel plate. Moreover, this pump enables independent bake out of the detector chamber.

2.3.1. Pressure

Vacuum quality varies across the setup, from high (HV) in the source chamber to ultra-high (UHV) in the trapping chamber. Pressure measurement in the beam and experimental chambers is measured with a nude Bayard Alpert ion gauges (SRS NR-F-UHV). During bakeout the filaments of the ion gauge have been degassed every 12 hours, to avoid contamination of vacuum at a later stage. During operation of the delay-line detector (see Sec. 2.5.2) the ion gauge is switched off, due to production of a considerable amount of ions. For this reason, we mounted a cold-cathode ionisation gauge (Pfeiffer Vacuum IKR 270) in the detector chamber that does not interfere with the DLD detection process. In this chamber we installed a spare Bayard Alpert ion gauge as well. We estimate the partial pressure of the helium beam to be 3×10^{-10} mbar while loading the MOT, and after loading to the MT we close the valve at the entrance of the Zeeman slower, thus we are operating at the base pressure of the chamber.

Furthermore, in the experimental chamber a residual gas analyser (Stanford Research Systems RGA100) allows for helium gas leak testing as well as monitoring the partial pressure before and after the bakeout.

[11] The temperature was measured on the outer layer of the slower, as we heated it by running current through the coils. Even though we used aluminium foil for insulation, the temperature of the inner layers was probably higher by several degrees.

[12] TSP filaments consist of titanium alloy and are heated electrically until titanium sublimates from the surface into the vacuum where it resublimes to the nearby area and forms a thin layer.

2.4. Lasers

The main laser system needed for all stages of the experiment is a commercially available fibre laser (Koheras[13]) producing a near infrared light at 1083 nm. A second laser with a wavelength of 389 nm is a frequency doubled diode laser (Toptica). It was meant to be used as an imaging laser, but the resulting absorption images had a low contrast. This we attribute to a high momentum kick during absorption (emission) of 389 nm photons (see Fig. 2.13). Thus, the blue light has been replaced by the infrared light and it is used mainly for troubleshooting purposes.

The output of the fibre laser is split evenly between spectroscopy, which stabilises its frequency on the $2^3S_1 \rightarrow 2^3P_2$ transition, and the input of the fibre amplifier (Keopsys) where it acts as a seed. The amplifier as well as the laser are based on a Yb^{3+} doped single-mode optical fibre where the population inversion is achieved by pumping them with the diode laser. Amplified in several stages the amplifier produces up to 5 W of output power which is more than enough to generate the beams required for various stages of the experiment. The combination of a fibre laser with a fibre amplifier is very convenient as it produces a single mode (TEM_{00}), high power, linearly polarised laser beam at a line width of 70 kHz. This line width was confirmed by a heterodyne beat measurement detailed in [78].

2.4.1. Frequency stabilisation

The frequencies of the lasers are stabilised by a Doppler-free spectroscopy. For the $2^3S_1 \rightarrow 2^3P_2$ line a saturation absorption spectroscopy (SAS) is used, whereas the laser driving the $2^3S_1 \rightarrow 3^3P_2$ transition is locked by the polarisation spectroscopy [80]. Both of these methods have their advantages and disadvantages and their comparison can be found in Max Ebner's PhD Thesis [45]. Nevertheless, the robustness against external influences of the SAS signal was the reason for its utilisation in the stabilisation setup of the infrared laser.

We use an open-ended glass cell[14], where helium, at partial pressure[15] of 1.2×10^{-1} mbar, is being constantly pumped. Due to the temperature drifts, pressure in the cell changes, leading to alteration of the magnitude of the absorption signal on a timescale of minutes. The glass cell has a length of 11 cm and a diameter of 2.5 cm. We use a tightly wound coil around the cell where we deliver up to 2 W of rf power at 31.5 MHz to induce discharge and to populate enough helium in the 2^3S_1 state to obtain a spectroscopy signal. The cell is covered by three layers of μ-metal to block any dc-magnetic field components. Additionally, we place it inside a hollow copper block to prevent rf field from radiating in the laboratory. A schematics of the setup for the SAS is shown in Fig. 2.9a and a typical signal is shown in the inset of Fig. 2.10.

[13] Now belongs to NK Photonics.

[14] Recently, we were able to produce a closed helium spectroscopy cell, though we have not been able to sustain discharge for long enough time.

[15] The pressure window where the radio-frequency radiation excites enough helium atoms to the metastable state to perform spectroscopy is roughly 10^{-1} mbar. At higher pressure the discharge is quenched.

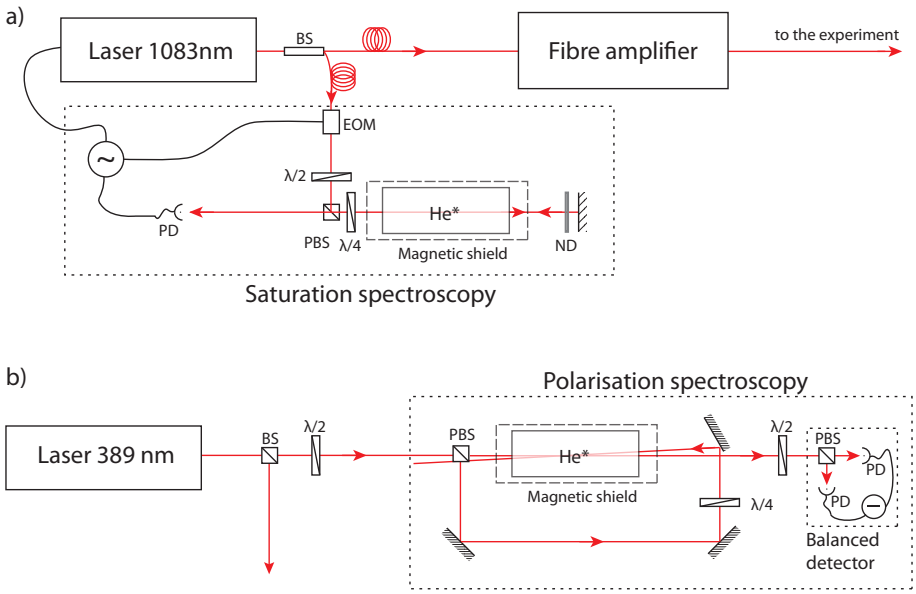

FIGURE 2.9. a) A schematic diagram of the saturated absorption spectroscopy of the $2^3S_1 \rightarrow 2^3P_2$ transition. An electro-optical modulator (EOM) modulates the phase of the laser light introducing sidebands. The light is detected by a high-bandwidth detector (PD) whose demodulated signal is proportional to the derivative of the absorption peak (see Fig. 2.10). b) Setup for a polarisation spectroscopy of the blue laser. An error signal is obtained directly from the output of the balanced photodetector.

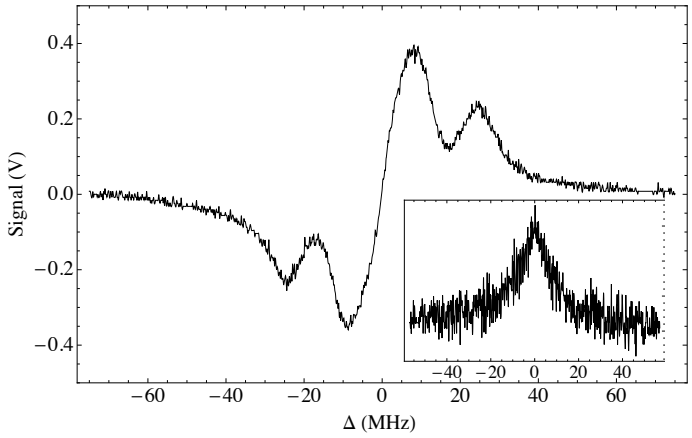

FIGURE 2.10. A typical error signal from saturated absorption spectroscopy after demodulation with a FWHM width of 20 MHz. An inset shows the Doppler-free spectroscopy signal before the demodulation.

To generate an error signal from the SAS for locking of the laser frequency on the $2^3S_1 \rightarrow 2^3P_2$ line, we use a Pound Drever Hall (PDH) technique. We split the output of the fibre laser using a fused fibre splitter and then we modulate the phase of the light with a fibre-integrated electro-optic modulator[16], EOM, (Photline NIR-MPX-LN-0.1) with a small amplitude at 40 MHz. This introduces sidebands to the carrier frequency. The spectroscopy signal from the high-bandwidth photodiode (Newport 1817FS) is then demodulated (by Toptica PDD100) to recover the error signal, which is then passed to the PID controller that is connected to the modulation input of the fibre laser, stabilising its frequency. The FWHM of the resulting error signal is 20 MHz. It is mainly influenced by power and pressure broadenings. Even though the signal-to-noise ratio is not perfect, this method of frequency stabilisation is robust to external influences, as the error signal is automatically centred around the absorption peak[17]. Having such a broad error signal it is important to avoid fluctuations of the set point, as it leads to a deviation in the estimate of the number of atoms (see Sec. 2.5.1).

Polarisation spectroscopy is used to obtain an error signal for locking of the diode laser. Its setup is depicted in Fig. 2.9b and is based on previous work [81, 82]. It consists of two counterpropagating beams in a spectroscopy cell—a circularly polarised pump and a linearly polarised probe beam. The pump creates an anisotropy in the medium that yields a rotation of the polarisation of the probe after traversing the sample, as its circular components experience an optical birefringence. The absorption coefficients are also different for both circular polarisations, which results in a circular dichroism. The two orthogonal polarisation components of the probe light are then detected with balanced photodiodes. The difference between these two detector outputs gives an error signal.

2.4.2. Beam layout

We use a 1083 nm wavelength with 3.5 W of laser power for the whole experiment. The abundance of laser power enables us to use optical fibres in the setup. Not only do they increase the stability of the experiment, but also decrease the complexity of the setup. The laser beams for each stage of the experiment are prepared on a separate optical table and are sent to the experiment via single-mode polarisation-maintaining optical fibres. This enables us to efficiently prevent any stray light from reaching the experimental chamber. The layout of the laser beams on the optical table can be seen in Fig. 2.11. We are using six acousto-optic modulators (AOMs) to produce the necessary frequency shifts. Every stage but the Zeeman slower is controlled by two AOMs. One AOM of the pair is aligned in a double-pass configuration such that we can vary the frequency in a certain range without any significant power loss and the other one is set up in a single-pass configuration. Table 2.2 summarises the AOMs and frequencies used in the experiment.

[16] As compared to free-space EOMs, fibre-based EOMs not only make alignment easier, but also require less power of the radio-frequency radiation.

[17] This is in contrast to the polarisation spectroscopy that we used earlier [45], where one obtains a dispersive curve at output of the photodiode. However, the offset of the error signal is prone to external influences (like pressure, temperature etc.) and the offset drifts over the course of the day causing frequency shifts.

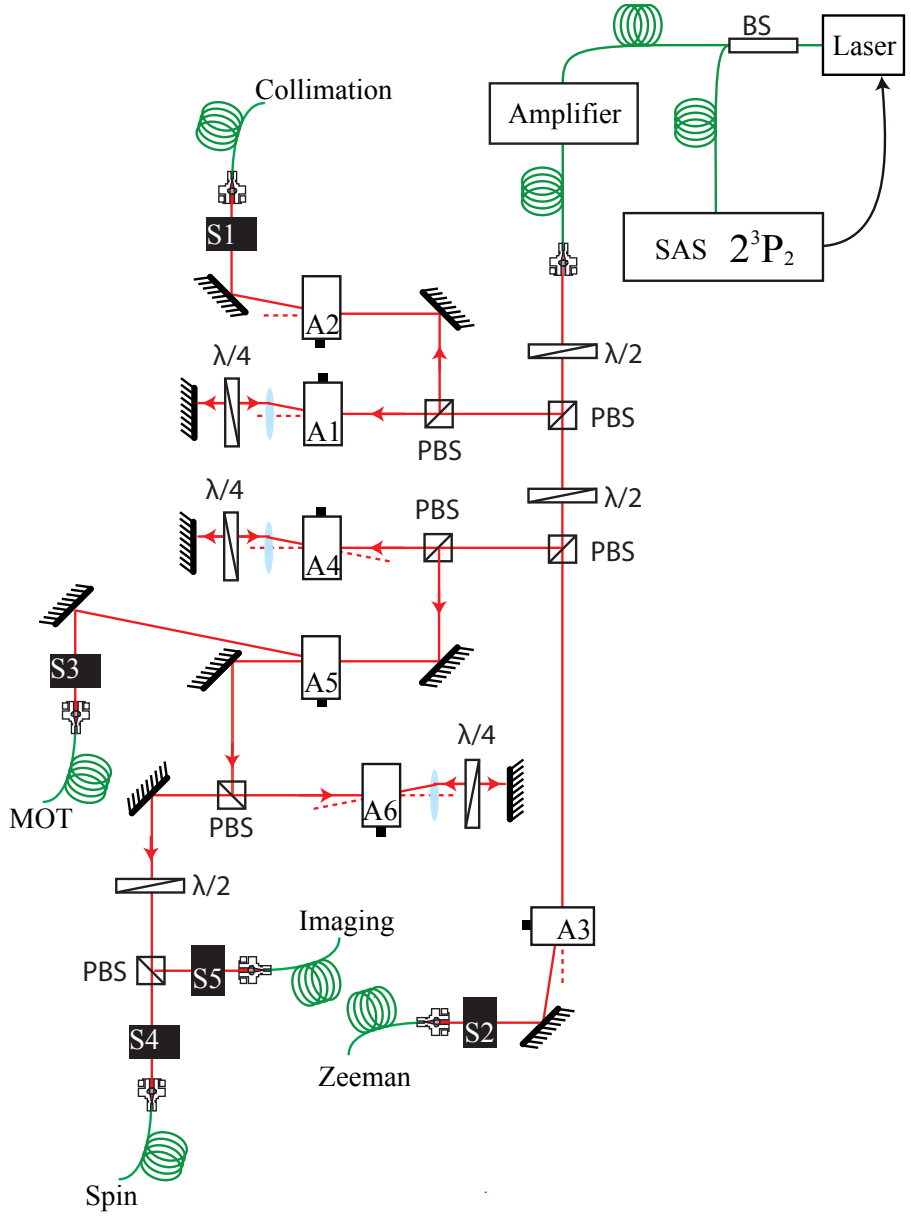

FIGURE 2.11. Schematic of the optical table, with A1-A6 the acousto-optic modulators and S1-S5 the mechanical shutters. Except for the Zeeman slower all stages of the experiment were set up such that they offer flexibility in frequency in a relevant range. Some lenses and mirrors are not drawn. The error signal from the spectroscopy (SAS) is fed to the piezo input of the fibre laser for frequency stabilisation.

It is worth noting that some AOMs are used multiple times in different, temporally-disjoint sections of the experiment, but with different frequencies.

The collimation beam is expanded to 6 mm and split in free space around the source part of the vacuum chamber. Fibres for the Zeeman slower and imaging are attached to the telescopes (Schäfter Kirchoff) that are directly mounted on the viewports of the vacuum chamber. The imaging beam has a beam waist of 3 cm, whereas the slower beam with initial waist of 3.6 cm is focused one metre behind the skimmer to circumvent transversal heating in the Zeeman slower (see Sec. 2.2.3). The rest of the fibres are connected to the fibre cluster (Schäfter Kirchoff).

Figure 2.12 shows the beam layout in the fibre cluster, that is used for the MOT, optical molasses, spin polarisation and 1D cooling. Since spin polarisation and 1D cooling are used in the magnetic trap, their polarisation is not necessarily the same as in the MOT beams, in fact polarisation of one of the beams has to be switched during the experimental run to match the quantisation axis. For the MOT and optical molasses the power is split into six beams of equal intensity[18] that are coupled again to the respective fibres. These fibres are attached to the telescopes expanding the beams to 5 cm, $1/e^2$ diameter. These telescopes are mounted on the viewports of the vacuum chamber, as can be seen in Figs. 2.8 and 2.31. Spin and 1D beams are split into two beams of equal intensity but orthogonal polarisation, and are positioned along the quantisation axis of the magnetic trap (y axis in Fig. 2.8). Every telescope used in the experiment has an integrated adjustable quarter-wave plate placed right after the fibre tip.

All the beams are switched with AOMs within a few µs, but to ensure that no stray light reaches the experimental chamber, five mechanical shutters (Stanford Research Systems, SR475, c.f. Fig. 2.11) are used to block laser beams on a timescale of a few ms.

2.5. Detection

We have two means of detecting and analysing the cold atomic cloud: by absorption imaging and by using a delay-line detector (DLD). While the former has been used in various experiments from the dawn of ultracold-atomic physics, the latter opens up new possibilities of characterisation as well as detection of the cloud.

2.5.1. Absorption imaging

Theoretical considerations

In this technique a weak, collimated laser beam, propagating along x direction, illuminates the atomic cloud with density n, gets absorbed and then is imaged on a camera. Thereby the intensity of the laser beam is reduced and using Lambert-Beer law it can be written as

$$\frac{dI}{dx} = -\sigma_a n I, \tag{2.5}$$

[18] In fact, due to the presence of 50:50 beam splitter in one output we split the light into seven beams, one of which remains redundant and enables quick power checks.

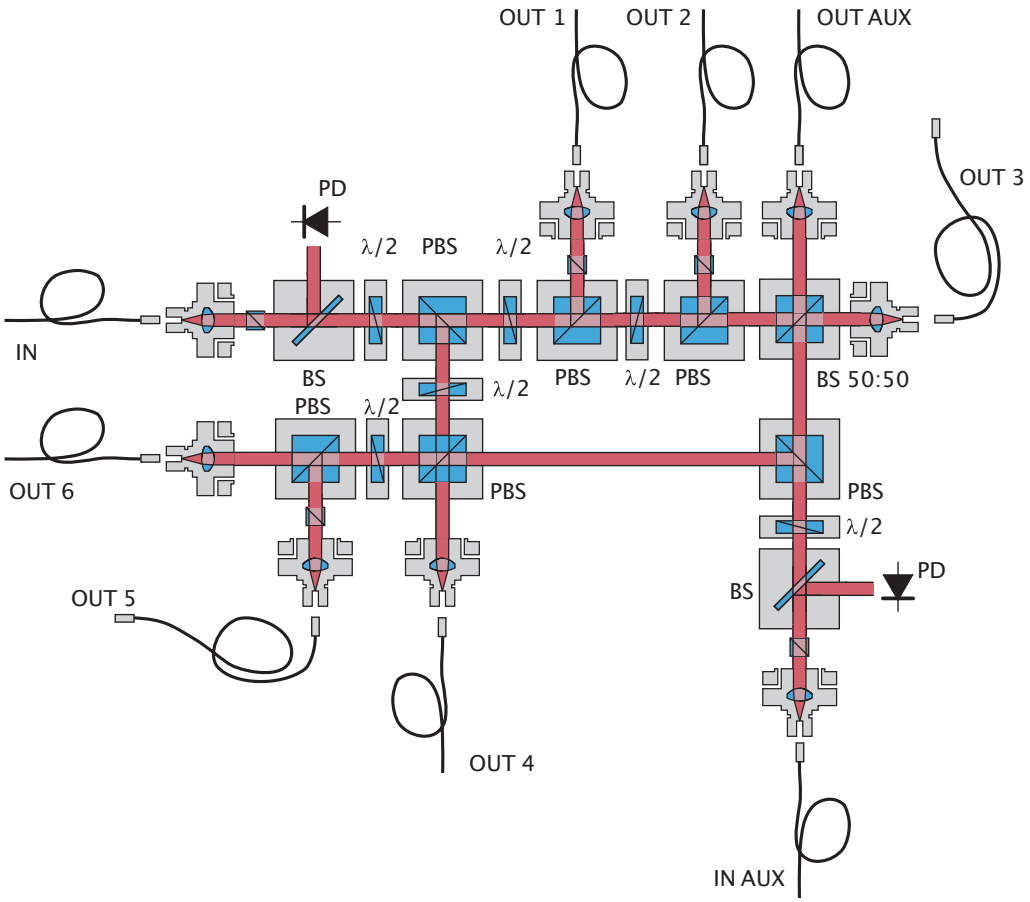

FIGURE 2.12. Fibre cluster used for the MOT, optical molasses, spin polarisation and 1D cooling. It has two inputs that are split up to seven outputs. At each input (IN) a fraction of power is split to a photodiode (PD) with which the input power can be monitored. Each input as well as outputs (OUT) 1, 2 and 5 contain a linear polariser that ensures proper coupling and maintaining of the polarisation. Outputs 1-6 are used for the MOT and optical molasses, whereas only 3 and 4 are used for spin polarisation and 1D cooling since these steps are performed only in one dimension. Due to the fact that the two latter steps are performed in the magnetic trap, the polarisation has to be switched in the output 4. One output is auxiliary due to the presence of a 50:50 beam splitter.

TABLE 2.2. Acousto-optic modulators used at various stages of the experiment, labelled as in Fig. 2.11. Frequencies as well as laser power that are used for different stages of the experiment. The detunings have been measured in heterodyne beat experiments and are given for the unshifted transitions.

Section of the experiment (AOM label)	Detuning (MHz)	Power before the optical fibre (mW)	AOM model
Collimation (A1,A2)	0	120	Brimrose TEF-55-20-1.08, Brimrose TEF-80-30-1.08
Zeeman slower (A3)	-370	200	IntraAction ATM-4001A2
MOT (A4, A5)	-41.5	1500	Brimrose TEF-40-10-1.08, Isomet 1201E-2
Molasses (A4,A5)	-5	1	
Spin polarisation (A5, A6)	+20	10	Brimrose TEF-40-10-1.08, IntraAction AOM-402AF3
1D Doppler cooling (A5, A6)	+31	1	
Imaging (A5, A6)	+4	2	

where σ_a is the photon scattering cross section, which in the low intensity limit $I \ll I'_{sat}$ is given by

$$\sigma_a = \hbar\omega \frac{\Gamma}{2I'_{sat}}, \tag{2.6}$$

with I'_{sat} being an effective saturation intensity. Following a thorough derivation by Tol [83], this can be written as

$$I'_{sat} = I_{sat} \frac{f}{\chi}, \tag{2.7}$$

where χ is the line-shape factor, f is a rational number found by solving rate equations [83] (alternatively an analytical expression can be found in [84]) and

$$I_{sat} = \frac{\hbar\omega\pi\Gamma}{3\lambda^2}, \tag{2.8}$$

is the saturation intensity of the atomic transition. The coefficient f is a polarisation and population dependent correction. If atoms are randomly aligned with respect to the quantisation axis, i.e. like in the magneto-optical trap, and the light is circularly (linearly) polarised then f changes from 18/10 (18/10) initially to 1 (17/10) in the steady state [83]. If all atoms are initially in the $m = \pm 1$ magnetic sublevel and the probe is circularly polarised then no population redistribution occurs, thus $f = 1$ throughout probing. For linear polarisation f starts at 2 and decreases to 17/10.

The line-shape factor χ contains all the information about the line shape of the transition and the line width of the laser. Moreover, it depends on the temperature of the sample, laser detuning, as well as an external magnetic field if the levels involved experience a Zeeman shift. In our case the laser line width is much smaller than the line width of the atomic transition and can be neglected. Thus, we assume that the laser is on resonance with the atomic transition $\Delta = 0$. Furthermore, due to the small mass of helium the contribution from the Doppler broadening cannot be neglected. Hence [83]

$$\chi(T) = \sqrt{\pi} u(T) \mathrm{e}^{u^2(T)} \mathrm{erfc}(u(T)), \tag{2.9}$$

with

$$u(T) = \frac{\lambda\Gamma}{4\pi} \sqrt{\frac{m}{2k_B T}}. \tag{2.10}$$

Around the critical temperature ($T_c = 1\,\mu\mathrm{K}$), χ approaches unity and has barely any effect on the line width. On the contrary, at the temperature of 1 mK (i.e. in the MOT and after loading of the magnetic trap) it broadens the line significantly, i.e. for 1083 nm transition in helium the natural line width $\Gamma/2\pi = 1.6\,\mathrm{MHz}$ becomes 4.1 MHz wide. More importantly if laser slightly off-resonance (for instance, due to the fluctuations of the error signal in the spectroscopy), i.e. $\Delta \neq 0$, then more general form of Eq. (2.9) has to be used.

Combining Eqs. (2.6) and (2.5) and staying in the low-intensity limit ($I \ll I'_{sat}$) we get

$$I_{out} = I_{in} \mathrm{e}^{-\hbar\omega \frac{\Gamma}{2I'_{sat}} \int n(\mathbf{r}) dx}. \tag{2.11}$$

The low intensity limit is important since we do not want to disturb the atomic sample with the probe light too much. In the case of helium already one scattered 1083 nm photon gives a recoil velocity of $v_{rec} = \hbar k/m = 9.2\,\mathrm{cm/s}$ and, as seen in Fig. 2.13, the absorption rate drops (especially at low temperature) with increasing number of absorptions, which results in images with worse contrast.

Fit functions

Thermal clouds

In order to determine the number of atoms, temperature and the cloud size, three pictures have to be taken: a raw absorption image $I_{abs}(y,z)$ of the cloud, a reference image where only the probe beam is present $I_{ref}(y,z)$ and a background image $I_{bgr}(y,z)$ with neither atoms or imaging light present for the noise subtraction. The transmittance is then

$$\frac{I_{out}(y,z)}{I_{in}(y,z)} = \frac{I_{abs}(y,z) - I_{bgr}(y,z)}{I_{ref}(y,z) - I_{bgr}(y,z)}. \tag{2.12}$$

The thermal cloud is assumed to have a Gaussian shape

$$n(x,y,z) = n_0 \exp\left(-\frac{x^2}{2\sigma_x^2}\right) \exp\left(-\frac{y^2}{2\sigma_y^2}\right) \exp\left(-\frac{z^2}{2\sigma_z^2}\right), \tag{2.13}$$

with central density n_0, axial rms radius σ_y and two radial rms radii σ_x and σ_z. The latter ones, due to the symmetry of the trap, are assumed equal. We apply for a short period of time a probe light with low intensity, thus combining Eqs. (2.11), (2.12), and (2.13) which results in

$$\frac{I_{out}(y,z)}{I_{in}(y,z)} = \exp\left[-\hbar\omega\frac{\Gamma}{2}\frac{1}{I'_{sat}}\frac{N}{2\pi\sigma_y\sigma_z}\exp\left(-\frac{(y-y_0)^2}{2\sigma_y^2}\right)\exp\left(-\frac{(z-z_0)^2}{2\sigma_z^2}\right)\right], \tag{2.14}$$

where $N = n_0(2\pi)^{3/2}\sigma_x\sigma_y\sigma_z$. This function is fitted to the transmission image with five free parameters: the centre of the cloud y_0, z_0, the rms radii σ_y, σ_z and the number of atoms N.

Bose gas and a BEC

As the cloud gets colder Bose statistics starts to play a role and its shape starts to deviate from a Gaussian. The thermal density distribution of an ideal (non-interacting) Bose gas is given by [85]

$$n_{th}(\mathbf{r}) = \frac{1}{\lambda_{dB}} g_{3/2}\left(\mathrm{e}^{\frac{\mu-U}{k_B T}}\right), \tag{2.15}$$

where μ is a chemical potential and $g_\alpha(x) = \sum_{k=1}^{\infty} x^k/k^\alpha$ is the polylogarithm function. For a gas confined in a harmonic potential

$$\frac{U}{k_B T} = \frac{x^2}{2\sigma_x^2} + \frac{y^2}{2\sigma_y^2} + \frac{z^2}{2\sigma_z^2} \tag{2.16}$$

and the gas has a thermal de Broglie wavelength $\lambda_{dB} = \sqrt{2\pi\hbar^2/(mk_BT)}$. Using Eq. (2.15) this can be expressed in terms of the number of atoms $N_{th} = \iiint_{-\infty}^{+\infty} n_{th}(\mathbf{r})d^3\mathbf{r}$ as

$$\lambda_{dB}^3 = \frac{(2\pi)^{3/2}}{N_{th}}\sigma_x\sigma_y\sigma_z g_3\left(\mathrm{e}^{\frac{\mu}{k_BT}}\right). \tag{2.17}$$

Using relation $\int_{-\infty}^{+\infty} g_\alpha(a\exp(-b(x+c)^2))dx = \sqrt{\pi/b}g_{\alpha+\frac{1}{2}}(a)$, for $b > 0$ and $c \in \mathbb{R}$ and integrating the density along $\hat{\mathbf{x}}$ which is the propagation direction of the probe beam, one obtains

$$n_{th}(y,z) = \frac{N_{th}}{2\pi\sigma_y\sigma_z g_3\left(\mathrm{e}^{\frac{\mu}{k_BT}}\right)} g_2\left(\mathrm{e}^{\frac{\mu}{k_BT}}\mathrm{e}^{-\frac{y^2}{2\sigma_y^2}-\frac{z^2}{2\sigma_z^2}}\right). \tag{2.18}$$

Hence Eq. (2.12) becomes

$$\frac{I_{out}(y,z)}{I_{in}(y,z)} = \exp\left\{-d_{th}g_2\left[\zeta\mathrm{e}^{-\frac{y^2}{2\sigma_y^2}-\frac{z^2}{2\sigma_z^2}}\right]\right\}, \tag{2.19}$$

where $\zeta = \exp(\mu/(k_BT))$ is the fugacity and d_{th} is the central column density. Equation (2.19) is fitted to the transmission image with three free parameters σ_y, σ_z and d_{th}. The number of atoms can be calculated from $N_{th} = 2\pi d_{th}\sigma_y\sigma_z g_3(\zeta)/\sigma_a$, where σ_a is the photon absorption cross section given by Eq. (2.6), and cloud radii evolve in time as

$$\sigma_i = \sqrt{\frac{k_BT}{m}\left(t^2 + \frac{1}{\omega_i^2}\right)}. \tag{2.20}$$

Below the critical temperature the density distribution of the condensate is found by solving Gross-Pitaevskii (GP) equation [85]

$$\imath\hbar\frac{\partial\psi(\mathbf{r})}{\partial t} = -\frac{\hbar^2}{2m}\nabla^2\psi(\mathbf{r}) + U(\mathbf{r})\psi(\mathbf{r}) + g_a|\psi(\mathbf{r})|^2\psi(\mathbf{r}), \tag{2.21}$$

with the mean-field interactions approximated by the $g_a|\psi(\mathbf{r})|^2$ term, in Thomas-Fermi approximation. In this approximation the mean-field interactions are dominant and the kinetic term can be neglected

$$\mu\psi(\mathbf{x}) = g|\psi(\mathbf{x})|^2\psi(\mathbf{x}) + \frac{1}{2}m(\omega_r^2(x^2+y^2) + \omega_z^2z^2)\psi(\mathbf{x}). \tag{2.22}$$

Thus, the density takes the form

$$n_{BEC}(\mathbf{r}) = \frac{1}{g_a}[\mu - U(\mathbf{r})], \tag{2.23}$$

where $g_a = 4\pi\hbar^2a/m$ is the interaction parameter a is the scattering length. The repulsive mean-field interaction is balanced by the external potential of the trap. In the case of a harmonic trap, the condensate has a parabolic density profile

$$n_{BEC}(\mathbf{r}) = \frac{15N_c}{8\pi r_x r_y r_z}\max\left(0, 1 - \left(\frac{x}{r_x}\right)^2 - \left(\frac{y}{r_y}\right)^2 - \left(\frac{z}{r_z}\right)^2\right). \tag{2.24}$$

Integrating this equation along the same direction as in Eq. (2.19) we get

$$n_{BEC}(y,z) = \frac{5N_c}{2\pi r_y r_z}\mathrm{Re}\left[\left(1-\left(\frac{y}{r_y}\right)^2-\left(\frac{z}{r_z}\right)^2\right)^{3/2}\right] \tag{2.25}$$

and the fit function for the BEC images becomes

$$\frac{I_{out}(y,z)}{I_{in}(y,z)} = \exp\left\{-d_{BEC}\mathrm{Re}\left[\left(1-\left(\frac{y}{r_y}\right)^2-\left(\frac{z}{r_z}\right)^2\right)^{3/2}\right]\right\}, \tag{2.26}$$

where r_y, r_z and d_c are fit parameters and the number of atoms can be obtained from $N_c = 2\pi d_c r_y r_z/(5\sigma_a)$. In the collisionless regime, the parabolic density distribution of the condensate remains during the expansion [86], and for a large aspect ratio the condensate size scales with time as (according to [87])

$$\begin{aligned} r_{\mathrm{rad}}(t) &= r_{\mathrm{rad}}(0)\sqrt{1+\omega_{\mathrm{rad}}^2 t^2}, \\ r_{\mathrm{ax}}(t) &= r_{\mathrm{ax}}(0)\left\{1+\left(\frac{\omega_{\mathrm{ax}}}{\omega_{\mathrm{rad}}}\right)^2\left[\omega_{\mathrm{rad}}t\arctan(\omega_{\mathrm{rad}}t)-\ln\sqrt{1+(\omega_{\mathrm{rad}}t)^2}\right]\right\}, \end{aligned} \tag{2.27}$$

where $r_i(0)$ is the so-called Thomas-Fermi radius, given by Eqs. (4.7), in radial and axial direction, respectively.

For partially condensed clouds we fit a function that is a product of Eqs. (2.19) and (2.26), assuming for the thermal component $\zeta = 1$ and $\mu = k_B T \ln\zeta = 0$. When a thermal component is present the temperature of the condensed cloud can be calculated either from time-of-flight (TOF) images of the expanding cloud or using TOF signal obtained with the MCP. Both methods were used in this thesis.

Looking at the structure of Eq. (2.11), it is seems natural that in order to extract a cloud density, one would take a logarithm of the experimental data. However, having images with a lot of noise, as it is in our case, it is important to fit images as they are, and not by taking their logarithm, as the noise in images is everywhere the same, the fitting error would be far greater in image sections with low transmittance. Hence, it would yield an incorrect fit.

Experimental setup

Absorption imaging is used to detect and analyse the whole ensemble of atoms in the cold atomic cloud. An EMCCD[19] camera delivers high detection efficiency ($\sim 30\%$) at 389 nm, which can be exploited for fluorescence imaging of the atomic beam. In contrast to the heavier alkali atoms absorption imaging of helium is much more delicate process. For the cold cloud with a limited number of atoms, the large momentum transfer of the blue light rapidly accelerates the atoms out of resonance with the imaging beam (compare Fig. 2.13). Technical limitations of the drivers of our AOMs set a lower limit on the length of the imaging laser pulses to about 60 µs. If the atoms are pushed out of resonance on a shorter time scale, the contrast in the image decreases, which cannot be compensated

[19] Electron-multiplying charge coupled device.

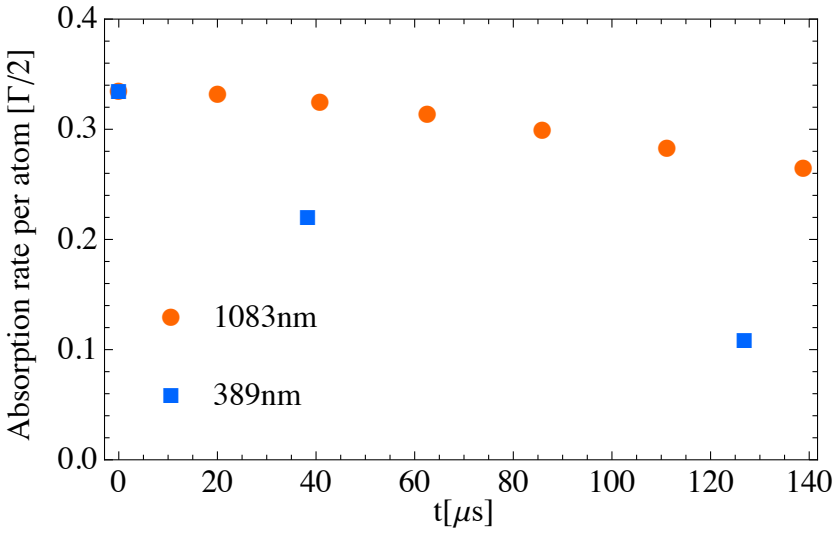

FIGURE 2.13. Calculated absorption rate per atom over time in units of the maximum possible rate $\Gamma/2$ at an intensity of $0.5\,I_s$. Due to the higher photon recoil for 389 nm photons (blue squares), the absorption rate drops much faster than for 1083 nm photons (red circles). The horizontal spacing between the dots indicates the average time between the scattering of two photons [88]. Therefore, by using the 1083 nm transition for absorption imaging of the atomic cloud, the atoms stay resonant and scatter photons for a longer time than in the case of 389 nm laser light.

for by a high detection efficiency. Instead we use $0.01\,I_s$ of resonant light at 1083 nm and image the shadow of the cloud. From the optical depth of the atomic cloud we deduce the number of atoms and from time-of-flight measurements obtain the temperature of the cloud.

For absorption imaging we use a 3 cm in diameter, σ^+ polarised laser beam. The laser beam is detuned such that it is resonant with the atoms after turning on of the quantisation axis. It enters the vacuum chamber through a viewport that is under a 22.5° angle with respect to the optical table. A magnetic field in xz plane, that introduces a quantisation axis for imaging, is produced by two sets of offset coils (see Fig. 2.14). An Andor[20] iXon EMCCD camera is used for image acquisition. It has 1004×1002 pixels whose size is $8\,\mu\text{m} \times 8\,\mu\text{m}$. Its quantum efficiency at 1083 nm is approximately 0.1%[21], but it is sufficient to image clouds with a weak probe beam. The CCD chip of the camera is

[20]Now is part of Oxford Instruments.
[21]Private communication with Andor Technology.

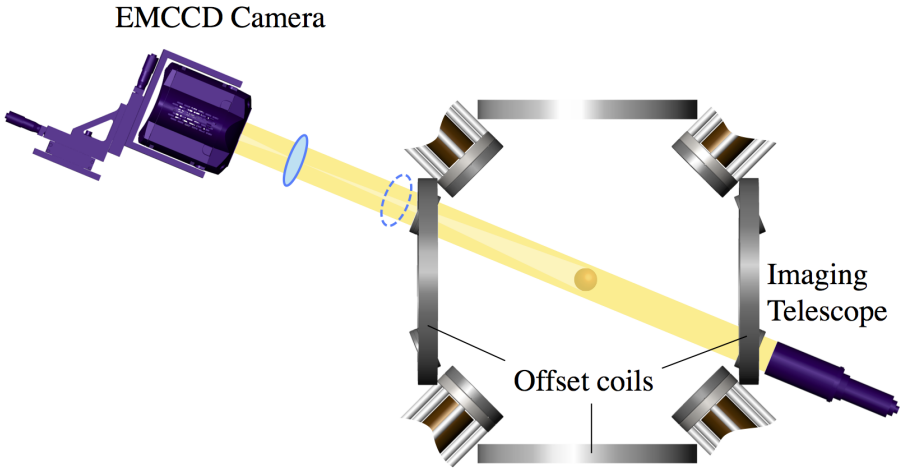

FIGURE 2.14. Setup for the absorption imaging. The EMCCD camera and the telescope are marked in purple. We use two lenses with foci 12.5 cm and 15 cm (dashed) giving magnification of 1/4 or 1, respectively. The offset coils create a uniform magnetic field to introduce the quantisation axis along the laser beam that is needed to drive the σ^+ transition.

exposed thrice for 150 µs[22] with the temporal separation of 45 ms[23]. The first two images (absorption and reference images) are taken with the laser pulses lasting 60 µs. In between these two images no additional laser pulse is needed to blow atoms away, as the helium cloud expands fast enough after the momentum kick from the first pulse. The last picture is taken with no laser beam to identify stray light and electronic thermal noise in the camera picture.

Great care has to be taken to keep the imaging light on resonance, though the width of the spectroscopy signal for 1083 nm light is 20 MHz (corresponding to roughly 10Γ). For instance a shift of 0.1Γ, which corresponds to a shift of the lock point by only 1/100 of the amplitude, would introduce a systematic error in the number of atoms of roughly 10%. Because of this and other error sources we will assume throughout the thesis an error in determination of the number of atoms to be 20%, unless otherwise noted.

Since the size of the MOT after few ms of expansion can easily exceed the size of the probe beam, we use a lens with 12.5 cm focal length that gives an effective magnification $M = 1/4$. Smaller and colder clouds (including BEC) can be imaged using a lens with a 15 cm focal length that gives a 1:1 image ($M = 1$). The magnification of the optical system has been verified by imaging a free-falling BEC during a known period of time. Both lenses are AR-coated achromatic doublets. The camera is fan-cooled to −55 °C for optimum noise performance. An infrared long-pass filter (> 1060 nm and a transmission

[22]This time is longer than the actual illumination of the atoms by the laser beam, due to the uncertainty between the trigger pulse and the actual start of the exposure as well as due to the technical limitations of the camera.

[23]We want to take these images in a quick succession to avoid laser power fluctuations. Yet this time is the shortest possible interval, being limited by the readout time of the previous image from the CCD chip.

$T = 90\%$) is mounted in front of the camera CCD chip to minimise background noise due to the presence of stray light.

2.5.2. Delay-line detector

Experimental setup

The key element in our setup is the delay-line detector (DLD) shown in Fig. 2.15, which allows for single-atom detection. It is commercially available, custom-made system produced by Surface Concept. It consists of a micro-channel plate with delay lines beneath it and (in our case) read-out electronics attached to them. The DLD is split into four independent quadrants, each having separate electronics. The detector is specified for count rates of 80 MHz and is mounted 80 cm below the trap. It can be moved by ± 17 mm with a resolution of 10 nm in the xy-plane by a translational stage (SmarAct SLC-2460-S-UHV) and rotated continuously with a resolution of 0.4 mrad by a rotational stage (SmarAct SR-3610-S-UHV).

Micro-channel plate

The detection process starts at a micro-channel plate (Photonis), which emits an avalanche of electrons when hit by a highly energetic particle. The plate consists of an array of tiny glass tubes, tens of microns in diameter, that are cut into millimetre thick slices. The top and bottom surfaces of these plates have a metallic coating in order to provide an electric connection to all channels. The inner surface of the channels in some MCPs is coated to lower the work function and facilitate ejection of the electrons, yet these coatings are very fragile and their lifetime is a limiting factor of their durability. Therefore we decided to use an uncoated MCP. The application of high voltage turns each channel into a dynode electron multiplier and provides electrons to depleted channels via strip currents. The ejected electrons are then accelerated in the electric field and, due to the fact that channels are slanted by several degrees, eject secondary electrons creating an avalanche. Because of the low mass of the electrons as well as low thickness of the MCP the process takes around 100 ps and the gain achieved saturates around $10^3 - 10^4$. In the case of He^* de-excitation is mainly due to the Auger process [89], where, during a collision with the surface, an electron bound to the atom decays to a ground state. The energy released during the process is either absorbed by the lattice of the solid or one electron of the solid is captured to an atomic bound state and the energy is absorbed by the atomic excited electron which may be ejected.

To increase the amplification one could in principle increase the voltage, but this at some point leads to destructive arcing. In order to overcome this, typically a stack of two (Chevron configuration) or three (Z stack) MCPs is used. The MCPs are aligned such that the angles oppose each other (for clarity see Fig. 2.16). This increases the gain without affecting the quality of the detection. Furthermore, this solves another problem: no particle can cross the MCP without hitting the wall of the channel[24].

[24] In the case of a single MCP, if a particle is flying at an appropriate angle it can fly through the MCP without touching any channel surface.

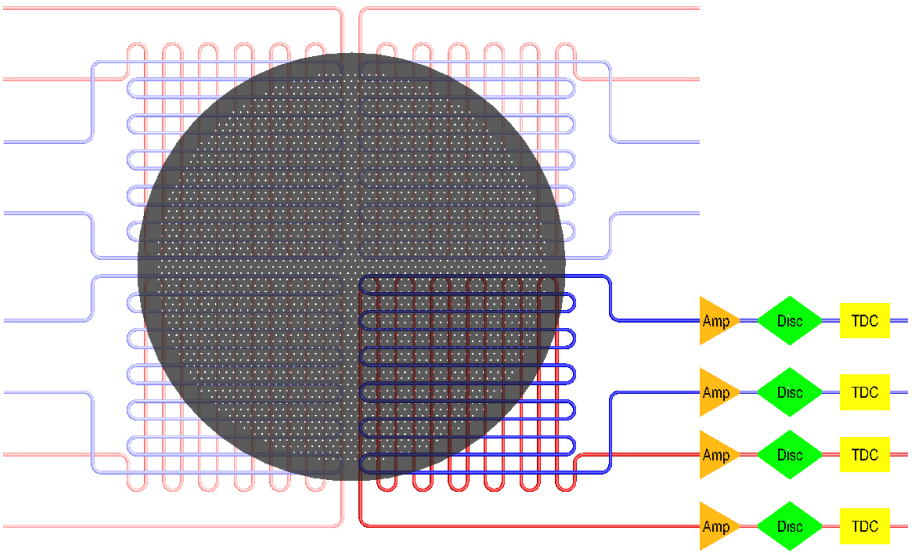

FIGURE 2.15. (Top view) Schematic of the delay-line detector (DLD) consisting of four quadrants with independent delay lines and read-out electronics. When an electron avalanche hits the delay lines located underneath the MCP, it creates an electronic signal that propagates along the wires in both directions. After preamplification, pulse discrimination and time-to-digital conversion (TDC), the four arrival times are recorded. Due to a constant propagation speed of the electronic signals along the delay lines, the arrival position of the helium atom can be deduced from $t_{x1} - t_{x2}$ and $t_{y1} - t_{y2}$. The arrival time of the atom at the detector is determined by taking the average of the four recorded times. The active region of the MCP has a diameter of 80 mm, the delay-lines of each quadrant extend over rectangular regions with a size of 45 mm × 48 mm with a separation between two neighbouring quadrants of below 1 mm. However, a region of approximately 5 mm in between the quadrants has to be discarded. As the signal cannot be reliably read out from curved sections of the delay lines.

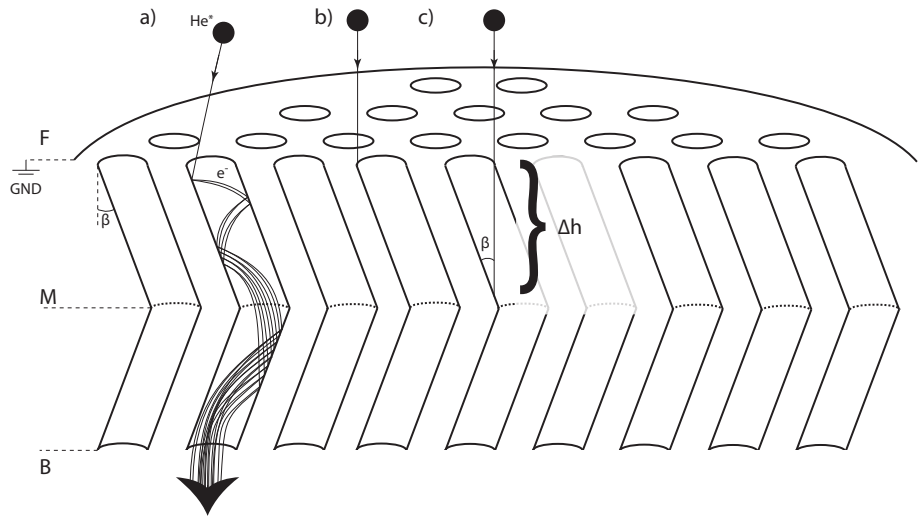

FIGURE 2.16. A cross-section through two micro-channel plates in a Chevron-stack configuration. The MCPs are aligned such that their bias angles β oppose each other and no particle can fly through without hitting the inner wall of the channel. In our detector the front (F) side of the MCP is grounded, while to the middle plane (M), the back side (B) of the MCP, and the anode (not shown) high voltage is applied. (a) A metastable helium atom falling onto the micro-channel plate (MCP) gets deexcited due to an Auger process and is likely to cause the emission of an electron that can be amplified to an electron avalanche in one of the channels. (b) and (c) show a particle hitting an MCP channel in two different scenarios: (b) right on the edge of the channel, (c) enters the channel on the other side of the diameter and hits the wall after falling $\Delta h = 72.6\,\mu\text{m}$ deeper. This can lead to a difference in the arrival times of $18\,\mu\text{s}$.

As mentioned before, the amplification of a single channel saturates which influences the detection of the following particles. This is caused by the local electronic depletion of the channels that strongly influences the amplification, i.e. not only the channel where a particle hit is affected, but also the neighbouring channels. It is compensated by the strip current, yet due to the high resistance of glass this current is quite low. The strip current can be increased by coating the walls of the channels. Another possibility would be to decrease the diameter of the channels while keeping the open-area ratio the same. This would increase the number of channels, but would reduce the area where the electronic depletion happens.

Delay line and readout electronics

The readout of the electronic avalanche can be done either by a phosphor screen or a delay-line anode [90–93]. Each of them has strong and weak points. A phosphor screen together with a CCD camera recording the phosphorescence allows for imaging of the cross sections of the falling cloud. Moreover, due to its optical resolution it can resolve very

tiny structures in the cloud and there are no problems with simultaneous events, even at a flux of particles exceeding 10^7 events per second. On the other hand, due to the large amount of data it has to transfer, its temporal resolution is limited by the frame rate of the camera to, typically, 20 ms. This makes 3D reconstruction of the cloud momentum space difficult. Another way of reading out of the electronic avalanche is by using a delay line. A delay line is a wound wire at which the electronic avalanche creates electric pulses that propagate towards both ends. From the arrival times of these pulses the position of the particle can be calculated. Delay lines have an excellent temporal resolution, that enables a very good reconstruction of the initial momentum of the atoms. Yet its spatial resolution is limited by the timing of the readout electronics as well as a dead time[25].

We chose to use a delay-line detector due to its three dimensional reconstruction capabilities and excellent temporal resolution, 220 ps in our case. The specialty of our DLD design is having the delay line itself split into four quadrants, each equipped with independent read-out electronics. This overcomes the dead time for particles not falling onto the same quadrant. Hence, true simultaneous detection of atoms registered at different quadrants can be achieved, which will be especially useful for quantum correlation experiments with a directed emission of particles. The delay-lines are not wound helically, but are meander-shaped. This decreases the propagation time of the pulses by a factor of two which translates to a better precision in determining the timing and a shorter dead time. One delay-line measures coordinates in only one direction, thus to obtain the x and y information about particle's position a second delay-line is used, which is placed right below the first one. Due to the propagation of the electronic signal along the delay lines, a dead time of 25 ns between two recordable events arises. Besides the dead time, electronic read-out and charge depletion of the MCP itself limits the burst count rate to a few $10^6\,\mathrm{s}^{-1}$. The specifications of our MCP as well as the underlying delay-line anode are summarised in Table 2.3.

The high voltage for the delay-line detector is provided by a dual high-voltage power supply. It contains two individual high-voltage modules (HV1 & HV2). Due to an internal resistor network the dual HV supply provides four positive high voltages adjustable between 0 V and up to +4 kV, though, their difference shall not be greater 1.5 kV. The front side (F) of the MCP is grounded (c.f. Fig. 2.16). The module HV1 controls the output voltage for the detector anode (A) in respect to the MCP front side (F), while the module HV2 controls the output voltage for the MCP back side (B) with respect to the MCP middle contact (M). The voltage for the MCP middle contact is related to the voltage of the anode via an internal resistor.

Subsequent recording of the arrival times of the electronic signal propagating along a delay line reveals its impact position and time. The pulses are then preamplified, shaped and discriminated by a constant fraction discriminator (CFD). The CFD transforms the pulses into a fast rising pulse sum that can be processed further. These are sitting as close to the detector as possible on the vacuum flange. The time-to-digital converter

[25]Because of the fact that one has to wait until the electric pulses arrive on the end of the delay line no other particle can hit the detector, otherwise it is very difficult (if not impossible) to assign appropriate pulses to a particle.

TABLE 2.3. Specifications of the MCP stack and of the delay-lines. Numbers taken from the data sheet, unless indicated otherwise.

MCP stack	Thickness (per MCP)	1.5 mm
	Active diameter	80 mm
	Pore size	25 µm
	Centre-to-centre spacing	32 µm
	Bias angle of channels	19(1)°
	Length-to-diameter ratio	60
	Open-area ratio	50%
	Typical gain	10^6
	Resistance	18.4 MΩ
Delay-line	Time-bin	6.8 ns
	Dead time[a]	25 ns
	Temporal precision[a]	220 ps
	Spatial precision[a]	177 µm

[a]Measured experimentally.

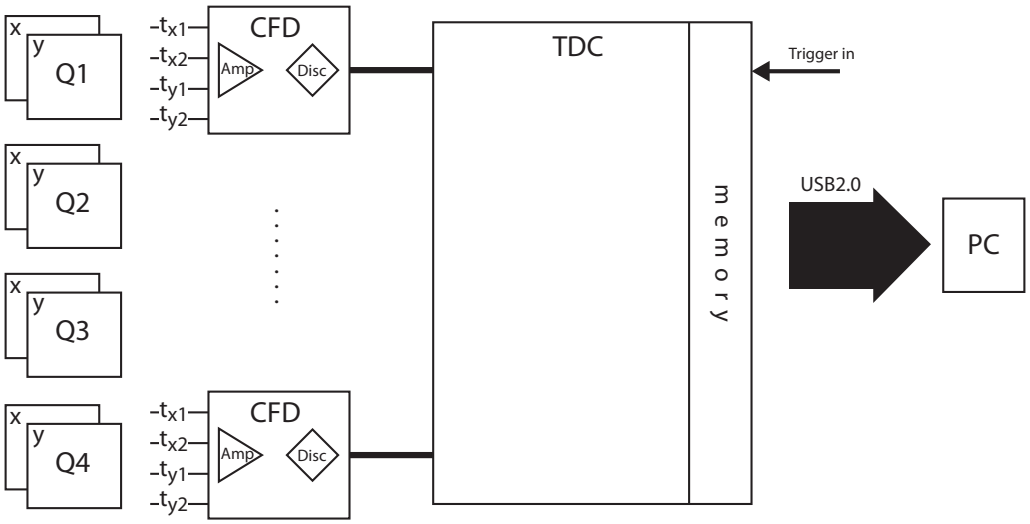

FIGURE 2.17. Schematic of the read-out of the pulses coming from delay lines. Each quadrant has 4 outputs coming from 2 delay lines. These signals are amplified (Amp), discriminated (Disc) and shaped appropriately in the constant fraction discriminator (CFD). Then a time-to-digital converter (TDC) transforms the analogue signals to a digitised information which is written to an internal memory. After each acquisition the data is transferred from the memory to the imaging PC via an USB2.0 connection.

(TDC) converts signals that are coming from the CFD to a digitised time information. Subsequently it can assign the coordinates to the particles or send the raw data further via USB connection to the computer. In principle the transfer rate of the USB limits the count rate to 2 MHz. However, if the count rate is so high that the USB connection becomes a bottleneck, an internal memory is used to store the large amount data and transfer it to the computer after the burst. Our TDC is running with a 80 MHz clock which at present is a limiting factor to the maximum data rate.

The CFD produces a fast rising pulse, and sends it further to the TDC, when the analogue signals reach a certain fraction of the maximum pulse height. The pulse recognition does not depend solely on the amplification of the MCP, but also on the ability of the delay lines to collect the electrons, which depends on the electric potential that is applied to the anode.

In order to determine a position in x and y, the arrival times of pulses per event at the four ends of each DLD meander/quadrant are subtracted (x: $t_{x_1} - t_{x_2}$; y: $t_{y_1} - t_{y_2}$). The TDC stop signals are grouped internally in pairs to form x and y. Time measurements are performed by summing up the arrival times of pulses at the end of the DLD meanders, i.e. the same results which are used to determine positions for each event are summed. The results of all these time sums correspond to $t_{sum} = t_{x_1} + t_{x_2} = t_{\mathrm{offset}} + n(t_{\mathrm{hit}} - t_{\mathrm{ref}})$, where $(t_{\mathrm{hit}} - t_{\mathrm{ref}})$ is the time of interest (e.g. time of flight) in a given experiment, n is the number of summed time results[26], and t_{offset} is a device related constant, which depends on cable lengths, electronics propagation times, experimental setup etc.. Hence it is possible to completely determine position and time of each event from only four precise time measurements. From the spatio-temporal information of the detection event, the momentum-space distribution of the atoms can be reconstructed (Fig. 2.18), which will be an essential element for future correlation experiments. This reconstruction, though, can only be performed if all four signals arrive to the TDC. If one of them is lost on the way or does not pass through CFD then this event is rejected. Also, if electric pulses from two (or more) independent events overlap in one of the channels, there is no possibility of distinguishing between these events; thus only one of those events will be registered. This gives rise to the aforementioned dead time of 25 ns and in the detection of very dense clouds can be observed as a saturation of the detector[27] as seen in Fig. 2.19. The reason for Quadrant1 not showing any visible saturation in Fig. 2.19 is probably the fact the atomic cloud is not perfectly centred on the detector. The difference in the pulse height between the quadrants probably results from ageing of the MCP that delivers lower than expected amplification. This leads to analogue signals of different heights along the DLD which leads to miscalibration of the CFD electronics. For this reason either the voltage on the MCP has to be increased, electronics has to be recalibrated or the MCP has to be replaced. At the moment the MCP is operated with a maximum voltage and increasing it further did not improve the count rates.

From this data we were also able to estimate the maximum number of counts that our detector can handle. It is approximately 1 MHz per quadrant which is far from the

[26] In this case $n = 1$, though one could also add arrival times in y direction.

[27] This happens at a lower count rate than the saturation of the MCP.

specified 20 MHz per quadrant. One of the reasons for this discrepancy might be that the specifications are relate to counts uniformly separated both in space and time, whereas our cloud falls at high density over short period of time.

DLD characterisation

Precision

We measured a temporal precision of 220(18) ps and a spatial precision of 177(32) µm. The measurement of the temporal resolution has been performed by shining a picosecond mode-locked UV laser on the quadrants of the detector and analysing the fluctuations of the registered detection events around the laser repetition rate. Even though the temporal precision of our detector translates to a 1 nm of resolution in vertical direction, it does not translate to the spatial resolution as directly as one would expect from the measured values. Experiments reported so far show that the temporal resolution is indeed better than spatial [28], but nobody was able to characterise it with slow particles. We suspect that this lower-than-expected temporal precision might result from the finite size of the channels. As shown in Fig. 2.16 particles do not always eject an electron at the edge of the channel. Often MCPs are used in high-energy applications where particles travel so fast that the position where the particle hits the channel is negligible. Yet for slow particles (as is the case with ^{4}He*), it matters where the particle hits the channel. Let us consider two cases, depicted in Fig. 2.16, that clearly illustrate the problem. In one case a particle hits the channel directly at the entrance, in the second case the particle enters the channel on the other side of the diameter and hits the wall after traversing longer distance by $h = 72.6$ µm (the channels of our MCP have a bias angle of $\beta = 19(1)^\circ$). If we assume channel diameter of 25 µm and that the atoms fall freely from 80 cm above the MCP, the arrival-time difference between the two cases is 18.3 µs. Increasing the bias angle of the channels to 45° reduces the arrival-time difference to 6.2 µs. Further reduction can be achieved by making the channels smaller.

The spatial resolution has been measured in two ways: by a time-sum method [94, 95] and by placing a mask with 30 µm wide holes on top of the MCP and deconvoluting the obtained pattern with the size of the holes [45]. The time-sum method gives a rough estimate of the precision and is burdened by the systematic errors in the PSU. This measurement gave us a conservative value of 300 µm. To cross-check this value, we placed a mask in front of the detector and illuminated it with the cloud from the magneto-optical trap (MOT). This determined the precision to be 124(12) µm, which is plausible, taking into account the time-bin size of the time-to-digital converter (6.8 ps) or the spatial discretisation of our detector (about 30 µm), and represents the actual performance in our current setup. Spatial precision can be also increased electronically at the cost of worsening the temporal precision, which as shown in previous paragraph is limited by the MCP rather than electronics.

Even though the manufacturer of our detector claimed that our spatial precision might be up to a factor of two better than what we have measured, our detector is still better than the state-of-the-art helium experiments [28, 96]. In the time of writing of this thesis

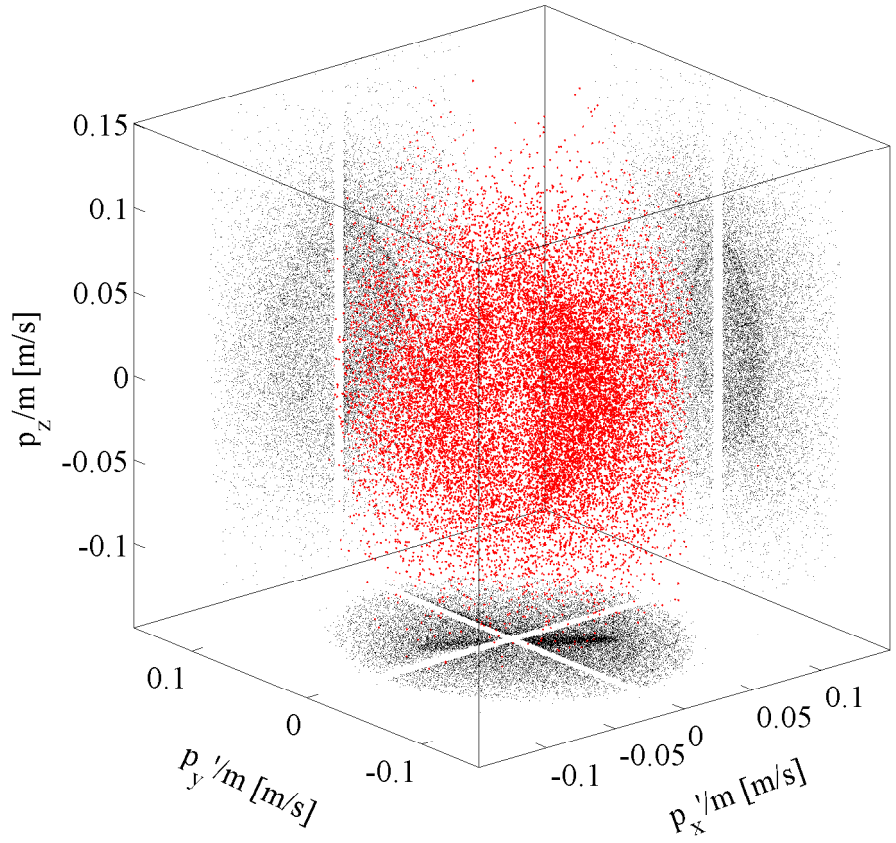

FIGURE 2.18. Reconstructed momentum space distribution of a condensed atomic cloud that was dropped onto the DLD, where each dot represents a single atom (in total about 3×10^4 for this measurement). Knowing the distance of the trap to the detector, the momentum of the atoms can be reconstructed. While no specific structure can be seen by the naked eye in the 3-dimensional plot, the 2-dimensional projections show the higher density of the condensed part of the atoms. The four different quadrants of the detector can be identified in the projections by the areas with no counts.

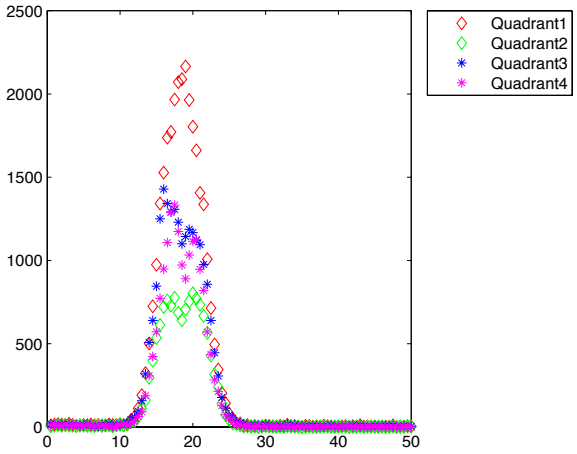

FIGURE 2.19. Histograms of the number of counts on each quadrant, taken from the same dataset as Fig. 2.18. Each dot represents the number of counts in a 0.5 ms bin. Every quadrant but Quadrant1 reveals saturation of the number of counts.

we were in the process of planning to implement the aforementioned changes to improve the spatial resolution as well as temporal.

Efficiency and uniformity

To determine the detection efficiency of the DLD we can link the sum of counts on the MCP with the number of atoms measured in the absorption imaging with the equation

$$N_{\mathrm{MCP}} = \alpha\xi(T)N, \tag{2.28}$$

where α is the detection efficiency that includes an open-area ratio of our detector (50%), $\xi(T)$ is a temperature dependent factor that takes care of the fact that we detect only a small volume of the falling cloud, and N is the number of atoms from absorption imaging. Having measured optically the number of atoms in the MOT and knowing the number of counts from the MOT cloud on the DLD we can estimate the efficiency to be $\alpha \approx 10\%$ which is in line with the reported efficiency by the French group [15, 95], although lower than the estimate of 30(10)% measured by the Australian group [97].

In order to test the uniformity of the amplification of the MCP we ran a MOT experimental sequence, where after switching off the magnetic trap, we dropped the cloud onto the MCP. We repeated this sequence 100 times and its results are shown in Fig. 2.20. The MOT cloud is so hot that provides a uniform number of particles across the detector, thus the count rate will solely depend on the amplification of the MCP and the calibration of the electronics. Figure 2.20 shows that there are some differences in gain across the four quadrants, but across each quadrant the amplification is relatively uniform (apart from the inner edges). Thus, these differences likely stem from the readout electronics and not

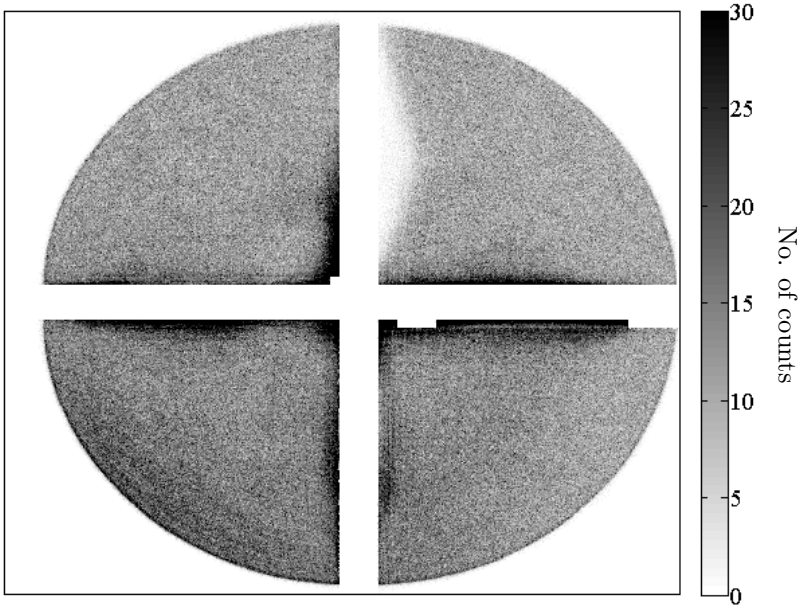

FIGURE 2.20. Uniformity of the amplification of the DLD detector. This image contains 100 shots of the MOT cloud. Apart from the edges each quadrant shows a uniform gain across the surface. The difference in counts between each quadrant is likely caused by the calibration of the electronics reading out the signals from the corresponding delay lines.

from the MCP itself. This result is favourable for our experiment, as gain maps reported by the other groups show non-uniform amplification across the detector [95, 98].

Dark counts

Apart from some border effects on the edges of the quadrants (as in Fig. 2.20), the dark counts remain low (25 cps per quadrant) and are attributed to the residual gas in the chamber and thermal electrons being ejected from the material of the MCP. Ultimately the dark counts are limited by the energetic cosmic rays passing through the surface of the detector and the radioactive decay of the elements in the substrate of the MCP. Such a low dark-count rate shows the advantage of the DLD over other single-particle detectors, i.e. single-photon avalanche photodiodes, CCD cameras etc. The low dark-count rate of the DLD allows for feasible single-particle detection without the necessity of resorting to cryogenic temperatures.

Linear calibration of the DLD

The future entanglement experiments require precise determination of (x, y, t) coordinates of single-particle hits. However, as can be seen in Figure 2.22, the real-world DLD unfortunately does not provide as accurate spatial imaging as, for example, CCD cameras.

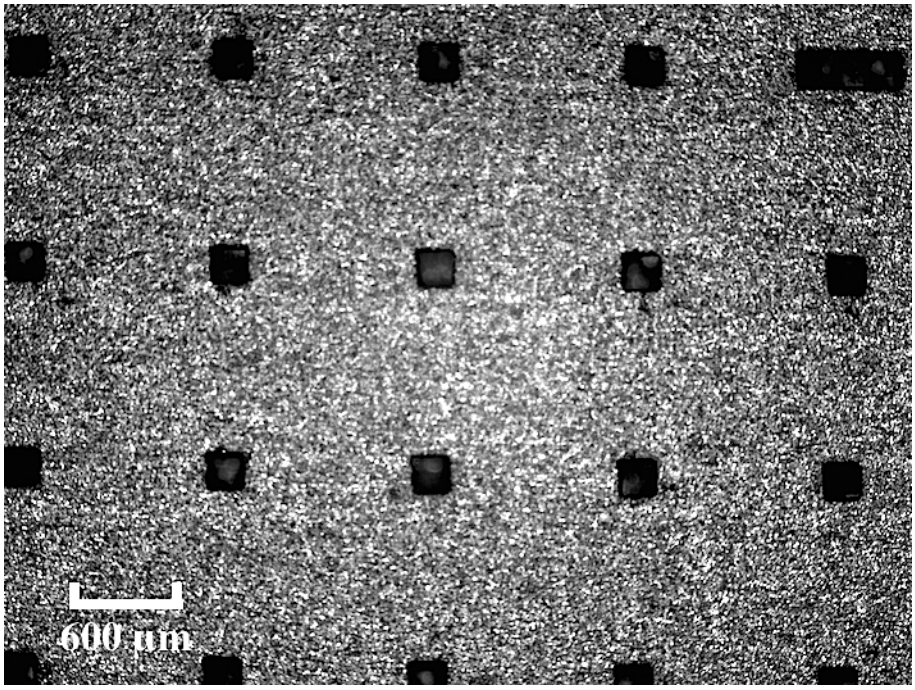

FIGURE 2.21. Scanning electron microscope picture of the laser-cut holes in a mask that is used for the linear calibration of the detector.

The image is distorted such that straight lines are not straight anymore, thus we had to perform a linear calibration of the detector. It enabled not only to straighten the imaged lines but also to quantitatively evaluate the unusable distance between the quadrants[28] to be 4.8 mm.

The calibration has been performed by placing a stainless steel mask (see Fig. 2.21), manufactured by KJ Laser Micromachining, containing equidistant, laser-cut square holes with a pitch 200 µm × 200 µm. The mask has been designed such that it had few rectangular holes (200 µm × 600 µm) that were used for alignment with respect to the DLD[29]. These holes were also used to precisely measure the distance between the quadrants. Scanning electron microscope (SEM) pictures of the mask are shown in Fig. 2.21. The mask was placed 2 mm above DLD. Subsequently the measurement has been performed by dropping a MOT cloud 1000 times to accumulate enough counts through the holes (the open area of the mask is approximately 3%).

The data were then summed into one picture. Firstly, the positions of the peaks are found which are used as apexes of vectors. The vectors spanning a quadrangle characterise the local deformation. Subsequently positions of the peaks are compared with the virtual grid of the peaks, which represents positions where the mask holes should have been. The

[28]Even though the physical distance between individual quadrants is less than 1 mm, in reality at the turning points of the delay lines, the position of the particles cannot be assigned precisely enough leading to a greater "dead zone".

[29]The rotational stage of the DLD made alignment straightforward.

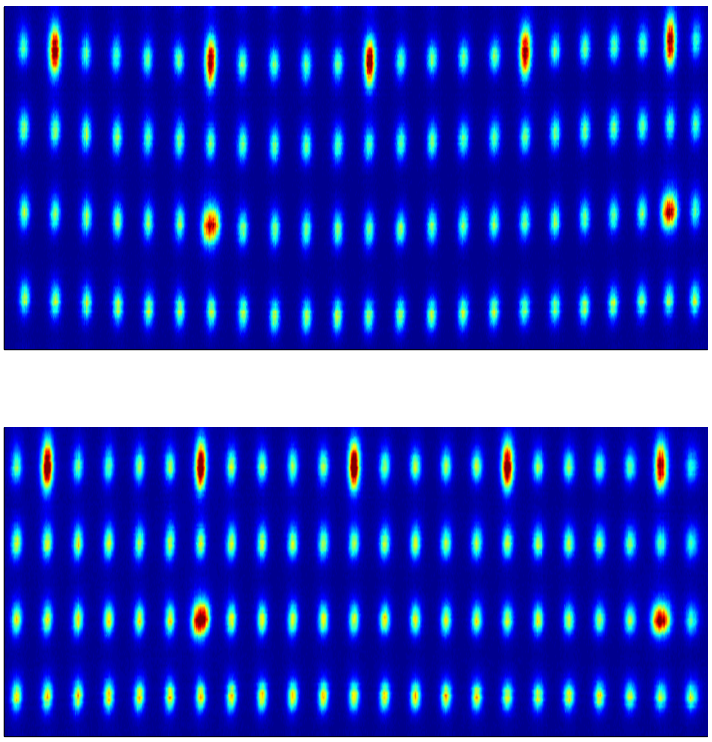

FIGURE 2.22. Imaging of the mask with uniform flux of atoms from the MOT. On top a slice of an uncorrected image is shown; the bottom image presents same slice of the image but with linearisation correction applied (see text for details). Similar distortions can be observed in the vertical direction.

pixels are then shifted such that the vectors from four neighbouring peaks span a rectangle. The detailed description of the used algorithm can be found in [99]. This way a map was created which can be applied to the taken data.

Fit functions for the time-of-flight signals

Thermal Bose distribution

For the derivation of the flux of atoms passing through the MCP we follow approach of Tychkov [100]. We treat the cloud as a point source that starts to expand at $t = 0$ after the magnetic trap has been switched off. At each instant of time we can write the flux through an area a as

$$\phi(t) = \int n(\mathbf{r}, t)\mathbf{v}(\mathbf{r}, t) \cdot \mathrm{d}\mathbf{a}, \tag{2.29}$$

where $n(\mathbf{r}, t)$ is the density and $v(\mathbf{r}, t)$ velocity distributions. We assume that the size of the cloud at $t = 0$ is point-like and atoms are experiencing a free fall influenced only by

gravity. We choose a cylindrical coordinate system with the origin in the centre of the atomic cloud with the gravity acting in $-\hat{\mathbf{z}}$ direction. The initial velocity is $\mathbf{v_0} = \{v_{0\rho}, v_{0z}\}$ and the position at time t is $\rho = v_{0\rho}t$, $z = v_{0z}t + gt^2/2$. We assume that the detector centre coordinates are $\{0, 0, -h\}$ and that it lies in the horizontal xy plane. Moreover, we can express $\mathbf{v} \cdot \mathrm{d}\mathbf{a} = (1/2gt + h/t)\,\mathrm{d}x\,\mathrm{d}y$, hence Eq. (2.29) becomes

$$\phi(t) = 2\pi \left(\frac{1}{2}gt + \frac{h}{t}\right) \int_0^{m_r} n(\rho, -h, t)\rho\,\mathrm{d}\rho, \tag{2.30}$$

where m_r is the MCP radius and ρ is the cylindrical coordinate.

We assume an ideal non-interacting Bose gas, with the density distribution given by Eq. (2.15). Inserting it to Eq. (2.30) yields

$$\phi_{th}(t) = \frac{2\pi}{\Lambda^3} \left(\frac{1}{2}gt + \frac{h}{t}\right) \int_0^{m_r} g_{3/2}\left(\zeta' \mathrm{e}^{-\frac{\rho^2}{2\sigma_\rho^2}}\right) \rho\,\mathrm{d}\rho, \tag{2.31}$$

with

$$\zeta' = \exp\left(\frac{\mu}{k_B T} - \frac{(-h + \frac{g}{2}t^2)^2}{2\sigma_z^2}\right). \tag{2.32}$$

Knowing that $\int_0^c x g_\alpha(a\mathrm{e}^{-bx^2})\,\mathrm{d}x = 1/(2b)[g_{\alpha+1}(a) - g_{\alpha+1}(a\mathrm{e}^{-bc^2})]$ (for $b > 0$), and integrating Eq. (2.31) results in a flux for an ideal Bose gas

$$\phi_{th}(t) = \frac{N_{th}}{\sqrt{2\pi}\sigma_z g_3\left(\mathrm{e}^{\frac{\mu}{k_B T}}\right)} \left(\frac{1}{2}gt + \frac{h}{t}\right) \left[g_{5/2}(\zeta') - g_{5/2}\left(\zeta' \mathrm{e}^{-\frac{m_r^2}{2\sigma_\rho^2}}\right)\right]. \tag{2.33}$$

At the condensation threshold, $T \leq T_c$, $\mu = 0$, whereas far from condensation threshold, when $T \gg T_c$ and $\mu \to -\infty$, Eq. (2.33) becomes

$$\phi_{th}(t) = \frac{N_{th}}{\sqrt{2\pi}\sigma_z} \left(\frac{1}{2}gt + \frac{h}{t}\right) \mathrm{e}^{-\frac{(-h+\frac{g}{2}t^2)^2}{2\sigma_z^2}} \left(1 - \mathrm{e}^{-\frac{(-h+\frac{g}{2}t^2)^2}{2\sigma_z^2} - \frac{m_r^2}{2\sigma_\rho^2}}\right), \tag{2.34}$$

which is the flux for a hot thermal cloud with a Maxwell-Boltzmann velocity distribution. Equations (2.33) and (2.34) are used to fit the time-of-flight data with fit parameters N_{th}, T and μ (if needed). The expected time-of-flight curves for a few temperatures of the cloud typically observed during the experimental run are presented in Fig. 2.23. After switching off the MOT, atoms have an initial peak velocity of approximately 2 m/s that is responsible for their rapid expansion and arrival on the detector 110 ms quicker than it is expected from the free fall. However, the colder the cloud the narrower the distribution of the arrival times is, and the atoms fall freely in the gravitational field.

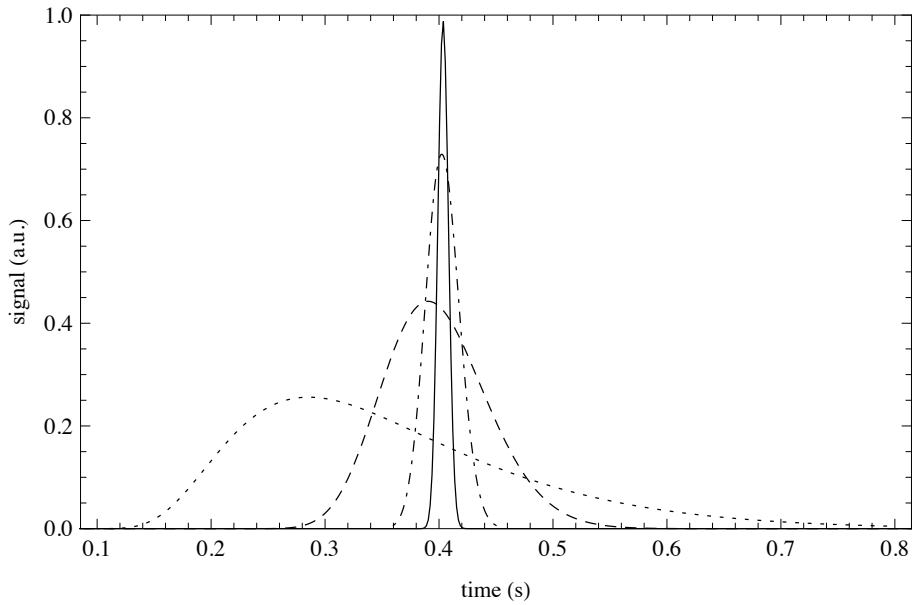

FIGURE 2.23. Calculated time-of-flight signal on the DLD (from Eq. (2.34)) for different typical temperatures of the cloud encountered during the experiment: 1 mK (dotted) during the MOT phase, 100 µK (dashed) after 1D cooling in the magnetic trap, 5 µK (dot-dashed) near the end of the evaporative cooling and 1 µK (solid) around the Bose-Einstein condensate transition. The origin of the horizontal axis is measured from the switch-off of the magnetic trap and amplitudes of the signals are scaled such that all the curves could be seen in the figure.

Bose-Einstein condensate

Analogously to the thermal Bose distribution, we can take the density distribution of a BEC given by Eq. (2.15) and insert it to Eq. (2.30) , which yields

$$\phi_{BEC}(t) = \frac{15N_c}{8\pi r_x r_y r_z}\left(\frac{1}{2}gt + \frac{h}{t}\right) \times \int_{m_y-m_r}^{m_y+m_r}\int_{m_x-m_c}^{m_x-m_c} \max\left(0, 1 - \left(\frac{x}{r_x}\right)^2 - \left(\frac{y}{r_y}\right)^2 - \left(\frac{(-h+1/2gt^2)}{r_z}\right)^2\right) \mathrm{d}x\,\mathrm{d}y, \tag{2.35}$$

hence

$$\phi_{BEC}(t) = \frac{15N_c}{16r_x}\left(\frac{1}{2}gt + \frac{h}{t}\right) \mathrm{Re}\left\{\left[1 - \frac{(-h+\frac{1}{2}gt^2)^2}{r_z^2}\right]^2\right\}. \tag{2.36}$$

Equation (2.36) is used to fit the condensed clouds with N_c and μ as free parameters. When partially condensed clouds are detected, we use a sum of Eqs. (2.33) and (2.36) as a fit function.

2.6. Magneto-optical trap

To create an ultracold sample of atoms one needs to trap the atoms and employ the much successful laser cooling techniques. In particular, the magneto-optical trap (MOT) has been a workhorse of almost all cold atom experiments.

We capture the slowed atoms in a MOT, whose centre is located 20.5 cm behind the Zeeman slower exit in an experimental chamber (see Fig. 2.31). For the MOT, we superimpose a magnetic field with a three pairs of counter-propagating laser beams that are mutually perpendicular to each other (cf. Fig. 2.24). Two of them are positioned at an angle of 45° with respect to the slower axis, such that they do not interfere with the slowing process [101]. The beams intersect at the centre of a pair of coils with opposite currents and are circularly polarised such that they induce σ^+ or σ^- transitions depending on the quantisation axis.

The quadrupole magnetic field for the MOT is generated by running 52 A through two coils positioned 12 cm apart. The coils (the outer radial, OR, coils) are part of the "cloverleaf" magnetic trap assembly (Fig. 2.28). The magnetic field gradient at the trap centre is 20 G/cm in radial and 10 G/cm in axial direction with respect to the symmetry axis of the magnetic trap. Additionally, three pairs of round offset coils are placed around the chamber to generate a homogenous magnetic field in the centre of the trap. This allows for positioning of the MOT such that its centre overlaps with the centre of the magnetic trap. Each coil was designed such that the current of 1 A would generate a magnetic field of 0.5 G in the trap centre.

A MOT for metastable helium is very peculiar as compared to the typical MOT of alkali atoms. First of all, because of the simple level structure of He*, it suffices to use only one laser frequency. Secondly, a two-body loss rate—due to Penning ionisation (PI) [51]—is a few magnitudes higher than in other species, leading to a short lifetime of the trapped cloud.

Penning ionisation (PI) is a collisional process that deexcites the metastable helium atom back to its ground state and ionises its collision partner [51]. It can also occur between two He* atoms, in which case both atoms are lost from the trap

$$\mathrm{He}(2^3\mathrm{S}_1) + \mathrm{He}(2^3\mathrm{S}_1) \rightarrow \begin{cases} \mathrm{He}(1^1\mathrm{S}_0) + \mathrm{He}^+ + e^- \\ \mathrm{He}_2^+ + e^- \end{cases} \tag{2.37}$$

For many years it was believed that loss rates due to PI would prevent formation of a He* BEC. Yet as it has been shown by Shlyapnikov et al. [102] that in a spin-polarised helium sample, due to spin conservation, the PI occurs at a rate 5 orders of magnitude slower than in the unpolarised case. On the other hand, this process can be used as a diagnostic tool to monitor the evolution of the atomic cloud in real time, while keeping the atoms trapped [31, 103, 104].

Thus, in order to achieve a significant number of atoms in the MOT we have to have a high loading rate, but more importantly we also have to minimise PI losses. While the former is true for every element that one wants to trap, the latter sets a very stringent requirement on the experimental apparatus. The loading rate can only be maximised by optimising incoming flux of trappable atoms and the application of large MOT beams

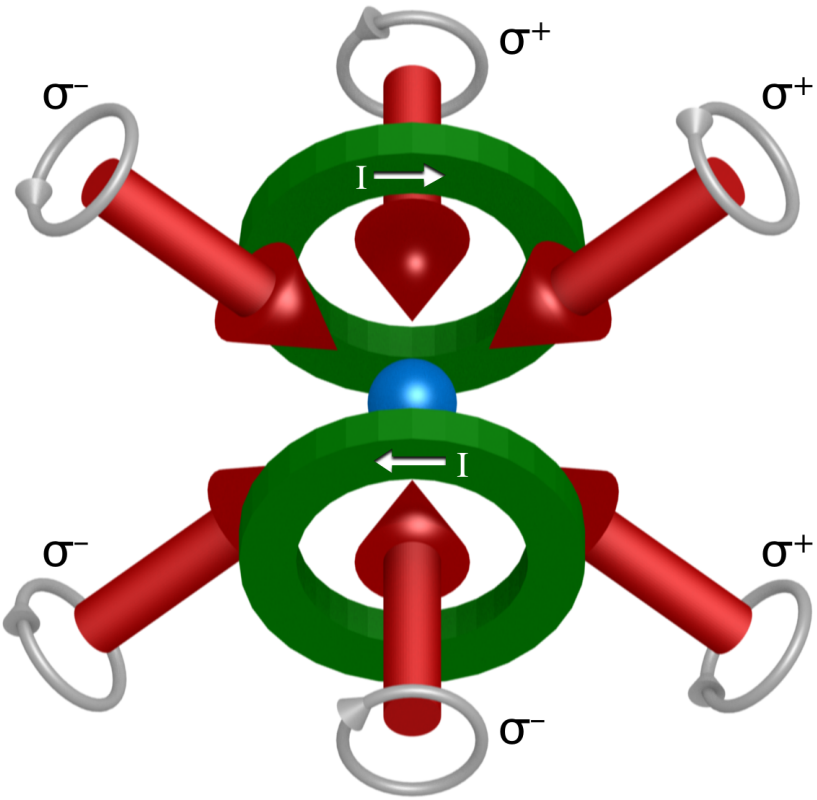

FIGURE 2.24. Trap configuration for the MOT. It is formed by three orthogonal pairs of laser beams (red) with requisite polarisation. Outer radial OR coils (green tori) from the cloverleaf coil assembly (see Fig. 2.28), are positioned 12 cm apart. They generate a quadrupole magnetic field. The arrows indicate the current direction in each coil, and the grey arrows the circular polarisation of the laser light.

to achieve a large capture region. The minimisation of PI losses is done by keeping the density as low as possible. The low density requirement entails creation of a MOT cloud of a considerable size and hence using a large detuning[30]. In order to capture a sufficient number of atoms in the trap we have to compensate for the detuning with higher laser power. The diameter of the MOT beams is 3.6 cm, and intensity is $30\,I_s$ per beam. The light is red-detuned by $-26.5\,\Gamma$ (-43 MHz) from the atomic resonance. The high intensity and detuning increase the capture velocity of the MOT and keep the density of the atomic cloud low, which is necessary to minimise losses resulting from PI.

[30]Early helium experiments used a "standard" detuning and their atom numbers were limited to 10^6 atoms [105–107].

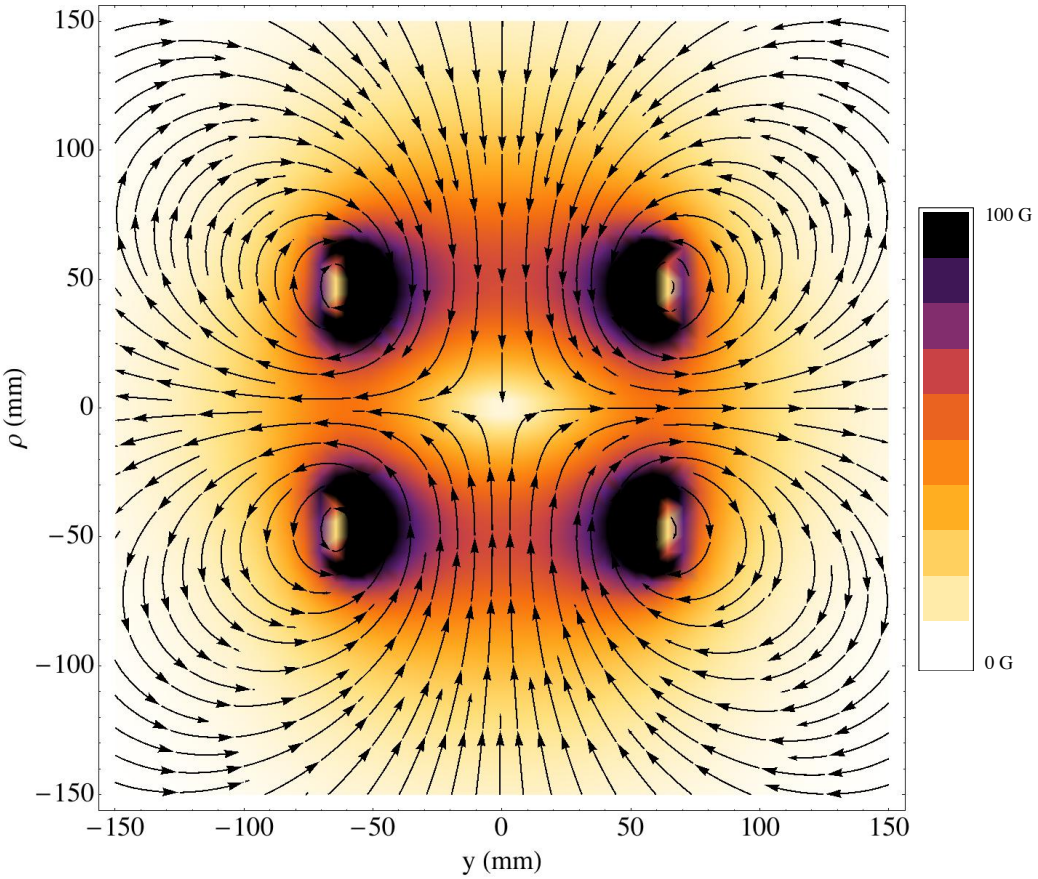

FIGURE 2.25. Field lines showing the direction of the MOT magnetic field in the yz plane. Shading indicates the absolute field.

TABLE 2.4. MOT typical experimental details and results.

Experimental details	Laser detuning	$-43\,\mathrm{MHz}$
	$1/e^2$ beam diameter	$5\,\mathrm{cm}$
	Beam intensity	$2\,\mathrm{mW\,cm^{-2}}$
	Magnetic field gradient $\frac{\partial B}{\partial y} = 2\frac{\partial B}{\partial \rho}$	$18.5\,\mathrm{G\,cm^{-1}}$
Typical results	Temperature, T (mK)	0.73(4)
	Number of atoms, N	$6.2(1) \times 10^8$
	Radial radius, σ_{rad} (mm)	2.5(1)
	Axial radius, σ_{ax} (mm)	2.2(3)
	Volume, V (mm^3)	216(12)
	Central density n_0 (cm^{-3})	$2.20(3) \times 10^9$
	Decay rate βn_0 (s^{-1})	12.3

We are monitoring the trapped cloud using fluorescence on a standard camera (Sony DV1910), despite its low sensitivity at 1083 nm. From the intensity profile the number of atoms in the MOT can be roughly estimated.

For an accurate characterisation of the atomic cloud we use a number of techniques (see Sec. 2.5). Typically we use absorption imaging to determine the number of atoms, whereas we use the MCP, positioned below the trap, to determine the velocity distribution[31]. This can be cross-checked with a measurement of the ballistic expansion of the MOT using absorption imaging with which we can additionally measure temperature in the axial direction. After switching off the trap we switch on the probe beam after different delays. From the ballistic expansion one gets cloud sizes at different expansion times from which we can infer the rms velocity and thus temperature. Assuming a Gaussian density profile and a Maxwell-Boltzmann velocity distribution in the MOT, the density profile remains Gaussian during expansion and the evolution of the radial σ_ρ and axial σ_y rms radii is given by

$$\sigma^2_{\rho,y}(t) = \sigma^2_{\rho,y}(0) + \bar{v}^2_{\rho,y} t^2, \tag{2.38}$$

where $\bar{v}^2_{\rho,y} = k_B T_{\rho,y}/m$ denotes the mean square velocity distribution and $T_{\rho,y}$ the temperature in radial and axial directions, respectively. With the number of atoms N and the trapping volume $V = (2\pi)^{3/2}\sigma^2_\rho \sigma_y$ the central density $n_0 = N/V$ can be calculated. We observe $6.2(1) \times 10^8$ atoms at a mean temperature of 0.73(4) mK with a difference of 0.1 mK between radial and axial directions. This leads to a density of $n_0 = 2.20(3) \times 10^9\,\mathrm{cm}^{-3}$ which is approximately 100 times lower than the typical densities achieved in an alkali-atom MOT. Lower temperature can be achieved at the expense of the lower number of atoms and vice versa by tuning the driving frequency and the efficiency of the diffraction of the double-pass AOM that is responsible for the MOT laser beams. Notwithstanding, we optimise the system for the highest number of atoms in the magnetic trap.

We stop the loading of the MOT by switching off the Zeeman slower (the light as well as the second section of the coil) and shutting off the atomic beam with the beam-line shutter. From the fluorescence signal, or from the flux of incoming atoms on the MCP detector, we can estimate the lifetime of the cloud and the loss rates. For a Gaussian density profile the loss rate of the atoms is given with the phenomenological formula [105]

$$\frac{dn(t)}{dt} = -\alpha n(t) - \frac{\beta}{2\sqrt{2}} n^2(t), \tag{2.39}$$

where $n(\mathbf{r}, t)$ is the atomic density, α is the decay constant due to the collisions between the trapped atoms and the background gas, and β is the two-body loss rate stemming from the collisions between trapped atoms. The flux at the MCP detector can be written as [105]

$$\phi(t) = \int \left(\epsilon_a \alpha n(t) + \frac{\epsilon_b \beta}{4\sqrt{2}} n^2(t) \right) d^3\mathbf{r}, \tag{2.40}$$

where ϵ_a and ϵ_b are the efficiencies with which ions are produced and detected respectively. At low enough pressures (which is the case in our case, as we operate MOT at

[31] Due to the asymmetry of the trap, MCP detector gives only the velocity distribution in radial direction.

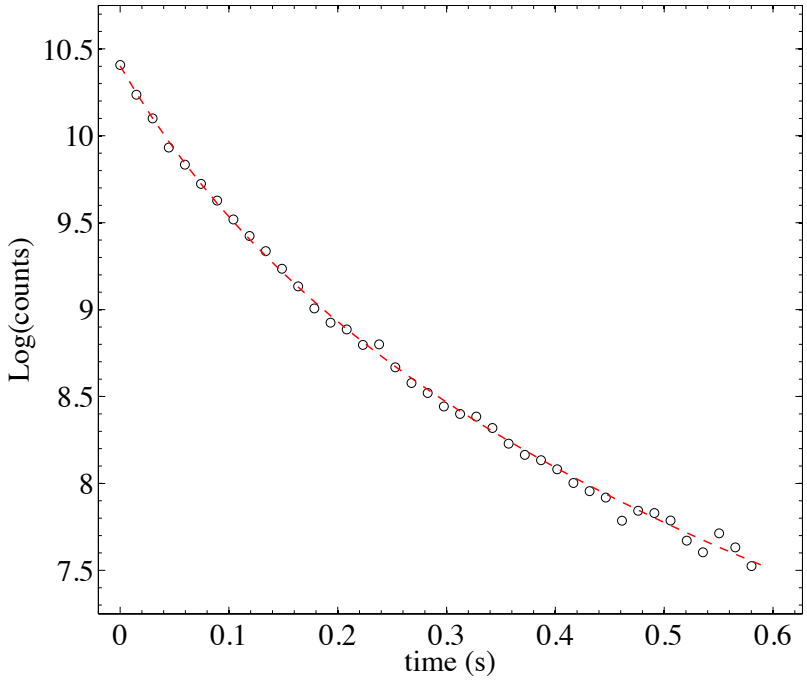

FIGURE 2.26. A non-exponential decay of the number of atoms from the MOT falling on the MCP detector. The origin of the horizontal axis, $t = 0$, is set as the moment when loading of the atoms to the MOT is stopped. We do this by switching off the Zeeman slower and blocking the direct line of sight to the source by closing the beam-line shutter. The vertical axis is linear and represents an integrated total number of counts from which the natural logarithm is taken. The curve is fitted according to Eq. (2.41), from which we get a decay rate of $\beta n_0 = 12.3\,\mathrm{s}^{-1}$.

$\sim 3 \times 10^{-10}\,\mathrm{mbar}$), due to sufficient density, β is so high that it is possible to neglect α. Solving Eq. (2.39) for $n(t)$ and integrating Eq. (2.40) leads to

$$\phi(t) = \sqrt{2}\epsilon_b V \frac{\beta n_0^2}{(2\sqrt{2} + \beta n_0 t)^2} + B, \tag{2.41}$$

where $n_0 \equiv n(t = 0)$ is the central density at $t = 0$, V is the trapping volume and B is the background signal. Knowing the central density n_0 from absorption imaging one can deduce β from the MCP signal. The loss rate β is of course dependent on laser detuning and intensity. An example of such a non-exponential decay together with a fitted curve from Eq. (2.41) is shown in Fig. 2.26. Data were taken for $\Delta = -43\,\mathrm{MHz}$ detuning and show perfect agreement with the model. The loss rate coefficient is $\beta = 5.6(8) \times 10^{-9}\,\mathrm{cm}^3\,\mathrm{s}^{-1}$, which is comparable to other helium experiments that measured loss rates in a 1083 nm

MOT [108–111]. The decay rate is then $\beta n_0 = 12.3\,\mathrm{s}^{-1}$ with a lifetime[32] of the MOT cloud of 180 ms.

Even though our loss rate coefficient is few orders of magnitude higher than for alkali atoms (e.g. for Rb $\beta_{Rb} \approx 10^{-12}$ [112]), we achieve comparable number of atoms compared to the MOTs of alkali-metals. This promises a good perspective for magnetic trapping and further cooling.

2.7. Magnetic trap

The temperatures that can be achieved in MOT are limited by the spontaneous emission. Furthermore, the atomic density is limited by losses associated with Penning ionisation. Further cooling can be realised in a magnetic trap where only low-field seeking atoms can be trapped, i.e. in case of ^{4}He only those in magnetic sublevel $m = +1$. Due to the spin conservation the losses are suppressed [113].

The simplest magnetic trap is created by the quadrupole field of the MOT. However, this configuration has a zero-field minimum which for an atom moving through the centre of the trap results in the field changing too fast, leading to severe losses by so-called Majorana spin flips [114, 115]. As the atoms at the trap minimum are mostly from the low energy tail of the Boltzmann energy distribution, the colder the sample is, the more pronounced these losses are. These losses arise when an atom is moving through a magnetic field that is changing magnitude or direction and the magnetic moment is not following the change. Quantitatively one can express that the rate of change of the magnetic field $d\theta/dt$ should be lower than the Larmor precession frequency $\omega_L = g m_J \mu_B B/\hbar$ of the atom. It is evident that this condition is violated at a low fields (especially when the field has a zero crossing) and high magnetic field changes. In such regions the atoms are not able to adiabatically follow the field changes. This can lead to a spin flip and an atom is ejected from the trap [116]. Therefore, it is necessary to have a trap with a nonzero field minimum with low magnetic field gradients where these spin flips are strongly suppressed.

An example of such a trap is the Ioffe-Pritchard trap that consists usually of two pairs of circular coils and four straight bars [117, 118] and produces a harmonic potential in the trap centre. This trap, though, requires a special vacuum design, as all current carriers need to be as close as possible to the atoms to provide maximum confinement. Its variation is a "cloverleaf" trap (shown in Fig. 2.28) where the bars are replaced by eight small coils [119]. This configuration allows for a more flexible design of the vacuum apparatus and provides more optical access.

2.7.1. Trapping field

The magnetic trap is the most critical piece of equipment in the apparatus, therefore we spent a great deal of time designing our magnetic trap. The magnetic field of a Ioffe-Pritchard quadrupole trap, expressed in cylindrical coordinates, is approximated near the

[32] Due to the non-exponential decay we define lifetime as time after which $1/e$ of the atoms are left in the trap.

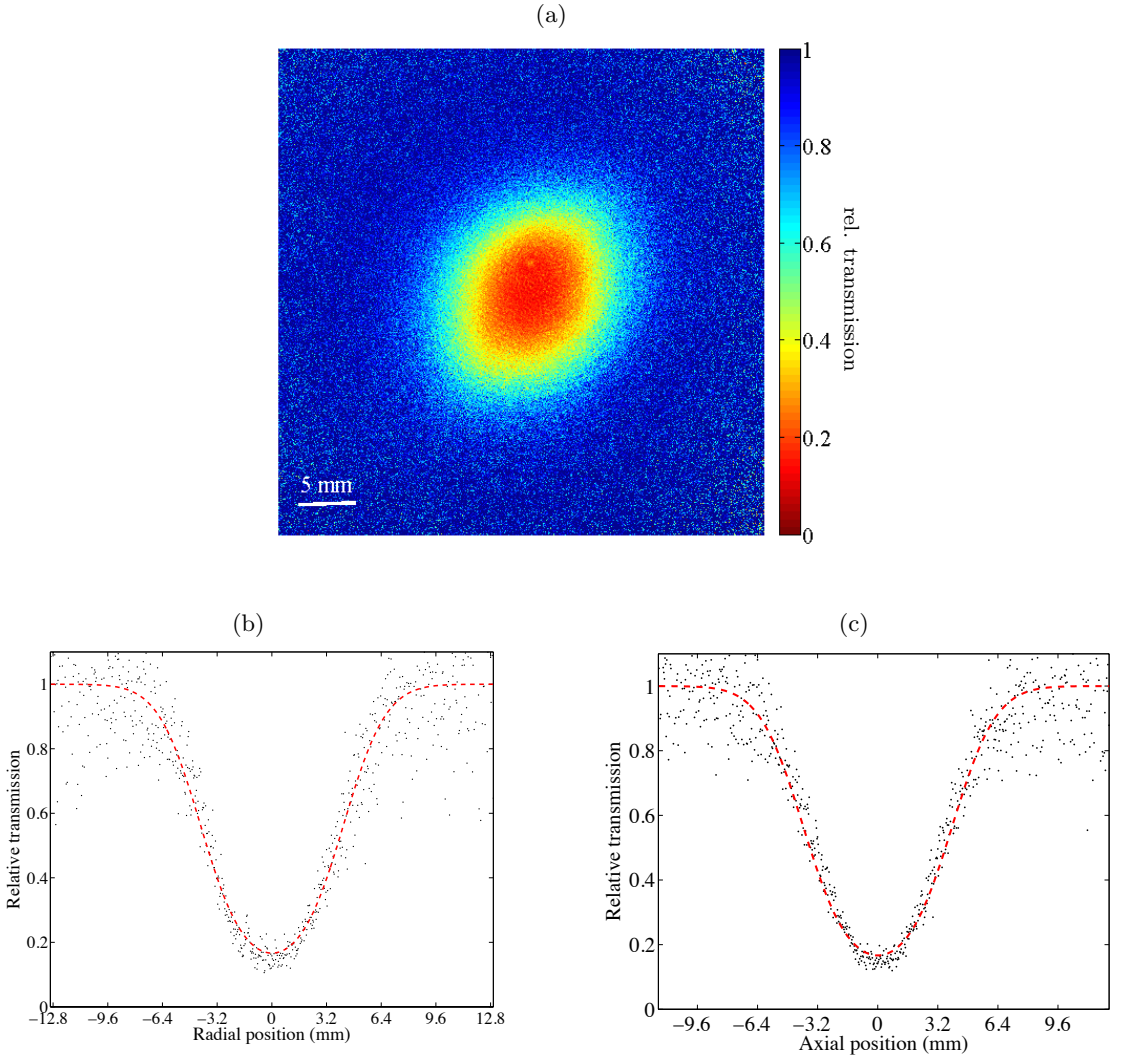

FIGURE 2.27. (a) An absorption image of the MOT cloud with 6×10^8 atoms, 1.5 ms after the trap has been switched off. (b) and (c): Cross sections through the cloud centre in the radial and axial direction respectively. The dashed curves are fits of the thermal distribution given by Eq. (2.14).

origin by [120]

$$\begin{aligned} B_\rho &= \alpha\rho\sin 2\phi - \beta z\rho, \\ B_\phi &= \alpha\rho\cos 2\phi, \\ B_z &= B_0 + \beta z^2 - \frac{1}{2}\beta\rho^2, \end{aligned} \tag{2.42}$$

where α is the radial gradient, β is the axial curvature and B_0 the magnitude of the field in the centre. Terms that contain α are components of the quadrupole field, produced by straight current segments (or cloverleaf coils), while other terms represent components of the dipolar field, produced by axial (pinch and compensation) coils. Alternatively, the magnetic field can be calculated by numerical calculation of a Biot-Savart integral, which gives the same result for the field magnitudes as well as regions that we are interested in.

The absolute field of a Ioffe-Pritchard quadrupole trap, with field vector components from Eq. (2.42), is given by

$$|\mathbf{B}| = \sqrt{(\alpha^2 - B_0\beta)\rho^2 + (B_0 + \beta z^2)^2 - 2\alpha\beta z\rho^2\sin 2\phi + \frac{1}{4}\beta^2\rho^4}. \tag{2.43}$$

The field is linear, except for the trap centre where it gradually becomes harmonic. For practical purposes, the second-order expansion of Eq. (2.43) around the trap centre is sufficient to describe the field at the trap centre,

$$B \approx B_0 + \beta z^2 + \frac{1}{2}(\alpha^2/B_0 - \beta)\rho^2, \tag{2.44}$$

but it is valid only when $(|\mathbf{B}| - B_0)/B_0 \ll 1$. Ultracold atomic clouds are trapped in this harmonic region.

The potential energy of an atom in an external magnetic field is given by

$$U(x) = -\boldsymbol{\mu}\cdot\mathbf{B}(x), \tag{2.45}$$

where $|\boldsymbol{\mu}| = -gm_J\mu_B$ is the magnetic moment, with Landé factor $g = 2.0023$ (in case of 2^3S_1 state in ^{4}He), magnetic quantum number m_J and Bohr magneton μ_B. Then for atoms trapped in $m_J = +1$ state, we can write

$$U = 2\mu_B B \approx 2\mu_B B_0 + \frac{1}{2}m(\omega_z^2 z^2 + \omega_\rho^2\rho^2) \tag{2.46}$$

with trap frequencies given by

$$\begin{aligned} \omega_\rho &= \sqrt{\frac{2\mu_B}{m}\left(\frac{\alpha^2}{B_0} - \beta\right)}, \\ \omega_z &= \sqrt{\frac{4\mu_B\beta}{m}}. \end{aligned} \tag{2.47}$$

The trap depth is determined by the lowest field barrier[33], the location and height of which has to be found using exact expressions for the magnetic field. Using the Radia

[33]Unless there is a geometrical constraint of the setup, i.e. the walls of the glass cell or a re-entrant flange.

package[34] for Mathematica we have simulated fields of the magnetic trap. It creates a real-size coil assembly, then using a finite elements method calculates the field by numerically solving the Biot-Savart integral. Figure 2.30 shows the absolute field in xy plane.

The absolute field before and after compression along the cross sections through the centre of the trap is shown in Fig. 2.29. Initially the magnetic trap has parameters $B_0 = 18\,\mathrm{G}$, $\alpha = 34.8\,\mathrm{G\,cm^{-1}}$ and $\beta = 8.6\,\mathrm{G/cm^2}$. After compression the radial gradient increases to $65\,\mathrm{G\,cm^{-1}}$, axial curvature is increased to $9.6\,\mathrm{G\,cm^{-2}}$ and a bias field is lowered to 2 G. As can be seen in Fig. 2.30 the field has four saddle points: two higher ones in the radial direction (as seen in Fig. 2.29a) and two lower ones positioned at $(20\,\mathrm{mm}, \pm 13.8\,\mathrm{mm})$ with respect to the trap centre where atoms with enough kinetic energy can leave the trap. The trap depth is then given by the height difference between the lower saddle points and the trap bottom. In the uncompressed trap it equals 28.2 G, which corresponds to the temperature of 3.8 mK, and after compression it increases to 7.2 mK. The position of the saddle points changes in the compressed trap to $(22\,\mathrm{mm}, \pm 9\,\mathrm{mm})$ with respect to the trap centre. The axial curvature and radial gradient are adjusted independently by changing the current in both sets of radial coils and cloverleaf coils, respectively. The bias field is the sum of fields of two sets of radial coils that produce almost equal and opposite fields in the trap centre. Moreover, the radial frequency depends on the bias field B_0, thus the trap can be compressed not only by increasing the current in the cloverleaf coils but also by lowering the trap bottom.

2.7.2. Trap design

Our cloverleaf trap consists of two sets of six coils each. Each set of coils contains four race-track shaped cloverleaf coils (IR), that are responsible for radial confinement, which are placed as close to the atoms as possible (see Fig. 2.28) as well as inner (IR) and outer radial (OR) coils that influence both axial and radial magnetic fields. Using our computer simulation we optimised the shape and the winding pattern of our coils such that we maximised both the magnetic field gradients as well as curvatures. However, we had to take into account a few geometrical and technical constraints. The geometrical limitations are given by the size of our vacuum chamber, whereas the technical ones are given by the power dissipation, availability of the commercial power supplies and copper tubing. The dimensions of the coils are limited by the size of the re-entrant flange: from one side, the outer diameter of the assembly cannot be larger than the inner diameter of the flange (153 mm), as this affects the size of the OR as well as the IR coils; on the other side, the inner diameter is limited by the diameter of the knife edge on the window flange (50 mm). As the window is not bonded to the vacuum chamber, its flange protrudes by a few centimetres out of the assembly for mounting convenience[35] (see Fig. 2.31). The coils are wound out of a square copper tube ($4\,\mathrm{mm} \times 4\,\mathrm{mm}$ with $2\,\mathrm{mm} \times 2\,\mathrm{mm}$ bore) that

[34] Radia is a Mathematica package developed by the European Synchrotron Radiation Facility (ESRF) and can be used in different branches of physics, where efficient solutions of 3D boundary problems of magnetostatics are needed.

[35] This configuration does not constrain the trap depth. However, it geometrically limits the optical access to a very narrow angle.

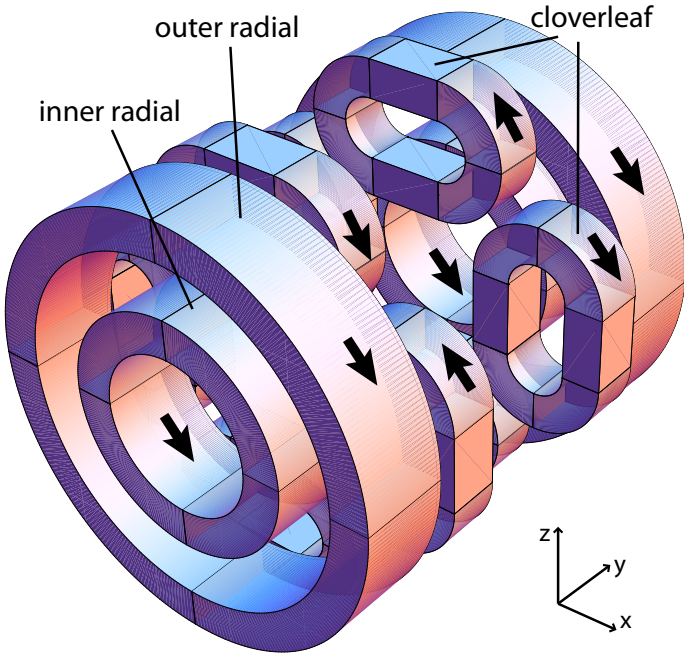

FIGURE 2.28. Schematic arrangement of our "cloverleaf" magnetic trap. It consists of a pair of outer radial coils (OR), a pair of inner radial coils (IR) and four pairs of race-track shaped "cloverleaf" coils (IR). The MOT quadrupole field is created by the current flowing in opposite directions in the OR coils, whereas in the magnetic trap OR and IR coils are mainly responsible for the trap bias field and the axial confinement, and the IR coils create the radial confinement. The coils are wound out of square, water-cooled, copper tubing. Each coil consists of 3 layers each containing 6 windings of copper tubing, except for IR coils that have 3 windings in each layer. The arrows indicate current directions in the magnetic trap.

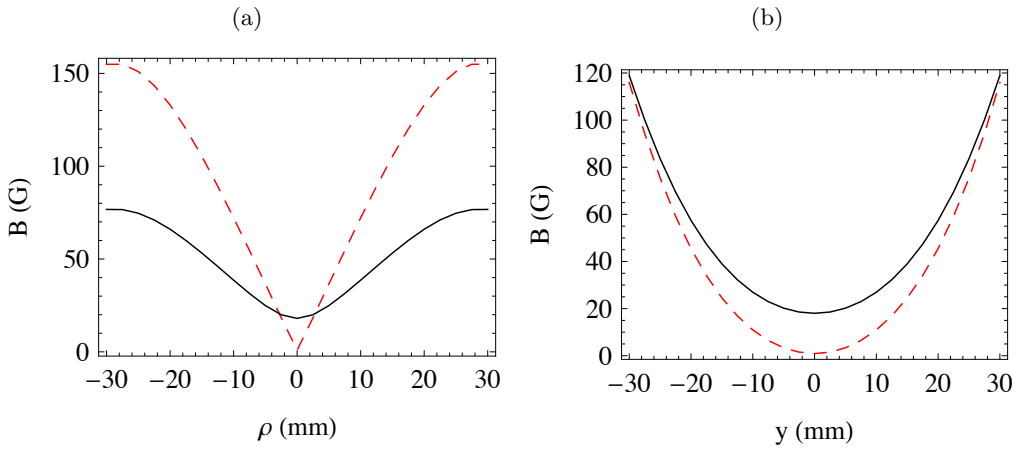

FIGURE 2.29. Cross sections of the simulated absolute magnetic field before (solid curve) and after (dashed curve) compression along the (a) radial and (b) axial directions in the trap centre.

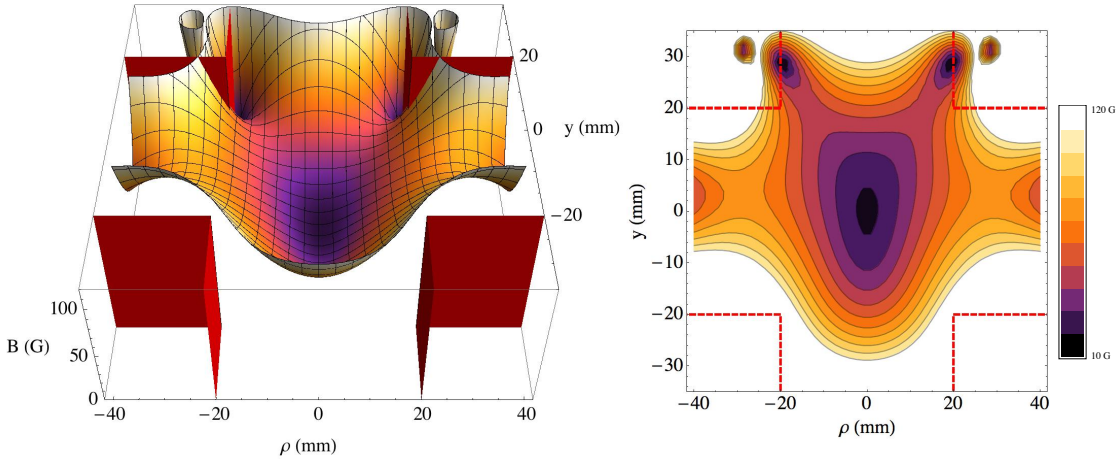

FIGURE 2.30. Calculated absolute field of the magnetic trap before compression in the xy plane. For clarity the two-dimensional plot on the right-hand side is the top view of the 3D plot on the left-hand side. On the left-hand side the vertical walls (dashed lines in the figure on the right-hand side) mark the positions of the re-entrant flanges where the coils are positioned.

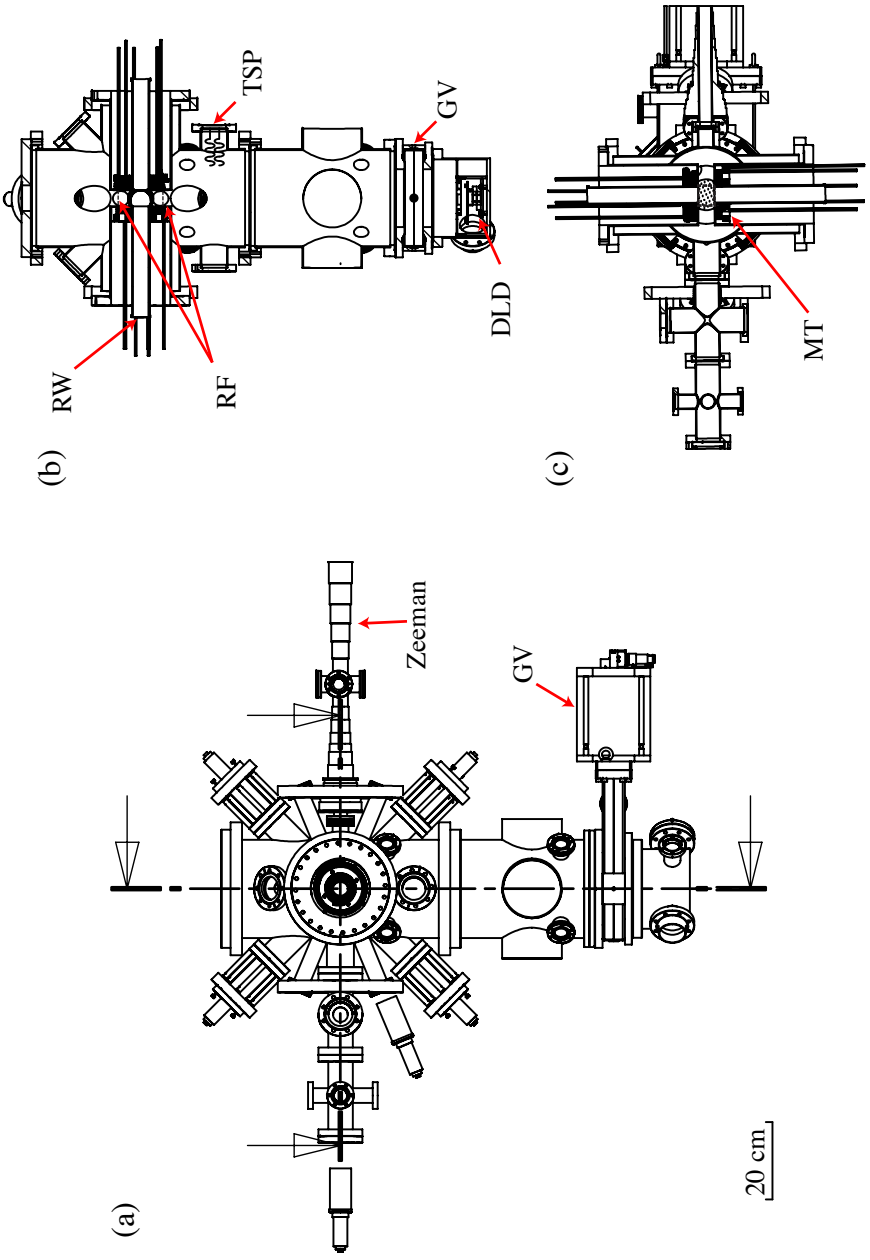

FIGURE 2.31. (a) Side view of the science vacuum chamber. Dashed lines together with arrows indicate the planes of the cross sections shown in (b) and (c). (b) Cross section of the back view of the science chamber. (c) Cross section of the top view of the science chamber. For clarity, only a few components are labelled, that is the Zeeman slower, the gate valve (GV), filaments of the titanium sublimation pump (TSP), the magnetic trap (MT), the radio-frequency coils (dashed, RF) and the viewport in the re-entrant flange above its surface. All dimensions are to scale.

is taped with 50 µm-thick Kapton tape which provides very good electric isolation at a minimal thickness. Each coil consists of three layers, each containing six windings of copper tubing, except for IR coils that have three windings in each layer. This ensures the achievement of low inductivity which is needed for fast switching. Each set of coils is glued (J-B Weld epoxy) onto a Teflon holder that for mechanical stability is held by three Tr8 trapezium-threaded screws. The whole assembly tightly fills a re-entrant flange, that allows placement of the coils as close as possible to the atomic cloud, and it is fixed to the vacuum chamber with M8 bolts. The distance between the two sets of coils is 50 mm.

The materials for the magnetic trap were carefully chosen to withstand the bakeout temperature of 200 °C. The coil setup is connected to a cooling circuit with a cooling power of 15 kW at a temperature of approximately 19 °C. A typical flow of around 1 l/s at 6 bar pressure is maintained. Each coil is cooled separately. The cooling fluid is a mixture in a ratio of 100:1 of tap water and a corrosion inhibiting fluid WIN-L-2320 from Wasser- und Industrietechnik GmbH. The temperature of the coils increases during operation by a few degrees, which causes thermal expansion of the materials used in the MT, its holder and the vacuum chamber. Our simulation predicts change of the trap bottom by a few MHz, though, we observe a shift of the trap bottom which is only a fraction of this value.

2.7.3. Current switching

The diagram showing connection of the coils and switches is shown in Fig. 2.32. The current is supplied by three Delta Elektronika (SM15-100, SM30-200, and SM15-400) power supplies. The current through the OR coils is supplied by the SM30-200 (PS2). The SM15-100 (PS1) adds current to the IR coils. The SM15-400 (PS3) is used exclusively to supply the current for the CL coils as they need the highest current for the radial confinement. As switches we use insulated gate bipolar transistors (IGBTs, Mitsubishi PM600DV1A060) that are driven by Powerex BP2A drivers. The current is delivered to the coils in the magnetic trap within 1 ms (see Sec. 3.2.1) and takes another 5 ms to settle. Quick switch-on behaviour of the coils is essential as the cloud released from the MOT should not be allowed to expand too much. Otherwise after switching on the magnetic trap, the atoms would end up in a region where the atoms would experience a high magnetic field, which translates to an increased potential energy, thus leading to heating of the cloud. Additionally, a quick switch-off of the currents is not only important for the transfer of the cloud from the MOT to the magnetic trap, but also for absorption imaging. The trap switch-off is performed on a µs timescale, yet due to eddy currents in the coils and in the vacuum chamber the magnetic field decays much longer. Magnetic field of the MOT decays in around 1.5 ms whereas field of the magnetic trap does not significantly disturb the atoms after about 3 ms.
The current is switched as follows:

- A MOT is realised by setting PS1 to 52 A and switches S1 and S4 closed. As the programming of the power supplies takes a few ms, we program PS2 and PS3 during MOT phase to 96.6 A and 160 A, respectively.

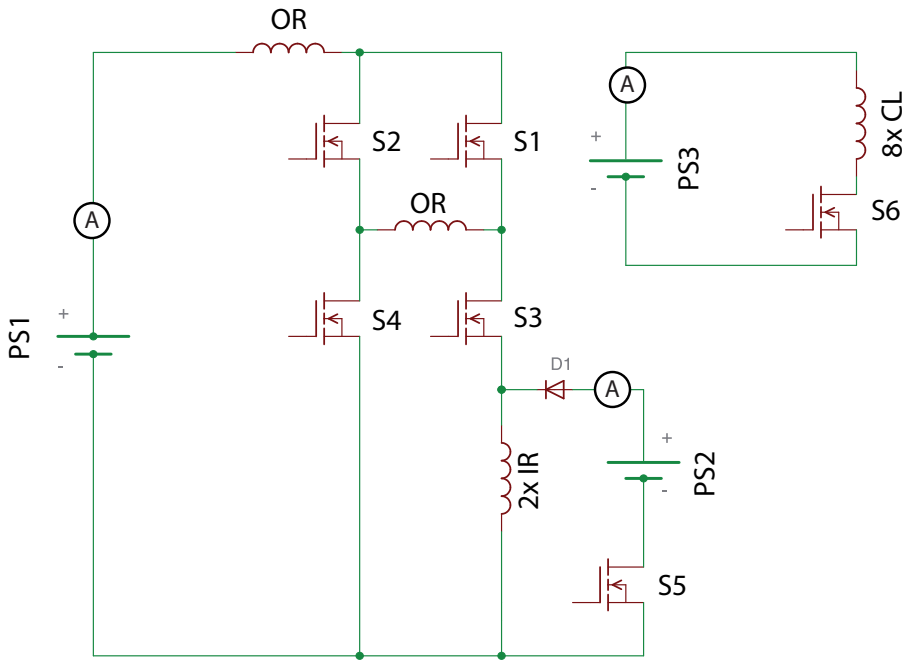

FIGURE 2.32. Schematics of the circuitry of the magnetic trap. The two inner radial IR coils as well as eight cloverleaf IR coils are connected in series. One of the OR coils is placed in an H-bridge configuration of the switches so that the current in the coil could be reversed. The MOT is produced by closing switches S1 and S4 while the cloverleaf trap is produced by closing switches S2, S3, S5 and S6. The current of the power supplies PS is measured by current transducers (A) right after the output and is fed back by control electronics (see Sec. 2.7.4). We achieve switching times on the order of µs, although eddy currents in the steel chamber prolong it up to 3 ms.

- In order to reverse the current in one of the OR coils we have to switch off the MOT, which is done by opening switches S1 and S4. Then we wait 0.4 ms for the induced current to decay, at the same time we set the current of PS1 to 120 A.
- The cloverleaf trap is created by opening switches S2, S3, S5 and S6. Now, the current flows in both OR coils in the same direction.
- We compress He* cloud by adiabatically ramping the current of the PS1, PS2 and PS3 to the respective values 122 A, 98 A and 320 A.

Separate electronic circuits, based on insulated-gate bipolar transistors (IGBTs), control the offset coils. The IGBTs are driven in the linear regime as this gives the flexibility to set different values during the experiment. Additionally, the current is stabilised by feeding back a voltage drop across a shunt resistor to the control circuit. Each pair of coils has its own control circuit and is designed for a maximum 10 A. The current in the offset coils is delivered by a power supply Agilent 6675A.

2.7.4. Current stabilisation

Stability of the currents in the magnetic trap coils is crucial for limiting the heating rate and thereby improving the lifetime of the atomic cloud in the magnetic trap. Also the repeatability of the magnetic field distribution when performing the same experiment multiple times is essential, especially for experiments that require good statistics. In particular, the magnitude of the magnetic field at the trap centre is very susceptible to fluctuations since it results from the subtraction of the much larger magnetic fields created by the outer radial coils and the inner radial coils. To achieve those two stability requirements, the currents are measured with the help of precise current transducers and shunt resistors with a very low susceptibility to temperature changes and ageing effects. The measured currents are then stabilised by analog PID circuits to controllable reference voltages from low-noise battery sources. The stabilised voltage lies in the range between 0 V-10 V and the remaining rms noise can be deduced by measuring the fluctuations on the error signal of the PIDs, which is around 10^{-4} V. This translates to a 1% stability of the 1 G magnetic field at the trap centre since it results from the subtraction of two fields on the order of 160 G. However, by measuring directly the trap bottom we verified that these fluctuations are on the order of 4%, which would imply that there are more systematic effects to be taken into account. Most probably the mechanical stability of the coils contributes to the observed instability of the trap bottom. These fluctuations translate to 120 kHz of frequency fluctuations of the trap bottom. In other words if we were to produce a condensate with the same number of thermal atoms we would have to change the end frequency of the radio-frequency ramp (see Sec. 2.8) by this value. With this stability we reliably achieve a BEC, though, it is not enough to control the number of atoms in the thermal fraction.

For maximum speed and lowest current ripple our power supplies are controlled via an analogue voltage control input. PS1 and PS2 can deliver current on a timescale of 2 ms whereas PS3 requires about 1 ms. Three flux gates (LEM Danfysik, IT 400-S Ultrastab) are located at the output of each power supply and they transduce the current by a factor of 10^3. They work on a zero-flux principle to compensate the flux of the current carrying flexes. Their outputs are transformed into voltage using an ultra-stable reference resistor (Vishay VCS3322Z, 5 Ω, Tolerance 0.1%), then the voltage is compared to the reference voltage coming either from a programmable digital-to-analogue converter (Wieserlabs FlexDAC) or stable batteries (it depends on the stage of the experimental cycle). This way an error signal is generated which is fed via a PID circuit back to the power supply.

As described in Sec. 2.9, directly after compressing the magnetic trap we use a TTL pulse that switches inputs in the control circuit from DAC to a battery in order to have a stable control voltage of the trap during the evaporative cooling. The battery is an ultra-low noise, isolated voltage source (Stanford SIM928).

2.8. Radio-frequency radiation source

Forced evaporative cooling requires a method to truncate the energy distribution of the trapped atoms at a variable energy ϵ_t. Ideally such that all atoms with energy $E > \epsilon_t$

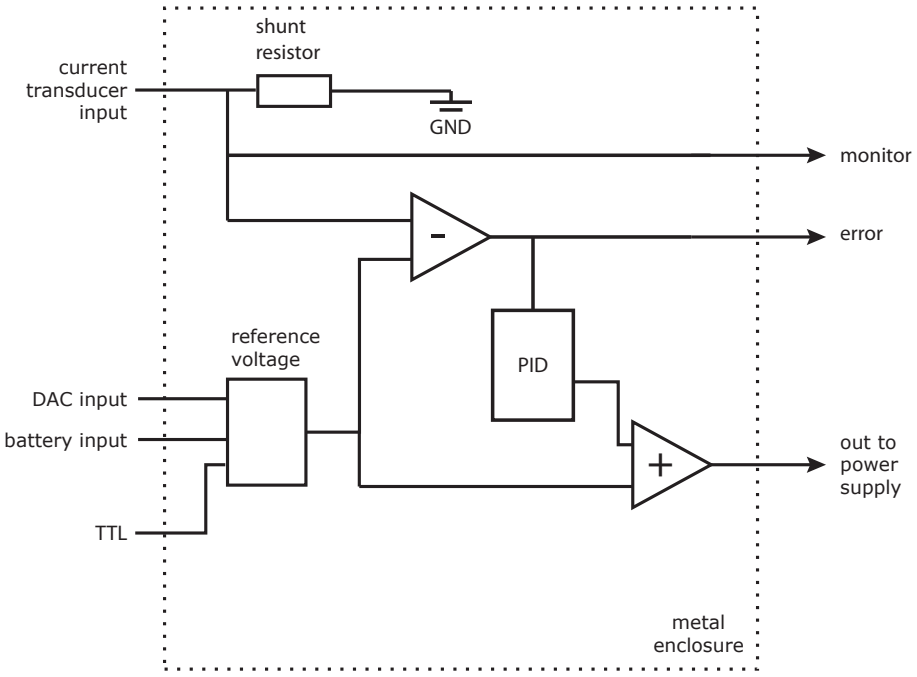

FIGURE 2.33. Schematics of the stabilisation of the magnetic trap. Current transducers sense the current delivered by each power supply, then their outputs are compared to the reference voltage coming either from a digital-to-analogue converter (DAC) that is programmed via LabView, or stable batteries. This way an error signal is generated which is then fed via a PID circuit back to the analogue voltage input of the power supplies.

are removed from the trap. By applying an rf field of linear polarisation in a direction orthogonal to the trapping magnetic field, transitions to other magnetic sub levels can be induced. Atoms traversing the surface defined by the resonance condition $\hbar\omega_{\mathrm{rf}} = 2\mu_B|\vec{B}(\rho,\phi,z)|$ are likely to undergo spin-flip transitions. When this process is efficient, the trap depth is reduced to the truncation energy $\epsilon_t = \hbar\omega_{\mathrm{rf}} - 2\mu_B B_0$.

As a radio frequency source we use a pulse/function/arbitrary noise generator (Agilent 81150A) which can be programmed to output frequency ramps with linear or exponential shapes. It is programmed via RJ45 Ethernet connection and the ramp is gated on a TTL signal from the LabView. A broadband rf amplifier (Bonn Elektronik BSA 0125-25) provides 44 dB amplification. Since its maximum input power is 0 dB the maximum available power is limited to 25 W. The amplified rf signal is coupled via an isolating SMA vacuum feedthrough to two square coils connected in series. The coils consist of five windings of insulated, vacuum compatible wire that is wound on a Teflon frame (48 mm × 50 mm). The coils are placed in between the re-entrant flanges at the distance of 120 mm, such that the laser beams are clipped as little as possible. Their exact placement is shown in Fig. 2.31. The coils have only a marginal impedance for the rf signal; thus, to reduce the back-reflection of the high power signal, it is terminated with a 50 Ω resistor. To minimise the radiation of the back-reflected signal we direct it via a directional coupler

(Mini Circuits, ZARC-26-12-S+) to the 50 Ω terminator. After the exponential ramp ends, a second rf generator (Rohde & Schwarz SMA100A) is used to generate a constant-frequency rf signal (rf knife) at the end frequency of the ramp.

In order to truncate the energy distribution of the cloud throughout the temperature range ($T \leq 1\,\mathrm{mK}$), the rf frequency has to cover the range between 150 MHz and 1 MHz. In practice, though, application of the Doppler cooling in the magnetic trap reduces the necessary frequency range to frequencies below 80 MHz.

In the experiments described in Sec. 4.4 a fraction of the condensed atoms is coupled out of the magnetic trap by means of the rf magnetic field. A separate (Agilent 33220A) Function/Arbitrary Waveform Generator is connected to the rf system, which is described above, at the input of the amplifier. This function generator is programmed to output either a predefined linear frequency sweep or a gated pulse at a fixed frequency. The start of the sweep is initiated by the TTL trigger.

2.9. Experimental control

The experiment is controlled by two expandable field-programmable gate arrays (FPGAs, National Instruments cRIO 9082) that are equipped with analogue- and digital-output modules. The former one controls in real-time each step of the experiment and the latter one serves as a supervisor, i.e. it monitors all pressures, vacuum pump statuses, electricity in the laboratory and the temperature of the cooling water. In case of any abnormality (like blackout, overheating of the coils, backing pump failure, etc.) it shuts off respective valves to maintain ultra-high vacuum. This module is also equipped with a GSM module that sends notifications via a cellular network to the relevant members of the project.

During the experimental cycle the execution and timing of the actions performed by the control FPGA is managed by an on-board clock in real-time with a time resolution (up to 55 ns) depending on cRIO module. All digital channels are externally amplified to deliver enough power to the appropriate devices. These digital output signals (TTLs) trigger different components of the setup:

(1) current switches for the magneto-optical and magnetic traps (see Sec. 2.7.3);
(2) a programmable digital-to-analogue converter (FlexDAC) which controls the current settings of the power supplies; the current stabilising circuit is told if it should take the reference voltage from LabView or from ultra-stable battery (see Sec. 2.7.4);
(3) direct digital synthesiser (DDS) that generates relevant frequencies for our AOMs;
(4) triggering of the rf generators for forced evaporative cooling, rf knife as well as rf outcoupling;
(5) triggering of the frame grabbing of the CCD camera as well as of the MCP detector;
(6) laser beam shutters to block the light in the optical fibres;
(7) beam line shutter and a gate valve to block the atomic beam after loading of the MOT and thus considerably improve vacuum.

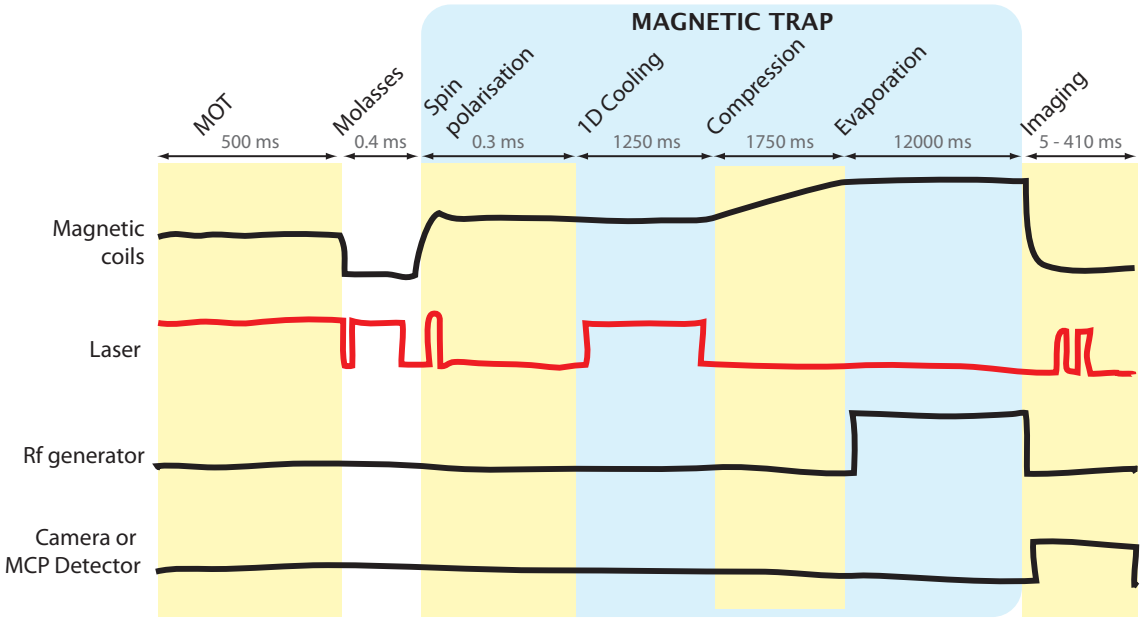

FIGURE 2.34. A simplified diagram of a sequence creating a Bose-Einstein condensate. Each column represents a step in a sequence. Steps that take place in a magnetic trap a surrounded in a light blue colour. Please note that the amplitudes of the signals are only a guide to the eye and the widths of the columns are not to scale. The duration of each step is written on top of each column.

Settings, that are used in the sequence, are sent to the devices via an Ethernet cable (i.e. radio frequency generators), RS232 connector (i.e. FlexDAC, DDS) and an analogue IO compact RIO module (i.e. power supplies, offset coils and a second stage of the Zeeman slower). Using the analogue IO module one can read out (with a maximum rate of 40 MHz) various parameters of the experiment. All these steps are programmed in a self-made, LabView-based software, whose interface serves as a GUI. A sample sequence is shown in Fig. 2.34. Settings for each experimental run (i.e. settings, variables, inputs, etc.) are saved for a convenient reconstruction of the sequence.

The data acquisition is performed on a separate IBM-class computer, so that while the data is read out (either from the camera or the DLD) the control computer can proceed to the next shot without any disruptions. The timing of the electronic shutter of the camera, necessary settings for the DLD as well as saving of the data is performed using LabView-based control software. More detailed description of the experimental control can be found in Michael Keller's PhD thesis [121].

CHAPTER 3

Magnetic trapping and cooling

In this chapter we will describe further experimental steps to achieve the Bose degeneracy. One of the crucial factors that enabled Bose-Einstein condensation of helium was suppression of Penning ionisation [113] by spin polarising the helium sample during its transfer to the magnetic trap. Then Doppler cooling of the sample is shown to be an efficient way to increase the phase-space density with almost no atom loss, lowering the temperature down to 120 µK. After a subsequent compression of the magnetic trap the cloud phase-space density is increased by five orders of magnitude using a radio-frequency-induced (rf) evaporation.

In the experimental sequence that leads to the BEC one needs to keep the atoms for an extended period of time in a magnetic trap. The most basic one, the quadrupole potential of the magnetic field in the MOT, due to Majorana-spin flips [114, 115] (see Sec. 2.7) around its zero crossing, is not suited for trapping atoms for longer times. Therefore, one has to create a potential that has a non-zero magnetic field minimum. The role of such a trap is to catch the atoms that are released from the MOT with minimal losses of atoms and phase-space density. The trapping potential should also be flexible to adiabatically compress the cloud. We have constructed a "cloverleaf" magnetic trap [117, 118], depicted in Fig. 2.28, which gives 360° optical access around the symmetry axis of the coil arrangement. The minimum of the magnetic field is located at the MOT centre. Furthermore, in order to transfer the atoms from one trap to the other one has to ensure that the atoms do not expand too much during the process. For this reason we apply a sequence of laser pulses that cool the sample further to accommodate for the lower trap depth of the magnetic trap, as well as transfer the atoms to the trapped $m = +1$ state.

3.1. Optical molasses and spin polarisation

To load the atoms into the magnetic trap, we need to reverse the current in one of the OR coils with respect to the MOT configuration. Furthermore, the temperature of the cloud has to be lowered to accommodate for the lower trap depth of the magnetic trap. We switch off the MOT current and while it is decaying we apply a 0.3 ms three-dimensional optical molasses pulse. The beams use the same telescopes as the MOT light and have a detuning of $-2.5\,\Gamma$ (-4 MHz) and an intensity of $5\,I_s$. This reduces the temperature of the cloud further to 1 mK. We thereby keep the density of the MOT cloud, at the same time reducing further the temperature of the cloud. Further cooling is avoided at this point to keep the density of the atomic cloud rather low and thereby minimise losses due to Penning ionisation.

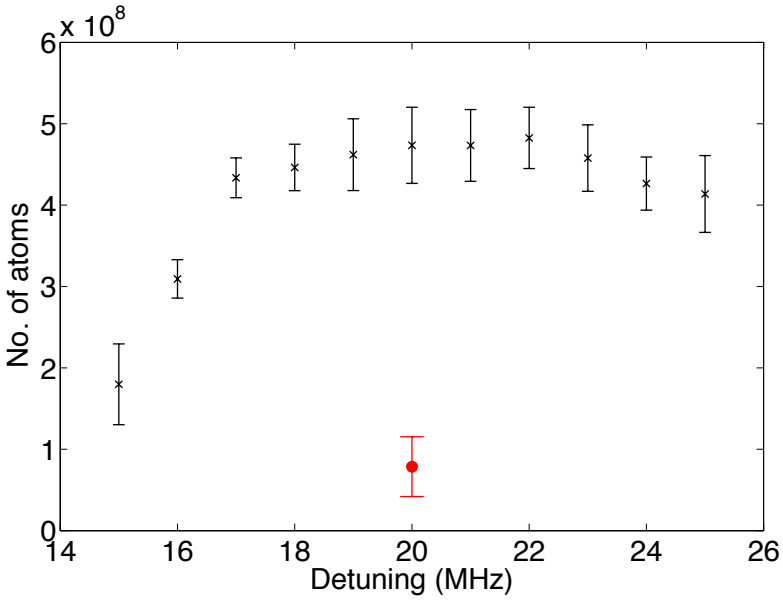

FIGURE 3.1. Measured number of atoms in the magnetic trap as a function of the detuning, Δ, of the spin-polarisation laser beams (crosses). The atom number is insensitive to the detuning over 10 MHz. One point (dot) is a run without the spin polarisation. The detuning is given with respect to the zero-field resonance. Error bars represent a standard deviation of five realisations.

Immediately after the molasses pulse, we switch on the currents of the cloverleaf magnetic trap, with its potential mode-matched to the MOT. Since the atoms in the MOT are distributed over $m = -1, 0, +1$ magnetic sublevels, we have to optically pump the atoms to the magnetically trapped $m = +1$ state. Spin polarisation not only increases the number of atoms in the magnetic trap, but also significantly reduces two-body losses due to Penning ionisation [102, 113]. Optical pumping is realised during the switch-on of the magnetic trap by two counter-propagating laser beams, aligned along the quantisation axis of the trap. These beams are σ^+ polarised to induce $\Delta m = +1$ transitions. They spin-polarise the atomic sample within 0.2 ms to the magnetic low-field seeking state. Even though the beams are blue-detuned by 32 MHz (20 Γ) with respect to the unshifted atomic transition, they become resonant during the build-up of the magnetic field. Thus, the exact detuning as well as the laser intensity ($2\,I_s$ in our case) are not crucial and can be adjusted over a broad range (as seen in Fig. 3.1). From Fig. 3.1 it is also apparent that the atoms were not evenly distributed over the magnetic sublevels, since the atom number in the magnetic trap increases almost six-fold as compared to the case with no optical pumping.

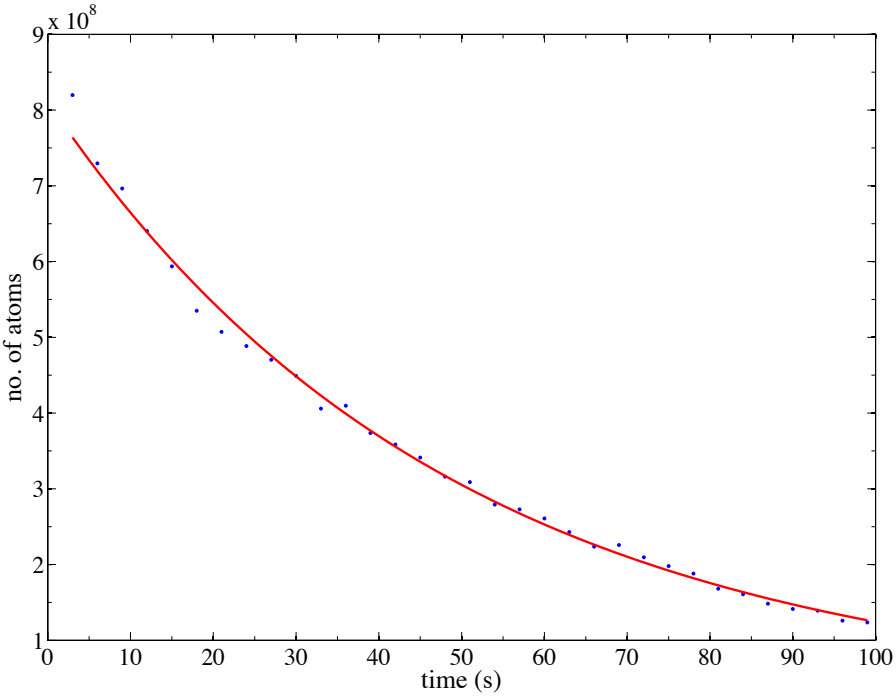

FIGURE 3.2. Number of atoms in the uncompressed magnetic trap. The fitted curve is an exponential decay and shows lifetime of the atomic cloud.

3.2. Magnetic trapping

3.2.1. Loading

Loading of the magnetic trap is a very sensitive process. Firstly, to maximise the transfer efficiency the MOT cloud centre has to overlap with the minimum of the magnetic trap field. Secondly, one cannot load the atoms immediately to the tight magnetic trap because not only would one catch barely any atoms, but also the phase space density would not increase since the cloud would be very hot. Thus, one first has to load the atoms to a "shallow" trap whose size is approximately the size of the MOT. The former is done by three pairs of offset coils, acting during the MOT phase[1] (see Sec. 2.6) and the latter is realised by lowering the currents of the power supplies.

Figure 3.3 depicts the switch-on behaviour of the currents in the magnetic trap. The currents were measured using a current probe (LeCroy CP500). The trap takes about 1 ms to have sufficient depth. This time is a compromise between bigger overshoot of the current and number of ripples in the current after switch-on. Due to the uncontrolled current oscillations the loading is non-adiabatic, which leads to heating of the cloud and the temperature increases.

At this point, the magnetic trap has trapping frequencies of $\omega_{\mathrm{rad}}/2\pi = 68\,\mathrm{Hz}$ and $\omega_{\mathrm{ax}}/2\pi = 35\,\mathrm{Hz}$ in radial and axial direction, respectively, and the bias field is 18 G. We

[1]It is much easier to manipulate a MOT cloud with external magnetic fields, since the field does not have to be extremely stable as it would have be in the case of magnetic trap.

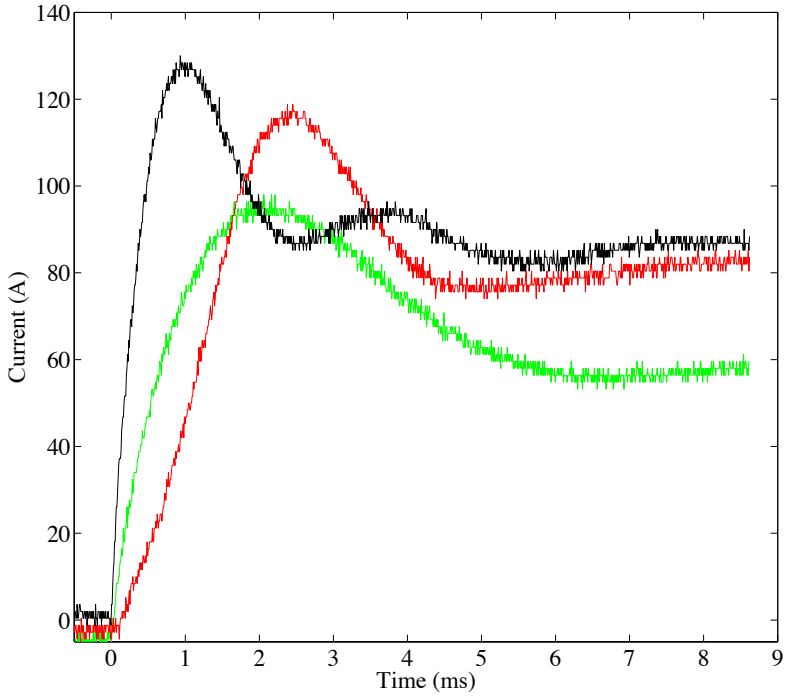

FIGURE 3.3. Magnetic trap currents during switch-on of the trap in outer radial (red), inner radial (black) and cloverleaf coils[3](green). The current has been measured using a current probe. After about 1 ms the field reaches enough depth to trap the atoms. The trapping field could be turned-on quicker but at the expense of bigger overshoot.

transfer about 90% of the initial atoms into the magnetic trap where they are in the 2^3S_1, $m_J = +1$ magnetic substate. The trap depth is around 28.2 G (3.8 mK). With the gate valve in front of the Zeeman slower closed, we achieve a lifetime of 61 s, which is limited by collisions with background gas[2].

Right after the spin polarisation pulse, we apply one-dimensional laser cooling in the magnetic trap [122, 123] for 1.2 s, which reduces the temperature of the sample to 120 µK, which is roughly three times the Doppler temperature $T_D = \hbar\Gamma/2k_B = 38.95\,\mu\text{K}$. Two counter-propagating beams are detuned by $-5\,\Gamma$ (-8 MHz) with respect to the Zeeman-shifted transition at the trap minimum. They are σ^+ polarised and have an intensity of $10^{-4}\,I_s$. The axial temperature decreases rapidly, whereas cooling in the radial direction is based on reabsorption of spontaneously emitted photons by the cloud as well as on collisional thermalisation. This increases the optical thickness of the cloud and at the

[2]To considerably increase the lifetime of the atoms in the magnetic trap we block stray light by enclosing the optical table with opaque doors.

[3]The cloverleaf current is half of the actual value as it is carried to the coils via two flexes with 50 mm^2 cross section and only one of them fits into the current probe.

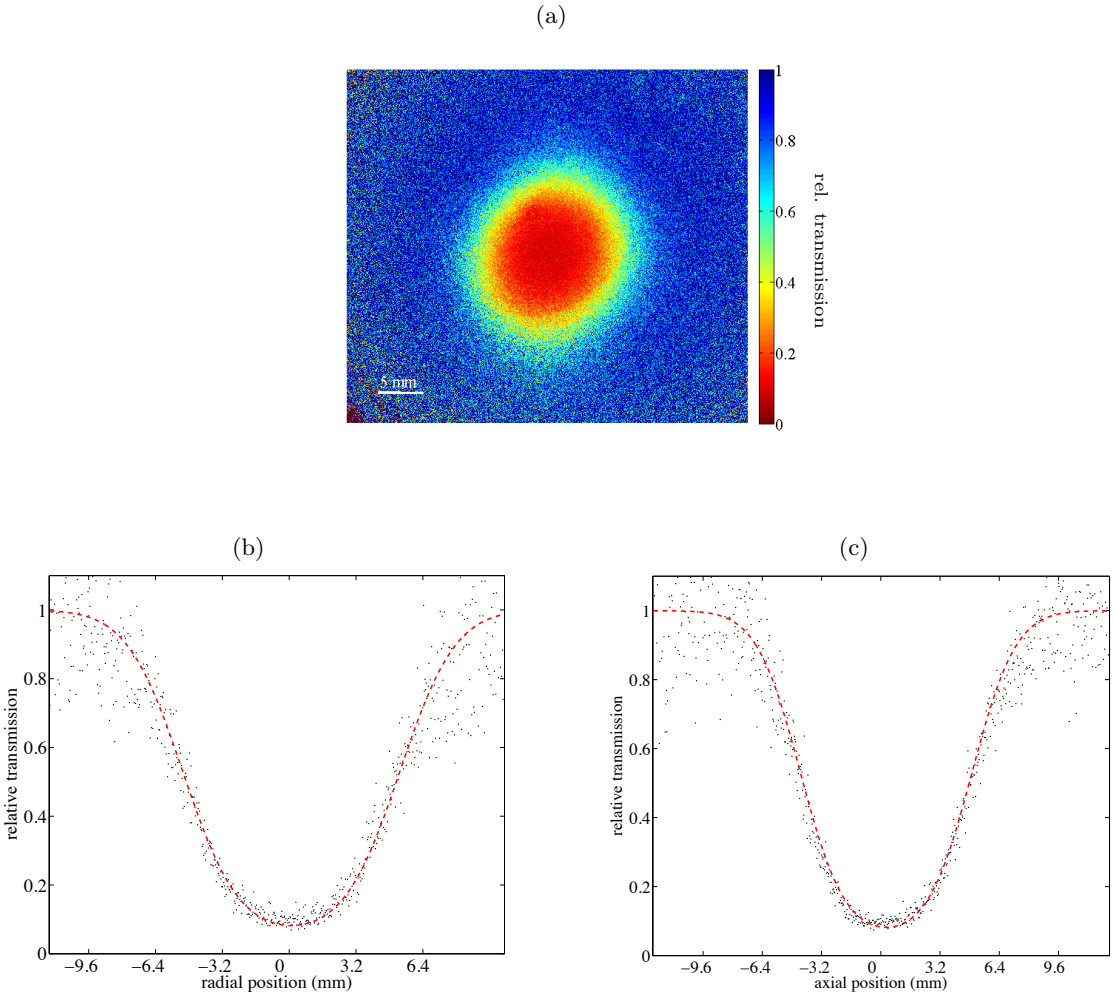

FIGURE 3.4. (a) An absorption image of the atoms in the shallow magnetic trap, after 1.2 s 1D Doppler cooling and additional 0.2 s of trapping of the cloud. The image was taken 6 ms after the trap has been switched off. The cloud has 5.8×10^8 atoms at a mean temperature 119 µK. (b) and (c) Cross sections in radial and axial direction, respectively, through the cloud centre. The dashed curve is a fit of the thermal distribution given by Eq. (2.14).

same time reduces its size. Figure 3.4 shows an exemplary image of 5.8×10^8 atoms loaded to the magnetic trap after application of the Doppler cooling and trapping for additional 0.2 s. Typically we transfer 80% of the atoms from the MOT to the magnetic trap, with around 10^9 of atoms and central density $n_0 = 3.1(2) \times 10^{10}\,\mathrm{cm}^{-3}$ after the 1D Doppler cooling.

3.2.2. Compression

Thermalisation and evaporative cooling are driven by elastic collisions. Hence, in order to be able to efficiently cool the atoms to the BEC one has to increase the elastic collision rate. We adiabatically increase the confinement of the magnetic trap until the strongest field configuration is reached. The radial gradient and axial curvature reach their maximum and at the same time the trap bottom B_0 is lowered to a minimum. In radial direction the confinement changes from harmonic to linear. Hence, under adiabatic conditions the phase-space density increases by [124, 125]

$$\frac{\Lambda_f}{\Lambda_i} = \frac{\exp\left(\frac{E_f}{Nk_BT_f}\right)}{\exp\left(\frac{E_i}{Nk_BT_i}\right)}, \tag{3.1}$$

where $E_{i,f}$ denotes the internal energy of the gas before and after compression, respectively. The phase-space density is a quantity that has to be increased during the cooling process. It is given by

$$\Lambda = n\lambda_{\mathrm{dB}}^3 \tag{3.2}$$

where λ_{dB} is the thermal de Broglie wavelength given by Eq. (A.7) and n is the density of the atomic cloud. Since the trapping potential has a finite depth ϵ_t, the energy distribution of the atoms is truncated, and one can express phase-space density as $\Lambda = N/\zeta$, with number of atoms N and a single-particle partition function ζ given by Eq. (A.8).

In order to increase the elastic collision rate, we increase the density of the atoms by adiabatic compression of the trap to $\omega_{\mathrm{rad}}/2\pi = 800(13)$ Hz and $\omega_{\mathrm{ax}}/2\pi = 47(5)$ Hz in radial and axial direction, respectively. The frequencies have been measured by adiabatically shifting the centre of the magnetic trap by one pair of the offset coils and then abruptly switching off this additional field, hold the atoms for a few ms in the unshifted trap and then do the TOF measurement. Taking images after different hold time allows us to extract the position of the cloud centre in the relevant direction, as the atoms oscillate with the trapping frequency (see Fig. 3.5).

The rate at which we compress the trap was found empirically to be 1.7 s. During the optimisation we strove for the least heating of the atoms in the radial direction, though the mean temperature increased from 120 µK to 420 µK. The trap depth increased to 53.3 G (7.2 mK). The trap frequencies correspond to a radial gradient of $65\,\mathrm{G\,cm}^{-1}$, an axial curvature of $9.6\,\mathrm{G\,cm}^{-2}$ and a bias field of 2 G. As the radial confinement is much stronger than the axial confinement, the cloud becomes elongated. A sample image of the cloud after compression with 5×10^8 atoms and the temperature $T = 0.42$ mK can be seen in Fig. 3.6. At this point, we have a cloud at a phase-space density $\Lambda_f = 10^{-6}$ (where the density of the atomic cloud n and the thermal de Broglie wavelength λ_{dB} can be obtained

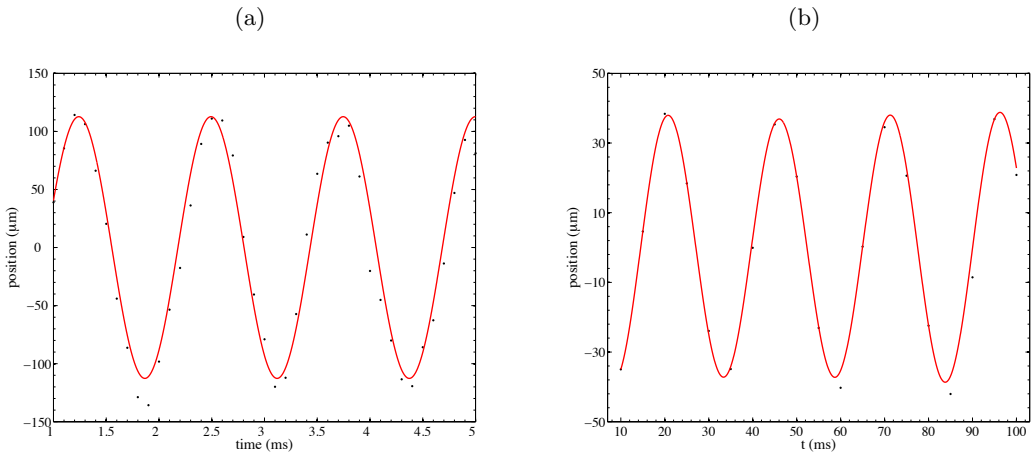

FIGURE 3.5. Magnetic trap frequency measurement in radial (a) and axial (b) directions. Using an external magnetic field the centre of mass of the cloud has been adiabatically shifted by several μm. By abrupt switch-off of the offset field we measured the position of the centre of the cloud. The fitted curves give $\omega_{\mathrm{rad}}/2\pi = 800(13)\,\mathrm{Hz}$ and $\omega_{\mathrm{ax}}/2\pi = 47(5)\,\mathrm{Hz}$ in radial and axial directions respectively.

from absorption measurements), which are excellent conditions to start forced evaporative cooling.

3.3. Evaporative cooling

Further lowering of the temperature of the atoms is done by forced radio-frequency evaporation. Evaporative cooling is a powerful tool for cooling and at the same time increasing the phase-space density of the trapped gas. In this process the atoms above a certain truncation energy ϵ_t can be spin-flipped and become untrapped, whereas the remaining atoms thermalise at a lower temperature. For a constant truncation barrier (so-called plain evaporation) the rate at which atoms are evaporated from the trap can be expressed as

$$\tau_{\mathrm{ev}}^{-1} = -\frac{\dot{N}}{N} = n_0 \bar{v} \sigma \mathrm{e}^{-\eta}, \tag{3.3}$$

where $\bar{v} = \sqrt{8k_BT/\pi m}$ is the average thermal velocity of the atoms and $\eta = \epsilon_t/k_BT$ is the truncation parameter [124]. As atoms are removed from the trap, the mean energy per atom is decreased and hence the gas cools. As the temperature decreases, η becomes larger and the evaporation is exponentially suppressed. Thus, continuous reduction of ϵ_t (forced evaporative cooling), such that, for instance, η remains constant, is much more efficient way to cool the atomic sample.

This can realised by the radio-frequency-induced (rf) evaporation [124, 126–128]. The rf radiation truncates the energy to ϵ_t, above which the atoms are spin flipped and become untrapped. The remaining fraction of atoms rethermalises via elastic collisions until new

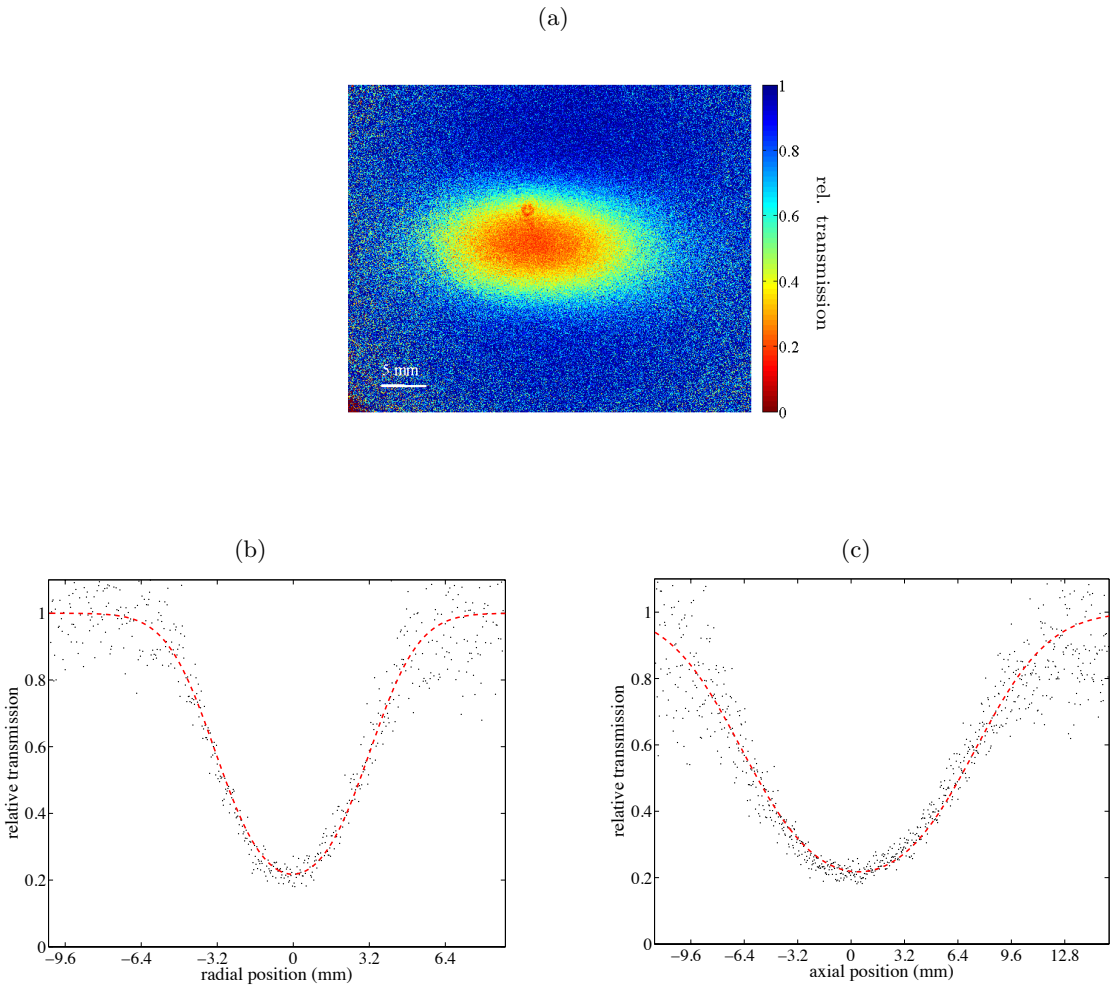

FIGURE 3.6. (a) An absorption image of the atoms in the compressed magnetic trap 3 ms after the trap has been switched off. After 1.7 s compression and 0.2 s of further trapping there are 5×10^8 atoms left in the trap that have a temperature of $T = 0.42\,\mathrm{mK}$. (b) and (c): Cross sections through the cloud centre in radial and axial direction, respectively. The dashed curves are fits of the thermal distribution given by Eq. (2.14).

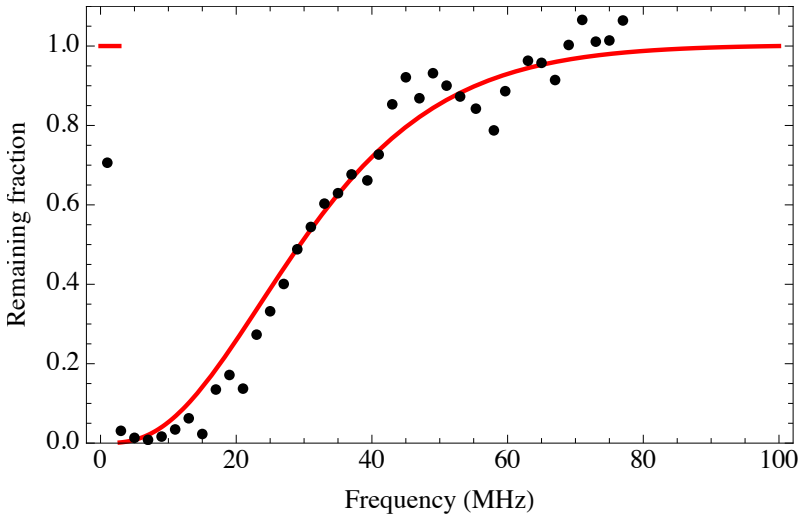

FIGURE 3.7. Measured remaining fraction of the atoms in the trap as a function of the radio frequency (dots) together with a theoretical curve (solid line) which is given by Eq. (3.4). The curve has no fit parameters.

equilibrium at lower temperature is reached. In order to force the cooling to proceed, one should lower the truncation energy further. The lowering of ϵ_t is done on a timescale slow in comparison to the thermalisation, which is the time required to achieve thermal equilibrium in the cloud. Moreover, it should be done such that every phase-space density increase is done with minimal loss of atoms. Radio-frequency induced evaporation can be completely decoupled from the design of the magnetic trap potential, i.e. varying the trap depth ϵ_t can be realised without changing the trapping potential. Furthermore, it is three-dimensional in velocity space, as the atoms are evaporated from the whole surface, defined by the ϵ_t, where the resonance condition is fulfilled. The fact that one can selectively remove the atoms with the largest total energy is an enormous advantage of a trapped gases.

In order to find the start and an approximate end frequencies we have performed an rf spilling experiment[4]. We apply an rf pulse for 100 ms at fixed frequency and with a power of 10 W to make sure that all atoms above given energy leave the trap. The remaining fraction of the atoms is released from the trap after 50 ms and is measured in the TOF. The loss of the number of atoms in the trap when going instantaneously from η to η' is given by Eq. (A.11) [83, 124]. Using Eq. (A.8) the fraction of the atoms left in the cloverleaf trap becomes

$$N' = \frac{3P(4,\eta') + 2\frac{U_0}{k_B T}P(3,\eta')}{3P(4,\eta) + 2\frac{U_0}{k_B T}P(3,\eta)}. \tag{3.4}$$

[4]In theory the bias field could be measured with a Hall probe. However, given the physical dimensions of the sensor we were not able to resolve the exact trap minimum.

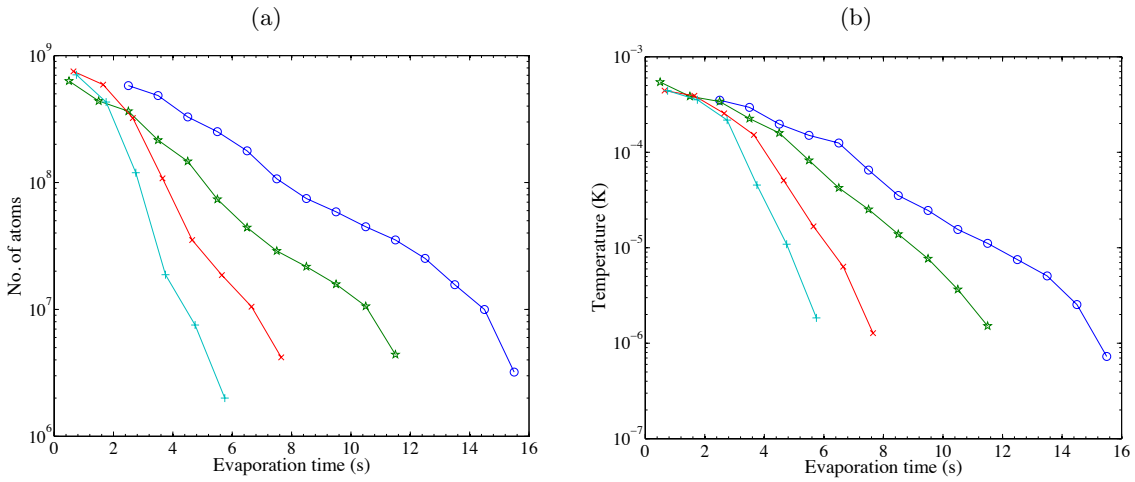

FIGURE 3.8. Evolution of the number of atoms (a) as well as the temperature (b) during the exponential rf sweep with different time duration: 6 s (pluses), 8 s (crosses), 12 s (stars) and 16 s (circles). We assume ±10% of systematic error in the determination of the number of atoms and the temperature (see Sec. 2.5.1).

Figure 3.7 shows the experimental results together with a theoretical prediction (there were no fit parameters). The results show a good agreement between theory and the experiment. Below 6 MHz the rf energy is smaller than the trap bottom and atoms are no longer removed.

Following the formalism of Walraven [127] it can be shown that for forced evaporative cooling at constant truncation parameter η

$$\frac{T}{T_0} = \left(\frac{N}{N_0}\right)^{\nu} \quad \text{with} \quad \nu = \frac{1}{3}(\eta - 2). \tag{3.5}$$

This means that there is cooling with decreasing number of atoms already for $\eta > 2$. As the temperature decreases faster with increasing η, the parameter ν can be used to describe the efficiency of evaporation and Eq. (3.5) can rewritten as

$$\nu = \frac{d(\ln T)}{d(\ln N)} = \frac{\dot{T}/T}{\dot{N}/N}. \tag{3.6}$$

In other words the efficiency ν is a measure of the temperature decrease per lost atom. Similarly to Eq. (3.5) it can be shown that, in spite of substantial loss of atoms in the evaporation process, the central density of the atomic cloud increases for $\eta > 4$. In order to realise such a density increase with large η, the evaporation has to be slow. This limit is called a "run-away" evaporation as the process proceeds faster and faster with decreasing temperature.

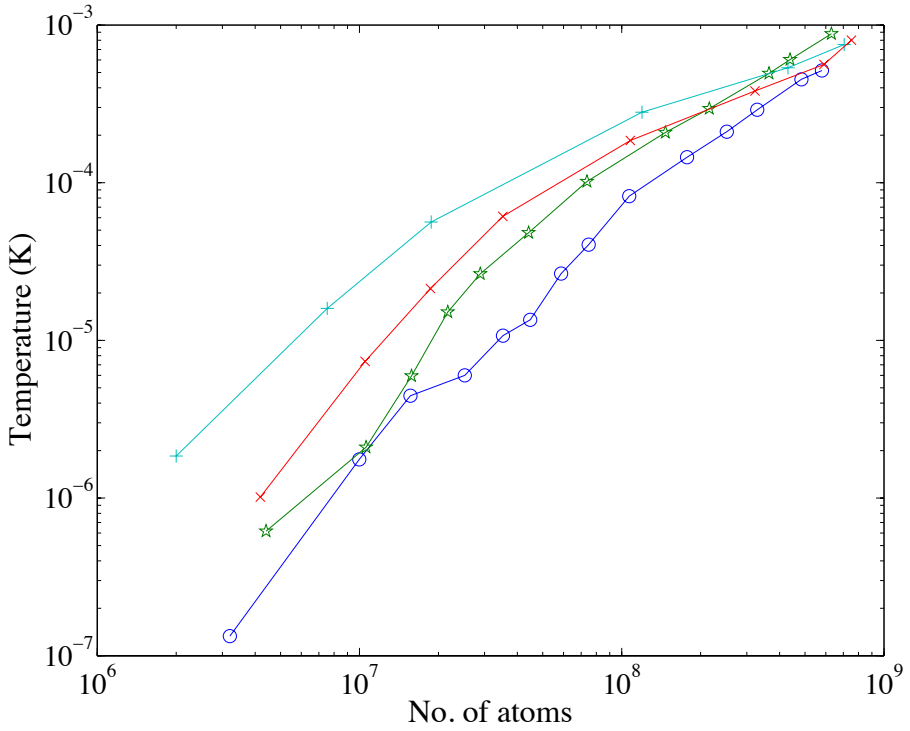

FIGURE 3.9. Evolution of the number of atoms versus the temperature during the exponential rf sweep with different time duration: 6 s (pluses), 8 s (crosses), 12 s (stars) and 16 s (circles). The steepest slope indicates the most efficient cooling.

We apply the rf radiation using two coils connected in series that are positioned close to the trapping region inside the vacuum chamber as described in Sec. 2.8. The magnetic field vector is positioned in the horizontal (xy) plane and is perpendicular to the bias field of the trap.

Ideally one would have to split the sweep into a few parts and optimise each ramp separately, yet due to the technical limitations of our rf generator this is not easily done. Instead we are using a single logarithmically-decaying frequency sweep. The truncation energy is determined by the rf frequency $\epsilon_t = \hbar\omega_{rf} - 2\mu_B B_0$, with $B_0 = 2\,\mathrm{G}$, thus the atoms with an energy $\geq \epsilon_t$ will be transferred to the magnetically untrapped state. We find the optimal ramp by utilisation of a logarithmic rf sweep that starts at 75 MHz and terminates at 6 MHz for different duration. To analyse the efficiency of the cooling process, we interrupt the sweep at various instants of time, take an absorption image after a certain TOF. At each instant of time, the TOF series allows us to obtain the number of atoms as well as temperature of the cloud. Figures 3.8(a) and (b) present the optimisation of the frequency sweep for various ramps, though, these figures are inconclusive. If we plot the cloud temperature as function of the number of atoms (c.f. Fig. 3.9) then, following Eq. (3.6), the steepest slope should indicate the most efficient cooling. As expected the longer the rf ramp the more efficient cooling is. However, the cooling efficiency of the

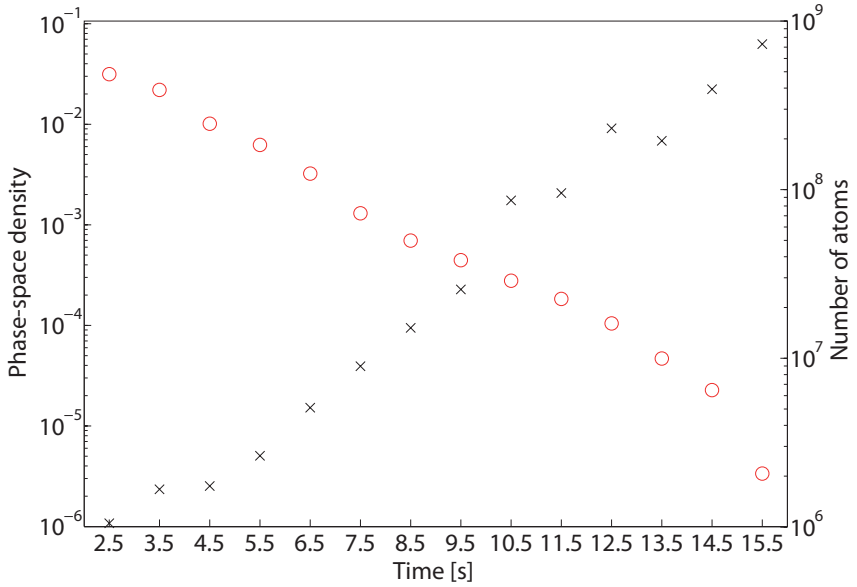

FIGURE 3.10. Increase of the phase-space density (black crosses) and decrease of the number of atoms (red circles) during the evaporative cooling. We lose more than 99 % of the atoms, but the phase-space density increases by five orders of magnitude. While in this realisation we evaporated the atoms over a time span of 16 s, degeneracy of the atoms can be achieved in a fraction of this time, but at the expense of the remaining number of atoms in the trap.

sweeps lasting 12 s and 16 s is comparable. This might be caused by the finite lifetime of the cloud in the trap, as the atoms in the longer ramp are lost from the trap before they rethermalise.

We evaporate the atoms right after compression of the magnetic trap, following the Doppler cooling stage, by applying up to 20 W of rf power to a pair of coil antennas and ramping the frequency exponentially from 75 MHz to below 6 MHz over a time period of typically 12 s, before the BEC is reached. Figure 3.10 shows the increase of phase-space density and decrease of the number of atoms during the evaporation cycle. The BEC can be achieved even for the shortest ramps but with much lower atom number.

CHAPTER 4

A Bose-Einstein condensate

This chapter describes an achievement of one of the very few Bose-Einstein condensates of metastable helium-4, similar to experimental realisations reported in [31, 32, 60, 129–131]. Comparison of the shape of the momentum distribution and the expansion dynamics indeed proves that the gas has undergone the phase transition. We measure lifetime of the cloud and the number of atoms. Finally, outcoupling of the atoms by rf radiation is shown, which can be referred to as a pulsed matter-wave "laser" [132].

At the end of the rf ramp, when the phase-space density approaches unity, the de Broglie wavelength of the atoms is so large that the wave functions of all atoms overlap. Then the atoms undergo a phase transition to the BEC. The Bose degeneracy manifests itself by a formation of a narrow peak in the density distribution. Shortly before the condensation the degeneracy is heralded by a deviation of the momentum distribution from Maxwell-Boltzmann distribution (as described in Sec. 2.5.1). Thus one has to fit the density profile with Eq. (2.19). Typically we get a few 10^6 atoms in the BEC. Shorter rf ramps also lead to a BEC, albeit with smaller numbers of atoms.

4.1. Theory

Many excellent review articles and books have been written about Bose-Einstein condensation, for instance [85, 133–135]. In this section we will briefly review some essential concepts.

We are treating our cloud as an ideal bosonic gas. Bose-Einstein condensation is the macroscopic occupation of a single quantum state. In a typical BEC this single quantum level is the ground state of the external potential. Typical experiments create a harmonic potential that can be written as

$$V_{ext}(\mathbf{r}) = \frac{1}{2}m\omega_\rho^2\rho^2 + \frac{1}{2}m\omega_y^2 y^2, \tag{4.1}$$

where $\omega_{\rho,\mathrm{y}}$ are trapping frequencies in radial and axial directions, respectively. For non-interacting bosons in the three-dimensional harmonic potential one can find that the transition temperature is given by [133]

$$T_c = \frac{\hbar\omega_{ho}}{k_B}\left(\frac{N}{\zeta(3)}\right)^{\frac{1}{3}} \approx \frac{0.94\hbar\omega_{ho}N^{1/3}}{k_B}, \tag{4.2}$$

where $\zeta(x) = \sum_{j=1}^{\infty} j^{-x}$ is the Riemann zeta function and $\omega_{ho} = \sqrt[3]{\omega_{\mathrm{ax}}\omega_{\mathrm{rad}}^2}$ is the mean trapping frequency. For example, one million helium-4 atoms undergo the BEC phase transition at around 1.4 µK. Taking into account interactions between atoms and the finite size of the cloud the critical temperature can shift even by 15% [32, 136, 137]. Once

the atoms are cooled below the critical temperature ($T < T_c$) the fraction of condensed atoms N_c scales as

$$\frac{N_c}{N} = 1 - \left(\frac{T}{T_c}\right)^3. \tag{4.3}$$

Thus only at $T = 0$ is the entire population is in the condensate.

The ground state of N non-interacting bosons in this potential can be written as a product of independent wave functions $\psi(\mathbf{r}_1, \ldots, \mathbf{r}_N) = \phi(\mathbf{r}_1) \cdots \phi(\mathbf{r}_N)$. Taking interactions between particles into account leads to a modification of the Schrödinger equation by a non-linear term, the so-called mean-field potential, thus

$$\left(-\frac{\hbar^2\nabla^2}{2m} + V_{ext}(\mathbf{r}) + gN|\phi^2(\mathbf{r})|\right)\phi(\mathbf{r}) = \mu\phi(\mathbf{r}), \tag{4.4}$$

where an energy $\mu = \partial E/\partial N$ is a chemical potential and $g = 4\pi\hbar^2 a/m$ is the strength of mean-field interaction, with a being an s-wave scattering length. For $a > 0$ the interaction is repulsive, whereas for negative a it is attractive. Equation (4.4) is a Gross-Pitaevski equation describing the mean-field approximation.

For sufficiently large clouds, the kinetic energy is small compared to the potential energy and we can neglect $\nabla^2\phi$ in Eq. (4.4), thus

$$\left[\frac{1}{2}m(\omega_\rho\rho^2 + \omega_{ax}y^2) + gN|\phi(\mathbf{r})|^2\right]\phi(\mathbf{r}) = \mu\phi(\mathbf{r}). \tag{4.5}$$

This is the Thomas-Fermi approximation. From this we find the single-particle wave function

$$\phi(\mathbf{r}) = \sqrt{\frac{\mu - \frac{1}{2}m(\omega_\rho\rho^2 + \omega_{ax}y^2)}{gN}}, \tag{4.6}$$

for $\mu > V_{ext}(\mathbf{r})$ and $\phi(\mathbf{r}) = 0$ otherwise. The density distribution is given by $n(\mathbf{r}) = |\phi(\mathbf{r})|^2$ which is an inverted parabola with radii

$$r_i = \sqrt{\frac{2\mu}{m\omega_i^2}}, \tag{4.7}$$

where subscript i denotes the axial or radial direction. In the Thomas-Fermi limit we can derive the chemical potential from the normalisation condition $\int n(\mathbf{r})\,\mathrm{d}^3r = 1$ that yields

$$\mu = \frac{\hbar\omega_{ho}}{2}\left(\frac{15Na}{a_{ho}}\right)^{2/5} \tag{4.8}$$

where $a_{ho} = \sqrt{\hbar/(m\omega_{ho})}$ is the size of the ground state wave function.

From Eq. (4.7) knowing our trapping frequencies we can estimate the initial size of the condensate; we find radial and axial size to be $R_{\mathrm{rad}} \approx 7\,\mu\mathrm{m}$ and $R_{\mathrm{ax}} \approx 140\,\mu\mathrm{m}$, respectively.

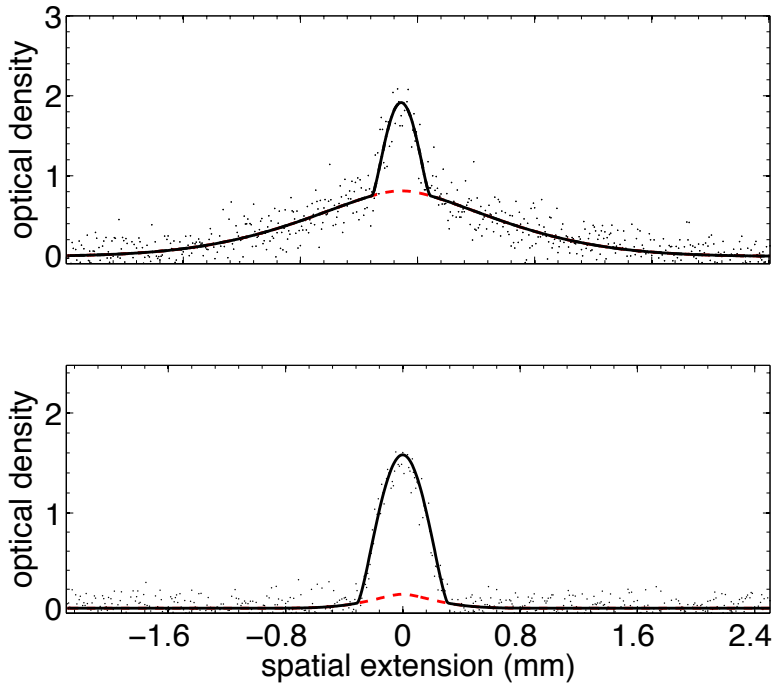

FIGURE 4.1. Density profiles (10 pixel line average) of a partly condensed atomic cloud (a) and almost a pure BEC cloud (b), obtained by using different end frequencies of the rf ramp. The images were taken 15 ms after release of the atoms from the trap. The black solid line represents the fit of the bimodal distribution, the red dashed line the thermal component, from which the temperature of the cloud can be inferred.

4.2. Expansion of the condensate

Atoms expand after switch-off of the trap. During expansion the cloud preserves its parabolic density distribution at each instant of time [85]. Castin and Dum [87] used a classical model to describe the evolution of the density after the trap switch-off. They found that at each instant of time the radii evolve as

$$r_i(t) = r_i(0)\lambda_i(t), \quad i = \{\mathrm{ax},\ \mathrm{rad}\} \tag{4.9}$$

where the scaling parameters λ_i, as seen in Eqs. (2.27), can be derived by solving a set coupled differential equations

$$\ddot{\lambda}_{\mathrm{rad}} = \frac{\omega_{\mathrm{rad}}^2(0)}{\lambda_{\mathrm{rad}}^3\lambda_{\mathrm{ax}}} \quad \text{and} \quad \ddot{\lambda}_{\mathrm{ax}} = \frac{\omega_{\mathrm{ax}}^2(0)}{\lambda_{\mathrm{rad}}^2\lambda_{\mathrm{ax}}^2} \tag{4.10}$$

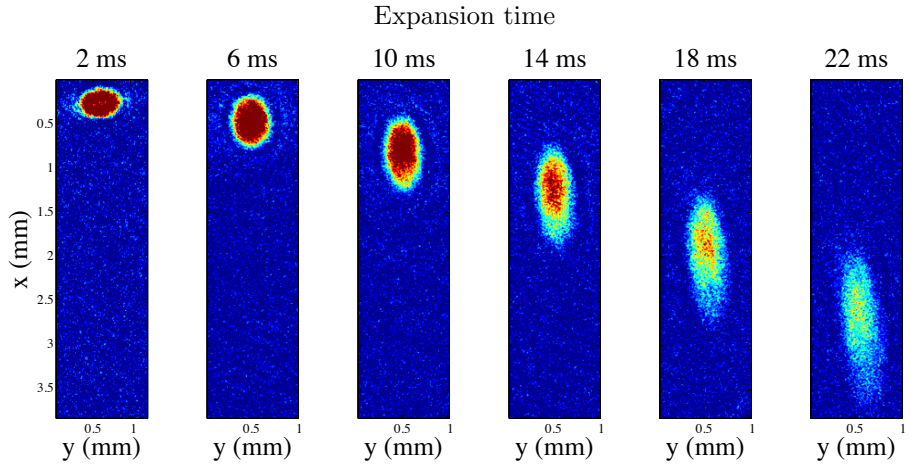

FIGURE 4.2. Absorption images of the condensed cloud falling under gravity. The atoms are released from a trap with an aspect ratio 1:17. The observed anisotropic expansion is a clear signature of a BEC.

with the starting conditions $\lambda_i(0) = 1$ and $\dot{\lambda}_i(0) = 0$, since the gas is initially at rest. Thus

$$\lambda_{\mathrm{rad}} = \sqrt{1 + \omega_\rho^2 t^2}, \tag{4.11}$$

$$\lambda_{\mathrm{rad}} = 1 + \left(\frac{\omega_{\mathrm{ax}}}{\omega_{\mathrm{rad}}}\right)^2 \left[\omega_{\mathrm{rad}} t \arctan(\omega_{\mathrm{rad}} t) - \ln\sqrt{1 + (\omega_{\mathrm{rad}} t)^2}\right] + O\left(\left(\frac{\omega_{\mathrm{ax}}}{\omega_{\mathrm{rad}}}\right)^4\right)$$

where one sees that after sufficiently long time $(\omega_{\mathrm{rad}} t)^2 \gg 1$, both directions tend to expand linearly. After a certain time the radial radius will be greater than the axial one, therefore it will change the aspect ratio $\epsilon = r_{\mathrm{rad}}/r_{\mathrm{ax}}$ of the condensate from $\epsilon < 1$ to $\epsilon > 1$. In the limit of large times, ϵ tends to the value of $\epsilon(\infty) = 2\omega_{\mathrm{rad}}/(\pi\omega_{\mathrm{ax}})$. Observation of the aspect ratio is thus a powerful tool to observe the boson degeneracy.

Figure 4.2 shows a typical time-of-flight series of a cloud that is released from a trap with an aspect ratio of 1:17. The images were taken after 2 to 22 ms of free expansion and present an expected anisotropic expansion which is remarkably different from the isotropic expansion of the thermal cloud. The evolution of the aspect ratio of the radii is shown in Fig. 4.3. Initially the condensate is elongated in the axial direction, yet as the radial expands much more quickly, around 4 ms the aspect ratio inverts and the cloud is elongated radially. The radial direction expands more quickly until the aspect ratio asymptotically achieves the value of around $\epsilon(\infty) \approx 11$ when both directions expand at the same rate.

Observation of the BEC cloud on the MCP detector was not as straightforward as it seemed at first. Even though, we saw condensed atoms on the MCP from the very end of the evaporation ramp. We could not see a BEC cloud on the detector after the switch-off of the magnetic trap. We suspect that during the sudden switch-off of the magnetic trap, the BEC gets a momentum kick that is so large that the atoms miss the DLD detector.

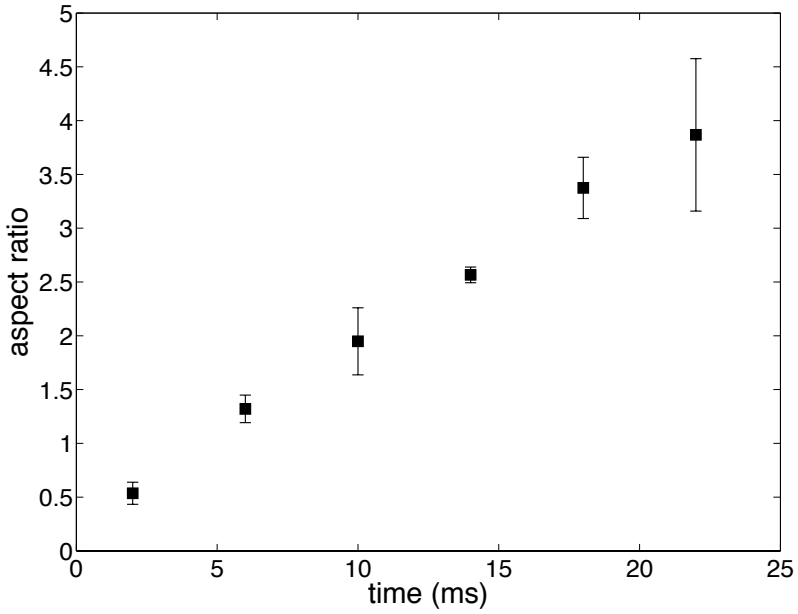

FIGURE 4.3. Time evolution of the aspect ratio, ϵ, of the extracted radii in radial and axial directions (same data as in Fig. 4.2). Initially (up to about 4 ms) the condensate is elongated along the axial direction, but then the aspect ratio is inverted. For aspect ratio $\epsilon(\infty) \approx 11$ the rate of expansion should be the same for both directions.

This kick, though, does not matter for the absorption imaging. Thus, the data presented in this chapter are mostly taken with the optical imaging.

We attempted to reduce this kick by changing the timing of the switch-off between different sets of coils, yet without any success. Another way to eliminate it is to adiabatically ramp down the currents[1]. However, this method has a huge disadvantage since the switch-off time is on a longer timescale than the oscillation frequency of the atoms in the trap, which leads to changes in the cloud shape and distortion of the time-of-flight expansion. As a result the measurements do not reflect the momentum distribution of the original trapped cloud. A sample image after such an adiabatic switch-off can be seen in Fig. 4.4. It can be compared to a BEC fraction that has been outcoupled by an rf pulse in Fig. 4.6. Even though Fig. 4.4 does not reflect the true momentum distribution in the trap, one can clearly see an integrated in time momentum distribution "pancake" of the condensed atoms. Its asymmetric shape is another proof that we observe a BEC on the detector.

[1]An adiabatic ramp-down minimises the torque that the coils impart on their holder. Therefore it also prolongs the mechanical stability of the trap.

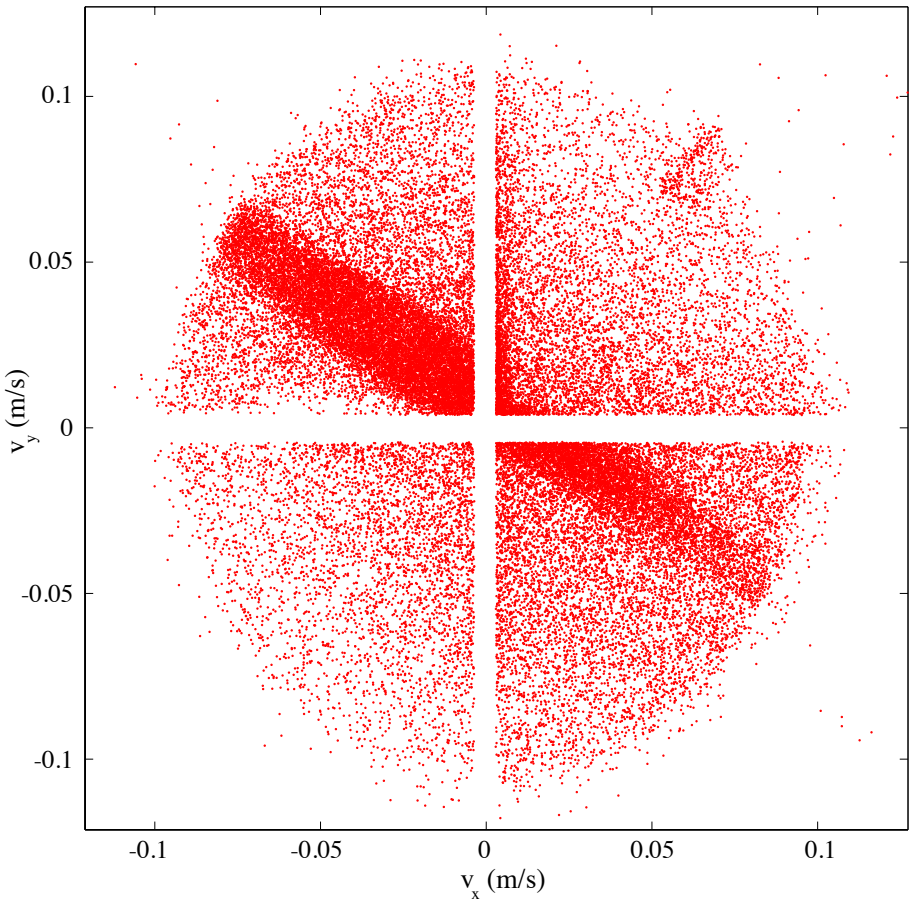

FIGURE 4.4. (Top view) Time-of-flight measurement of the BEC cloud on the DLD after switching off the magnetic trap currents by an adiabatic ramp. The condensed atoms are seen as a dense flat strip across the detector.

4.3. Lifetime of the condensate

The formation and the decay of the condensate has been a subject of study and discussions in a number of experiments [138–141]. The lifetime of the condensate gives a measure of, for example, thermal excitations due to the fluctuations of the trap currents. Furthermore, it is important to have cloud lifetime which is significantly longer than the time scale of planned experiments. As these involve outcoupling and entangling of single-atomic pairs, it is favourable to work on one BEC instead of repeating the sequence too frequently. Studying the density dependence of the condensate lifetime is also of scientific interest, since the two-body and three-body loss coefficients, that one obtains from analysing the decay of the trapped atom number, are closely related to the correlations between the particles [142].

The measurement was performed by holding the atomic cloud in the trap with the rf knife turned on at the final rf frequency until the trap has been switched off.Then

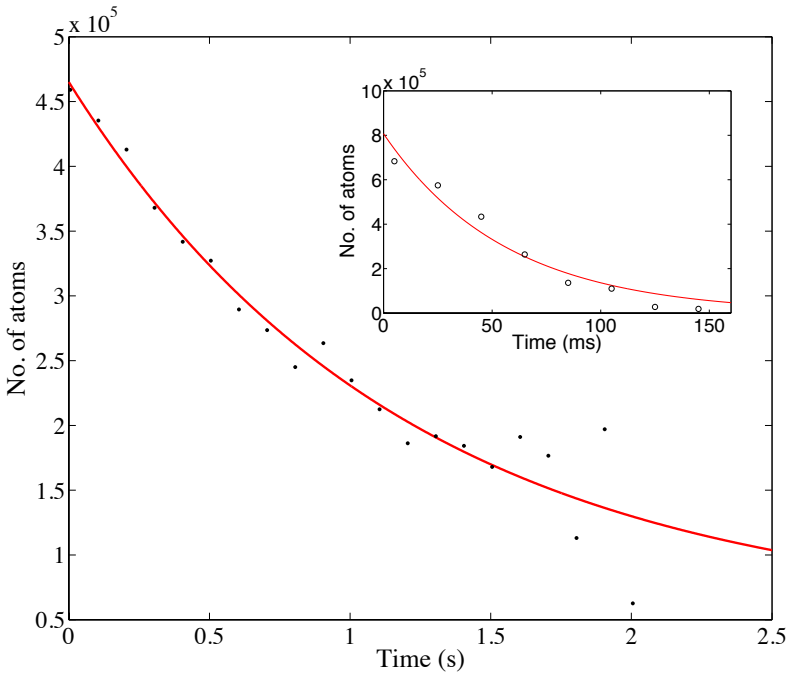

FIGURE 4.5. Number of atoms in the condensate with and without (see inset) the rf knife plotted as a function of storage time. Data was taken with absorption imaging. The fitted curves show exponential decay which corresponds to one-body losses.

the absorption image was taken, from which the number of condensed atoms has been extracted. Assuming one-body losses the lifetime of the condensate can be determined. Figure 4.5 shows the dependence of the atom number in the condensate on the storage time in the trap. Fitting an exponential decay, given by the formula $dN/dt = -N(t)/\tau$, to the data, it yields a lifetime of $\tau_{\mathrm{rf_{on}}} = 1.5\,\mathrm{s}$ and of only $\tau_{\mathrm{rf_{off}}} = 60\,\mathrm{ms}$ when the rf knife is present and absent respectively. These curves indicate that one-body losses are dominant and higher order losses are negligible. Our limitation is probably caused by current fluctuations that lead to thermal excitations of the atoms. A significant increase of the lifetime of the condensed atoms by the rf knife is promising, though compared to other helium BECs there is about an order of magnitude of room for improvement, e.g. in the Amsterdam group the BEC can be observed up to 75 s after it was produced [129].

4.4. Radio-frequency outcoupling

A Bose-Einstein condensate is a sample of atoms with macroscopic population in the ground state. This population forms a coherent matter wave, which can be described by the nonlinear Schrödinger equation. While the outcoupling can be realised in various ways, the most straightforward one is using a pulse (or sweep) of rf radiation. This rf

radiation transfers coherently some of the atoms to magnetically insensitive ($m = 0$) or high-field seeker ($m = -1$) states.

A weak rf field is used to extract the atoms from the condensate over a period of up to a few ms. The output coupling mechanism can be visualised as a small, spatially localised leak in the trapping potential. The condensate wave function passes through the leak and forms an expanding atomic pulse. The rf-controlled outcoupling mechanism of a BEC to "free" modes can be done in a controlled and non-dissipative way. It has been first realised by Mewes et al. [23] and is often referred to as an atom laser since it is a coherent source of atoms, analogously to laser [132]. A short resonant pulse prepares the atoms in a superposition of all magnetic sublevels of 2^3S_1 manifold with coefficients [23] $a_{+1} = \cos^2(\omega_R t_{\text{pulse}}/2)$, $a_0 = i/\sqrt{2}\sin(\omega_R t_{\text{pulse}})$ and $a_{-1} = -\sin^2(\omega_R t_{\text{pulse}}/2)$, where $\omega_R = g\mu_B B_{\text{rf}}/2\hbar$ is the single-particle Rabi frequency. It is also possible to apply a linear rf sweep with a constant rate. A radio-frequency sweep through a resonance has the advantage that it is not affected by small drifts in the resonance frequency due to fluctuations of the bias field in the trap centre. However, such a ramp outcouples more atoms from the thermal fraction, which in some cases is not desired.

The outcoupling is performed with the same pair of coils that is used for evaporative cooling and that are described in Sec. 2.8. To detect the atoms we use the MCP detector that can be thought as a single-particle counter for an atom laser. The outcoupled fraction is too dilute to be seen with absorption imaging, but one could quantify it up to a certain degree by measuring atom losses in the cloud using absorption imaging.An outcoupled fraction of the condensed atoms is shown in Fig. 4.6. In this realisation we observe 1.25×10^5 atoms which is roughly 10% of the condensed number of atoms. The saturation of the detector can be seen in Fig. 4.6(c) and (d), even though in Fig. 4.6(a) and (b) there are no obvious signs of saturation. It can be avoided by outcoupling even smaller fraction of atoms. We fitted a function given by Eq. (2.36) to the data in Fig. 4.6(d), excluding the central part of the signal as there the counts on the detector were saturated. The observed uneven height distribution of the number of counts between quadrants results from the fact that due to the ageing of the MCP its amplification has decreased. Therefore the analogue signals from the delay lines have lower amplitudes than expected and they get discarded in the CFD. For this reason the electronics has to be recalibrated or the MCP has to be replaced.

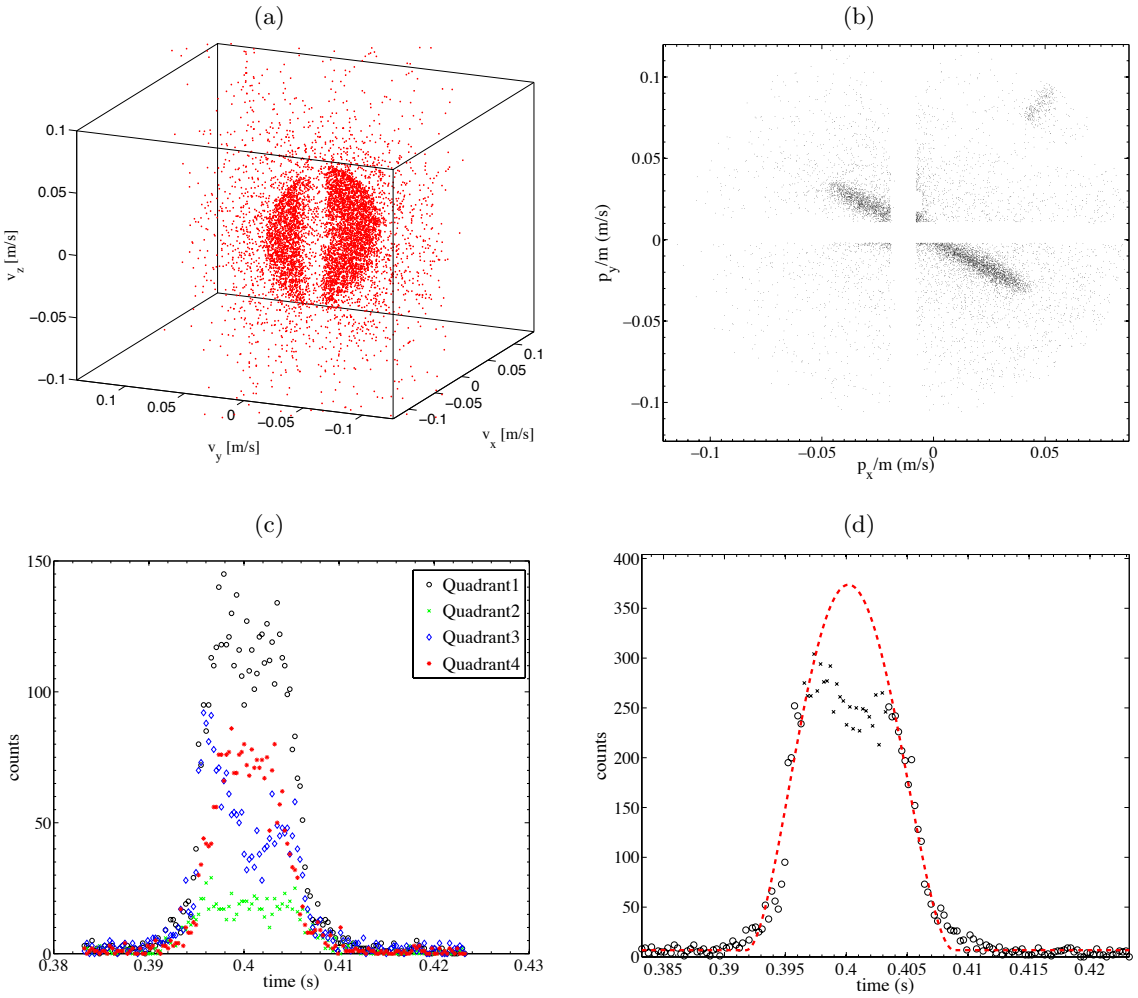

FIGURE 4.6. Sample of radio-frequency outcoupled atoms out of the BEC. (a) A three-dimensional momentum distribution of the atoms in the trap. (b) Top view of (a). (c) Histograms (in 150 bins) of time-of-flight counts from individual quadrants. Each quadrant shows a saturation of the counts due to the high density of the cloud. (d) A sum of histograms from (c) with a fitted curve (dashed) for the flux of condensed atoms given by Eq. (2.36). Because of the saturation of the detector some of the data were excluded (crosses) from the fit.

CHAPTER 5

Summary and Outlook

The realisation of a Bose-Einstein condensation of metastable helium-4 atoms was the main subject of this thesis. This BEC will eventually serve as a source for coherent matter-wave experiments. The biggest novelty our setup is the four-quadrant delay-line detector. Its four independent quadrants allow for true simultaneous detection. The detector will help overcome one of the biggest challenges in this experiment, i.e. saturation of the detector from the condensate clouds that did not scatter.

To achieve a Bose-Einstein condensate, a sequence of well-controlled manipulation and cooling steps has been designed, developed, implemented and characterised. First, the atoms are excited to their metastable state within a dc-discharge source. Transverse laser cooling increases the atomic beam flux, which is necessary to achieve high loading rates into a magneto-optical trap. The MOT is loaded after deceleration of the atoms in a Zeeman slower, containing typically 10^9 at a temperature of 1 mK. Following the transfer to a magnetic trap, the atoms are cooled to degeneracy, with typically a few 10^6 atoms at temperatures of around 1.4 µK.

Moreover, a micro-channel plate in combination with a delay-line detector with four quadrants has been attached to the system and its characteristics were tested. The delay-line detector has an efficiency of 10% and is capable of resolving single-atom detection events temporally with 220(18) ps and spatially with 177(32) µm at rates of several 10^6 events per second per quadrant. Therefore, our detector is a frontrunner when it comes to spatial resolution, compared to other helium BECs. It allows for a full 3D reconstruction of the atomic cloud. Moreover, when one of the quadrants is saturated (e.g. by a dense cloud of atoms), the other allow for simultaneous detection.

The combination of a BEC as a source for coherent matter waves and single-atom detection capability to measure correlations will enable us to perform experiments with non-classical states of matter waves that can be created via four-wave mixing in the condensate. The combination of high count rates, good resolution and true simultaneous detection with independent quadrants of the delay-line detector provides excellent conditions for these types of experiments. It will bring a three-dimensional version of the original Einstein-Podolsky-Rosen paradox closer to realisation in a matter-wave system and push the field closer to exploiting the possibilities of matter-wave quantum entanglement.

A natural follow-up experiment would be a realisation of a Hong-Ou-Mandel (HOM) effect, which has become a textbook example of quantum mechanical destructive interference of indistinguishable bosons [143]. Even though, the HOM experiment has been recently realised in an atomic system by Kaufman et al. [30] and Lopez et al. [36], its exploration with massive particles remains largely unexplored field.

Generation and detection of such quantum correlations in matter waves can be extended towards stricter tests of quantum mechanics such as those implied by the violation of a Bell's inequality [4]. This would enable fundamental tests of quantum mechanics into previously unexplored regimes. One of the open questions in quantum mechanics is the boundary between classical and quantum world. For matter-waves there exists no analogue of a classical wave obeying Maxwell equations.

Dealing with massive particles lets us perform experiments where both quantum mechanics and gravity play a role. One of the pioneering experiments observing gravitational phase shifts was performed in a neutron interferometer by Colella, Overhauser and Werner (COW) [144]. We would extend this experiment by performing phase-shift measurements on entangled particles. While due to intensity limitations it will be difficult to compete with atomic interferometers [145], it would for the first time allow for an observation of gravitational phase shift for an entangled state.

Recent demonstration of entanglement with orbital-angular momentum (OAM) of photons reaching $300\hbar$ [146] and possibility of transfer of the OAM from a laser beam onto the BEC [147] would pave the way for many fascinating experiments. These would include entanglement between photonics OAM and topological charge in a BEC or the study of collisional entanglement creation within a BEC carrying vortices. The high OAM of photons could also be used to generate an almost perfect box potential by utilisation of optical trapping fields.

The addition of fermonic species (^{3}He) to the experimental setup would allow us to explore quantum mechanics beyond what is possible with photons since fermonic experiments do not have an analogue in quantum optics. We would be able to investigate whether processes that usually are described using bosonic stimulation, such as four-wave mixing, matter-wave amplification and superradiance, can be also observed in a fermionic system. In fact there exist few theoretical proposals generalising these phenomena to coherence properties of atomic gas and to multi-particle interference effects [148, 149].

There is a plethora of experiments that we would like to perform with such a system. Nevertheless, only few of them are listed in the preceding paragraphs to show the versatility of our system. The realisation of the Bose-Einstein condensation in our laboratory sets the stage for future and I am confident that owing to the system presented in this dissertation and to the commitment of the team, with whom I had pleasure to work with, they will allow for a realisation and a detection of momentum entangled states. I strongly believe that these goals will be achieved in the near future.

APPENDIX A

Statistical mechanics of the magnetic trap

To describe the atomic density in a trap with a finite depth, an approach of Luiten et al. [124] is used. Below only a summary is given of the equations needed to calculate the density distribution. When we consider only atoms with energies lower than the trap depth ϵ_t the truncated density distribution becomes

$$n(r) = n_0 \mathrm{e}^{-\frac{U(r)}{k_B T}} P\left(\frac{3}{2}, \frac{\epsilon_t - U(r)}{k_B T}\right), \tag{A.1}$$

with $P(a, \eta)$ an incomplete gamma function and the trapping potential $U(r)$ given by

$$U(x, y, z) = \sqrt{\alpha^2(x^2 + y^2) + (U_0 + \beta z^2)^2} - U_0 \tag{A.2}$$

where $U_0 = 2\mu_B B_0$ (in case of $2^3\mathrm{S}_1$ state in ^{4}He) is the minimal potential energy. An incomplete gamma function P can be expressed in terms of a gamma function Γ as

$$P(a, \eta) = 1 - \frac{\Gamma(a, \eta)}{\Gamma(a, 0)} = \frac{\int_0^\eta t^{a-1}\mathrm{e}^{-t}dt}{\int_0^\infty t^{a-1}\mathrm{e}^{-t}dt}. \tag{A.3}$$

Here T is still called the temperature, yet strictly speaking a thermodynamic temperature is not defined for a nonequilibrium distribution. The central density can be expressed as

$$n(0) = n_0 P\left(\frac{3}{2}, \eta\right), \tag{A.4}$$

where η is the truncation parameter given by

$$\eta = \frac{\epsilon_t}{k_B T} \tag{A.5}$$

and

$$n_0 = \frac{N}{\lambda_{dB}^3 \zeta}, \tag{A.6}$$

is the central density only in the limit of infinite trap depth, with thermal de Broglie wavelength

$$\lambda_{dB} = \sqrt{\frac{2\pi\hbar^2}{m k_B T}} \tag{A.7}$$

and a single-atom partition function ζ (in case of a cloverleaf trap)

$$\zeta = 6A_{IQ}(k_B T)^4 \left[P(4, \eta) + \frac{2U_0}{3k_B T} P(3, \eta)\right], \tag{A.8}$$

with

$$A_{IQ} = \frac{m^{3/2}}{4\sqrt{2\beta}\alpha^2\hbar^3}. \tag{A.9}$$

In the first approximation when $\eta \geq 3$, $P(\frac{3}{2}, \eta)$ approaches unity and the central density is almost equal to $n(0)$. The internal energy of the gas is equal to

$$E = \frac{12P(5,\eta) + 6\frac{U_0}{k_BT}P(4,\eta)}{3P(4,\eta) + 2\frac{U_0}{k_BT}P(3,\eta)} Nk_BT. \tag{A.10}$$

The loss δN in the number of atoms produced by instantaneously lowering the trap depth from ϵ_t to ϵ_t' is given by

$$\delta N = N\left(\frac{\zeta(\eta')}{\zeta(\eta)} - 1\right), \tag{A.11}$$

where primed symbols correspond to trap parameters after truncation.

Bibliography

[1] A. Einstein, B. Podolsky, and N. Rosen, *Can Quantum-Mechanical Description of Physical Reality Be Considered Complete?*, Physical Review **47** (1935), no. 10, 777–780. 1

[2] E. Schrödinger, *Die gegenwaertige Situation in der Quantenmechanik*, Naturwissenschaften **23** (1935), no. 49, 823–828. 1

[3] E. Schrödinger and M. Born, *Discussion of Probability Relations between Separated Systems*, Mathematical Proceedings of the Cambridge Philosophical Society **31** (1935), no. 04, 555. 1

[4] J. Bell, *On the Einstein-Podolsky-Rosen paradox*, Physics **1** (1964), no. 3, 195–200. 1, 90

[5] J. F. Clauser, M. A. Horne, A. Shimony, and R. A. Holt, *Proposed experiment to test local hidden-variable theories*, Physical Review Letters (1969), 880–884. 1

[6] J. Clauser, *Experimental distinction between the quantum and classical field-theoretic predictions for the photoelectric effect*, Physical Review D **9** (1974), no. 4, 853–860.

[7] A. Aspect, J. Dalibard, and G. Roger, *Experimental Test of Bell's Inequalities Using Time- Varying Analyzers*, Physical Review Letters **49** (1982), no. 2, 1804–1807. 1

[8] A. Zeilinger, *Experiment and the foundations of quantum physics*, Reviews Of Modern Physics **71** (1999), no. 2, S288–S297. 1

[9] M. A. Rowe, D. Kielpinski, V. Meyer, C. A. Sackett, W. M. Itano, C. Monroe, and D. J. Wineland, *Experimental violation of a Bell's inequality with efficient detection*, Nature **409** (2001), no. 6822, 791–794. 1

[10] R. Blatt and D. Wineland, *Entangled states of trapped atomic ions*, Nature **453** (2008), no. 7198, 1008–1015. 1

[11] M. Steffen, M. Ansmann, R. C. Bialczak, N. Katz, E. Lucero, R. Mcdermott, M. Neeley, E. M. Weig, A. N. Cleland, and J. M. Martinis, *Measurement of the Entanglement of Two Superconducting Qubits via State Tomography*, Science **313** (2006), no. 5792, 1423–1425. 1

[12] J. Hald, J. L. Sørensen, C. Schori, and E. S. Polzik, *Spin Squeezed Atoms: A Macroscopic Entangled Ensemble Created by Light*, Physical Review Letters **83** (1999), no. 7, 1319–1322. 1

[13] C. Gross, H. Strobel, E. Nicklas, T. Zibold, N. Bar-Gill, G. Kurizki, and M. K. Oberthaler, *Atomic homodyne detection of continuous-variable entangled twin-atom states.*, Nature **480** (2011), no. 7376, 219–223. 1

[14] J. G. Rarity and P. R. Tapster, *Experimental Violation of Bell's Inequality Based on Phase and Momentum*, Physical Review Letters **64** (1990), no. 21, 2495–2498. 1, 2

[15] A. Perrin, H. Chang, V. Krachmalnicoff, M. Schellekens, D. Boiron, A. Aspect, and C. I. Westbrook, *Observation of Atom Pairs in Spontaneous Four-Wave Mixing of Two Colliding Bose-Einstein Condensates*, Physical Review Letters **99** (2007), no. 15, 150405. 1, 2, 43

[16] M. H. Anderson, J. R. Ensher, M. R. Matthews, C. E. Wieman, and E. A. Cornell, *Observation of Bose-Einstein condensation in a dilute atomic vapor*, Science **269** (1995), no. 5221, 198–201. 2, 7

[17] K. B. Davis, M.-O. Mewes, M. R. Andrews, N. J. van Druten, D. S. Durfee, D. M. Kurn, and W. Ketterle, *Bose-Einstein Condensation in a Gas of Sodium Atoms*, Physical Review Letters **75** (1995), no. 22, 3969–3973.

[18] C. C. Bradley, C. A. Sackett, J. J. Tollett, and R. G. Hulet, *Evidence of Bose-Einstein Condensation in an Atomic Gas with Attractive Interactions*, Physical Review Letters **75** (1995), no. 9, 1687–1690. 2

[19] M. Greiner, O. Mandel, T. Esslinger, T. W. Hänsch, and I. Bloch, *Quantum phase transition from a superfluid to a Mott insulator in a gas of ultracold atoms*, Nature **415** (2002), no. 6867, 39–44. 2

[20] S. Jochim, M. Bartenstein, A. Altmeyer, G. Hendl, S. Riedl, C. Chin, J. Hecker Denschlag, and R. Grimm, *Bose-Einstein Condensation of Molecules*, Science **302** (2003), 2101–2103. 2

[21] M. W. Zwierlein, C. A. Stan, C. H. Schunck, S. M. F. Raupach, S. Gupta, Z. Hadzibabic, and W. Ketterle, *Observation of Bose-Einstein Condensation of Molecules*, Physical Review Letters **91** (2003), no. 25, 250401–1–250401–4.

[22] M. Greiner, C. A. Regal, and D. S. Jin, *Emergence of a molecular Bose-Einstein condensate from a Fermi gas*, Nature **426** (2003), no. 6966, 537–540. 2

[23] M.-O. Mewes, M. R. Andrews, D. M. Kurn, D. S. Durfee, C. G. Townsend, and W. Ketterle, *Output Coupler for Bose-Einstein Condensed Atoms*, Physical Review Letters **78** (1997), no. 4, 582–585. 2, 86

[24] L. Deng, E. W. Hagley, J. Wen, M. Trippenbach, Y. Band, P. S. Julienne, J. E. Simsarian, K. Helmerson, S. L. Rolston, and W. D. Phillips, *Four-wave mixing with matter waves*, Nature **398** (1999), no. 6724, 218–220. 2

[25] T. Gericke, P. Würtz, D. Reitz, T. Langen, and H. Ott, *High-resolution scanning electron microscopy of an ultracold quantum gas*, Nature Physics **4** (2008), 949–953. 2

[26] W. S. Bakr, J. I. Gillen, A. Peng, S. Fölling, and M. Greiner, *A quantum gas microscope for detecting single atoms in a Hubbard-regime optical lattice*, Nature **462** (2009), 74–77.

[27] J. F. Sherson, C. Weitenberg, M. Endres, M. Cheneau, I. Bloch, and S. Kuhr, *Single-atom-resolved fluorescence imaging of an atomic Mott insulator*, Nature **467** (2010), 68–72. 2

[28] M. Schellekens, R. Hoppeler, A. Perrin, J. V. Gomes, D. Boiron, A. Aspect, and C. I. Westbrook, *Hanbury Brown Twiss effect for ultracold quantum gases.*, Science **310** (2005), no. 5748, 648–651. 2, 41

[29] R. Bücker, A. Perrin, S. Manz, T. Betz, C. Koller, T. Plisson, J. Rottmann, T. Schumm, and J. Schmiedmayer, *Single-particle-sensitive imaging of freely propagating ultracold atoms*, New Journal of Physics **11** (2009), 103039.

[30] A. M. Kaufman, B. J. Lester, C. M. Reynolds, M. L. Wall, M. Foss-Feig, K. R. A. Hazzard, A. M. Rey, and C. A. Regal, *Two-particle quantum interference in tunnel-coupled optical tweezers*, Science **345** (2014), no. 6194, 306–309. 2, 89

[31] A. Robert, O. Sirjean, A. Browaeys, J. Poupard, S. Nowak, D. Boiron, C. I. Westbrook, and A. Aspect, *A Bose-Einstein condensate of metastable atoms.*, Science **292** (2001), no. 5516, 461–464. 2, 7, 49, 79

[32] F. Pereira Dos Santos, J. Leonard, J. Wang, C. J. Barrelet, F. Perales, E. Rasel, C. S. Unnikrishnan, M. Leduc, and C. Cohen-Tannoudji, *Bose-Einstein condensation of metastable helium.*, Physical Review Letters **86** (2001), no. 16, 3459–3462. 7, 79

[33] W. Vassen, C. Cohen-Tannoudji, M. Leduc, D. Boiron, C. I. Westbrook, K. G. H. Baldwin, and M. Trippenbach, *Cold and trapped metastable noble gases*, Reviews Of Modern Physics **84** (2012), 175–210. 2

[34] T. Jeltes, J. M. McNamara, W. Hogervorst, W. Vassen, V. Krachmalnicoff, A. Perrin, D. Boiron, A. Aspect, and C. I. Westbrook, *Comparison of the Hanbury Brown-Twiss effect for bosons and fermions*, Nature **445** (2007), no. 7, 402–405. 2

[35] S. S. Hodgman, R. G. Dall, A. G. Manning, K. G. H. Baldwin, and A. G. Truscott, *Direct Measurement of Long-Range Third-Order Coherence in Bose-Einstein Condensates*, Science **331** (2011), no. 6020, 1046–1049.

[36] R. Lopes, A. Imanaliev, A. Aspect, M. Cheneau, D. Boiron, and C. I. Westbrook, *Atomic Hong-Ou-Mandel experiment.*, Nature **520** (2015), no. 7545, 66–68. 2, 89

[37] A. J. Ferris, M. K. Olsen, E. G. Cavalcanti, and M. J. Davis, *Detection of continuous variable entanglement without coherent local oscillators*, Physical Review A **78** (2008), no. 6, 060104–1–060104–4. 2

[38] A. J. Ferris, M. K. Olsen, and M. J. Davis, *Atomic entanglement generation and detection via degenerate four-wave mixing of a Bose-Einstein condensate in an optical lattice*, Physical Review A **79** (2009), no. 4, 043634–1–043634–11.

[39] J. Kofler, M. Singh, M. Ebner, M. Keller, M. Kotyrba, and A. Zeilinger, *Einstein-Podolsky-Rosen correlations from colliding Bose-Einstein condensates*, Physical Review A **86** (2012), no. 3, 032115–1–032115–5. 2, 3

[40] Z. Y. Ou, X. Y. Zou, L. J. Wang, and L. Mandel, *Observation of Nonlocal Interference in Separated Photon Channels*, Physical Review Letters **65** (1990), no. 3, 321–324. 2

[41] Z. Y. Ou, S. F. Pereira, H. J. Kimble, and K. C. Peng, *Realization of the Einstein-Podolsky-Rosen Paradox for Continuous Variables*, Physical Review Letters **68** (1992), no. 25, 3663–3666. 2

[42] J. M. Vogels, K. Xu, and W. Ketterle, *Generation of Macroscopic Pair-Correlated Atomic Beams by Four-Wave Mixing in Bose-Einstein Condensates*, Physical Review Letters **89** (2002), no. 2, 020401–1–020401–4. 2

[43] J. M. Vogels, J. K. Chin, and W. Ketterle, *Coherent Collisions between Bose-Einstein Condensates*, Physical Review Letters **90** (2003), no. 3, 030403–1–030403–4. 2

[44] K. V. Kheruntsyan, J.-C. Jaskula, P. Deuar, M. Bonneau, G. B. Partridge, J. Ruaudel, R. Lopes, D. Boiron, and C. I. Westbrook, *Violation of the Cauchy-Schwarz Inequality with Matter Waves*, Physical Review Letters **108** (2012), no. 26, 260401–1–260401–5. 2

[45] M. Ebner, *Development of a metastable helium BEC as a platform for experiments with EPR-entangled matter waves*, Ph.D. thesis, University of Vienna, 2012. 2, 22, 24, 41

[46] J. R. Woodworth and H. W. Moos, *Experimental determination of the single-photon transition rate between the* 2^3S_1 *and* 1^1S_0 *states of He I*, Physical Review A **12** (1975), no. 6, 2455–2463. 3, 5

[47] S. S. Hodgman, R. G. Dall, L. J. Byron, K. G. H. Baldwin, S. J. Buckman, and A. G. Truscott, *Metastable Helium: A New Determination of the Longest Atomic Excited-State Lifetime*, Physical Review Letters **103** (2009), no. 5, 53002. 3, 5, 7

[48] U. Kilian and C. Weber (eds.), *Lexikon der Physik*, Spektrum Akademischer Verlag, 2000. 5

[49] J. E. Sansonetti and W. C. Martin, *Handbook of basic atomic spectroscopic data*, vol. 18, 2006. 6

[50] R. Van Dyck Jr, C. Johnson, and H. Shugart, *Radiative Lifetime of the* 2^1S_0 *Metastable State of Helium*, Physical Review A **4** (1971), 1327. 6

[51] F. M. Penning, *Über Ionisation durch metastabile Atome*, Die Naturwissenschaften **15** (1927), no. 40, 818. 6, 49

[52] N. Herschbach, P. J. J. Tol, W. Hogervorst, and W. Vassen, *Suppression of Penning ionization by spin polarization of cold He(*$2\,^3S$*) atoms*, Physical Review A **61** (2000), no. 5, 050702–1–050702–3. 6

[53] D. C. Morton, Q. Wu, and G. W. Drake, *Energy levels for the stable isotopes of atomic helium(* ^{4}*He I and* ^{3}*He I)*, Can J Phys **84** (2006), no. 2, 83–105. 6

[54] S. Moal, M. Portier, J. Kim, J. Dugué, U. Rapol, M. Leduc, and C. Cohen-Tannoudji, *Accurate Determination of the Scattering Length of Metastable Helium Atoms Using Dark Resonances between Atoms and Exotic Molecules*, Physical Review Letters **96** (2006), no. 2, 023203. 6

[55] R. S. Van Dyck, Jr, S. L. Zafonte, S. Van Liew, and D. B. Pinegar, *Ultraprecise atomic mass measurement of the* α *particle and* ^{4}*He*, Physical Review (2004), 220802–220806. 6

[56] C. C. Bradley, C. A. Sackett, and R. G. Hulet, *Bose-Einstein Condensation of Lithium: Observation of Limited Condensate Number*, Physical Review Letters **78** (1997), no. 6, 985–989. 7

[57] K. Davis, M.-O. Mewes, M. R. Andrews, and N. J. Van Druten, *Bose-Einstein condensation in a gas of sodium atoms*, Physical Review Letters **75** (1995), 3969–3974. 7

[58] G. Modugno, G. Ferrari, G. Roati, R. Brecha, A. Simoni, and M. Inguscio, *Bose-Einstein Condensation of Potassium Atoms by Sympathetic Cooling*, Science **294** (2001), no. 5545, 1320. 7

[59] T. Weber, J. Herbig, M. Mark, H.-C. Nagerl, and R. Grimm, *Bose-Einstein condensation of cesium*, Science **299** (2003), no. 5604, 232–235. 7

[60] S. C. Doret, C. B. Connolly, W. Ketterle, and J. M. Doyle, *Buffer-Gas Cooled Bose-Einstein Condensate*, Physical Review Letters **103** (2009), 103005. 7, 79

[61] G. W. F. Drake, *Theory of Relativistic Magnetic Dipole Transitions: Lifetime of the Metastable* $2\,^3S$ *State of the Heliumlike Ions*, Physical Review A **3** (1971), no. 3, 908–915. 7

[62] H. W. Moos and J. R. Woodworth, *Observation of the Forbidden* $2^3S_1 \rightarrow 1^1S_0$ *Spontaneous Emission Line from Helium and Measurement of the Transition Rate*, Physical Review Letters **30** (1973), no. 17, 775–778. 7

[63] M. Kotyrba, *Metastable-Helium-4 Source For Cold-Atom Experiments*, Master's thesis, University of Vienna, 2010. 7, 10

[64] J. Kawanaka, M. Hagiuda, K. Shimizu, F. Shimizu, and H. Takuma, *Generation of an Intense Low-Velocity Metastable-Neon Atomic Beam*, Applied Physics B **56** (1993), no. 1, 21–24. 7

[65] Y. Raizer, V. Kisin, and J. Allen, *Gas discharge physics*, Springer Berlin Heidelberg, 2011. 8, 18

[66] H. J. Metcalf and P. van der Straten, *Laser cooling and trapping*, Springer-Verlag New York, 1999. 10

[67] R. Stas, J. McNamara, W. Hogervorst, and W. Vassen, *Homonuclear ionizing collisions of laser-cooled metastable helium atoms*, Physical Review A **73** (2006), no. 3, 032713. 10

[68] N. Vansteenkiste, C. Gerz, R. Kaiser, L. Hollberg, C. Salomon, and A. Aspect, *A frequency-stabilized LNA laser at 1083nm: application to the manipulation of helium 4 atoms*, Journal de Physique II **1** (1991), no. 12, 1407–1428. 10, 12

[69] W. Rooijakkers, W. Hogervorst, and W. Vassen, *An intense collimated beam of metastable helium atoms by two-dimensional laser cooling*, Optics Communications **123** (1996), 321–330. 10, 12

[70] G. R. Woestenenk, J. W. Thomsen, M. Van Rijnbach, P. Van Der Straten, and A. Niehaus, *Construction of a low velocity metastable helium atomic beam*, Review of Scientific Instruments **72** (2001), no. 10, 3842–3847. 10

[71] J. Swansson, K. G. H. Baldwin, and M. Hoogerland, *A high flux, liquid-helium cooled source of metastable rare gas atoms*, Applied Physics B **79** (2004), 485–489. 10

[72] A. Aspect, N. Vansteenkiste, R. Kaiser, H. Haberland, and M. Karrais, *Preparation of a pure intense beam of metastable helium by laser cooling*, Chemical Physics **145** (1990), no. 2, 307–315. 12

[73] E. Rasel, F. Dos Santos, F. S. Pavone, F. Perales, C. S. Unnikrishnan, and M. Leduc, *White light transverse cooling of a helium beam*, European Physical Journal D **7** (1999), no. 3, 311–316. 12

[74] W. D. Phillips and H. Metcalf, *Laser Deceleration of an Atomic Beam*, Physical Review Letters **48** (1982), no. 9, 596–599. 13, 14

[75] C. J. Dedman, J. Nes, T. M. Hanna, R. G. Dall, K. G. H. Baldwin, and A. G. Truscott, *Optimum design and construction of a Zeeman slower for use with a magneto-optic trap*, Review of Scientific Instruments **75** (2004), no. 12, 5136–5142. 13, 14, 16

[76] S. Mayer, N. Minarik, M. Shroyer, and D. Mclntyre, *Zeeman-tuned slowing of rubidium using σ^+ and σ^- polarized light*, Optics Communications **210** (2002), no. 3-6, 259–270. 14

[77] E. Courtade, F. Marion, P. J. Nacher, G. Tastevin, K. Kiersnowski, and T. Dohnalik, *Magnetic field effects on the 1083 nm atomic line of helium*, European Physical Journal D **21** (2002), no. 1, 25–55. 14

[78] F. Leupold, *Production of a Slow Metastable Helium Atomic Beam for a BEC*, Master's thesis, Free University of Berlin, 2010. 14, 22

[79] W. Rooijakkers, W. Hogervorst, and W. Vassen, *Laser deceleration and trapping of metastable helium atoms*, Optics Communications **135** (1997), 149–156. 14

[80] C. E. Wieman and T. W. Haensch, *Doppler-Free Laser Polarization Spectroscopy*, Physical Review Letters **36** (1976), no. 20, 1170–1173. 22

[81] C. Pearman, C. Adams, S. Cox, P. Griffin, and D. Smith, *Polarization spectroscopy of a closed atomic transition: applications to laser frequency locking*, Journal of Physics B: Atomic, Molecular and Optical Physics **35** (2002), 5141–5151. 24

[82] Y. Yoshikawa, T. Umeki, T. Mukae, Y. Torii, and T. Kuga, *Frequency stabilization of a laser diode with use of light-induced birefringence in an atomic vapor*, Applied Optics **42** (2003), no. 33, 6645–6649. 24

[83] P. Tol, *Trapping and Evaporative Cooling of Metastable Helium*, Ph.D. thesis, Vrije Universiteit Amsterdam, 2005. 29, 75

[84] B. Gao, *Effects of Zeeman degeneracy on the steady-state properties of an atom interacting with a near-resonant laser field: Analytic results.*, Physical Review A **48** (1993), no. 3, 2443–2448. 29

[85] F. Dalfovo, S. Giorgini, L. Pitaevskii, and S. Stringari, *Theory of Bose-Einstein condensation in trapped gases*, Reviews Of Modern Physics **71** (1999), no. 3, 463–512. 30, 31, 79, 81

[86] Y. Kagan, E. Surkov, and G. Shlyapnikov, *Evolution of a Bose-condensed gas under variations of the confining potential.*, Physical Review A **54** (1996), no. 3, R1753–R1756. 32

[87] Y. Castin and R. Dum, *Bose-Einstein Condensates in Time Dependent Traps*, Physical Review Letters **77** (1996), no. 2, 5315–5319. 32, 81

[88] N. Herschbach, *Trapped triplet helium atoms: Inelastic collisionsand evaporative cooling*, Ph.D. thesis, Vrije Universiteit Amsterdam, 2003. 33

[89] M. Alducin, *Auger deexcitation in a helium atom induced by a metal surface*, Physical Review A **53** (1996), no. 6, 4222. 35

[90] F. Shimizu, K. Shimizu, and H. Takuma, *Double-slit interference with ultracold metastable neon atoms*, Physical Review A **46** (1992), no. 1, R17–R20. 37

[91] J. Lawall and M. Prentiss, *Demonstration of a novel atomic beam splitter*, Physical Review Letters **72** (1994), no. 7, 993–996.

[92] U. Spillmann, O. Jagutzki, L. Spielberger, R. D rner, V. Mergel, K. Ullmann-Pfleger, and H. Schmidt-B cking, *A Novel Delay-Line Anode Design for Position and Time Sensitive Read-Out of MCP-Based Detectors*, Physica Scripta **T92** (2001), no. 1, 225–226.

[93] G. Da Costa, F. Vurpillot, A. Bostel, M. Bouet, and B. Deconihout, *Design of a delay-line position-sensitive detector with improved performance*, Review of Scientific Instruments **76** (2005), no. 1, 3304. 37

[94] O. Jagutzki, V. Mergel, K. Ullmann-Pfleger, L. Spielberger, U. Spillmann, R. Dörner, and H. Schmidt-Böcking, *A broad-application microchannel-plate detector system for advanced particle or photon detection tasks: large area imaging, precise multi-hit timing information and high detection rate*, Nuclear Instruments and Methods in Physics Research Section A: Accelerators, Spectrometers, Detectors and Associated Equipment **477** (2002), no. 1, 244–249. 41

[95] M. Schellekens, *L'effet hanbury brown et twiss pour les atomes froids*, Ph.D. thesis, Université de Paris XI Orsay, 2007. 41, 43, 44

[96] R. G. Dall, L. J. Byron, A. G. Truscott, G. R. Dennis, M. T. Johnsson, and J. J. Hope, *Paired-atom laser beams created via four-wave mixing*, Physical Review A **79** (2009), 11601. 41

[97] S. Hodgman, *Transition Lifetime Measurements and Correlation Experiments with Ultra-cold Metastable Helium*, Ph.D. thesis, Australian National University, 2011. 43

[98] V. Krachmalnicoff, *Deux experiences de correlations quantiques sur des gaz de helium metastable: Degroupement de fermions et etude de paires de bosons correles par collision de condensats*, Ph.D. thesis, Université de Paris XI Orsay, 2009. 44

[99] A. Widl, *In preparation.* 46

[100] A. Tychkov, *Bose-Einstein Condensation of Metastable Helium Atoms*, Ph.D. thesis, Vrije Universiteit Amsterdam, 2006. 46

[101] F. P. D. Santos, F. Perales, J. Leonard, A. Sinatra, J. Wang, F. S. Pavone, E. Rasel, C. S. Unnikrishnan, and M. Leduc, *Efficient magneto-optical trapping of a metastable*

helium gas, The European Physical Journal Applied Physics **14** (2001), no. 1, 69–76. 49

[102] G. Shlyapnikov, J. T. M. Walraven, and U. Rahmanov, *Decay Kinetics and Bose Condensation in a Gas of Spin-Polarized Triplet Helium*, Physical Review Letters **73** (1994), no. 24, 3247–3250. 49, 68

[103] N. Herschbach, P. Tol, A. Tychkov, W. Hogervorst, and W. Vassen, *Magnetic trapping and evaporative cooling of metastable triplet helium*, Journal of Optics B: Quantum and Semiclassical Optics **5** (2003), no. 2, S65–S74. 49

[104] R. G. Dall, C. J. Dedman, and A. G. Truscott, *Feedback control of an atom laser.*, Optics Express **16** (2008), no. 19, 14716–14722. 49

[105] F. Bardou, O. Emile, J. M. Courty, C. I. Westbrook, and A. Aspect, *Magneto-Optical Trapping of Metastable Helium: Collisions in the Presence of Resonant Light*, Europhysics Letters **20** (1992), no. 8, 681–686. 50, 52

[106] M. Kumakura and N. Morita, *Visible Observation of Metastable Helium Atoms Confined in an Infrared/Visible Double Resonance Trap*, Japanese Journal of Applied Physics **31** (1992), no. Part 2, No. 3A, L276–L279.

[107] H. C. Mastwijk, J. W. Thomsen, P. Van Der Straten, and A. Niehaus, *Optical Collisions of Cold, Metastable Helium Atoms*, Physical Review Letters **80** (1998), no. 2, 5516–5519. 50

[108] P. Tol, N. Herschbach, E. A. Hessels, W. Hogervorst, and W. Vassen, *Large numbers of cold metastable helium atoms in a magneto-optical trap*, Physical Review A **60** (1999), no. 2, R761–R764. 54

[109] A. Browaeys, J. Poupard, A. Robert, S. Nowak, W. Rooijakkers, E. Arimondo, L. Marcassa, D. Boiron, C. I. Westbrook, and A. Aspect, *Two body loss rate in a magneto-optical trap of metastable He*, European Physical Journal D **8** (2000), no. 2, 199–203.

[110] F. P. Dos Santos, F. Perales, J. Leonard, A. Sinatra, J. M. Wang, F. S. Pavone, E. Rasel, C. S. Unnikrishnan, and M. Leduc, *Penning collisions of laser-cooled metastable helium atoms*, European Physical Journal D **14** (2001), no. 1, 15–22.

[111] R. J. Stas, J. M. McNamara, W. Hogervorst, and W. Vassen, *Simultaneous Magneto-Optical Trapping of a Boson-Fermion Mixture of Metastable Helium Atoms*, Physical Review Letters **93** (2004), no. 5, 53001. 54

[112] S. D. Gensemer, V. Sanchez-Villicana, K. Tan, T. T. Grove, and P. L. Gould, *Trap-loss collisions of ^{85}Rb and ^{87}Rb: Dependence on trap parameters*, Physical Review A **56** (1997), no. 5, 4055–4063. 54

[113] N. Herschbach, P. Tol, W. Hogervorst, and W. Vassen, *Suppression of Penning ionization by spin polarization of cold He (2^3S) atoms*, Physical Review A (2000), 050702–050705. 54, 67, 68

[114] C. Zener, *Non-Adiabatic Crossing of Energy Levels*, Proceedings of the Royal Society of London Series A, 1932, pp. 696–702. 54, 67

[115] C. Sukumar and D. Brink, *Spin-flip transitions in a magnetic trap*, Physical Review A **56** (1997), no. 3, 2451–2454. 54, 67

[116] W. Petrich, M. H. Anderson, J. R. Ensher, and E. A. Cornell, *Stable, Tightly Confining Magnetic Trap for Evaporative Cooling of Neutral Atoms*, Physical Review Letters **74** (1995), 3352. 54

[117] Y. V. Gott, M. S. Ioffe, and V. G. Telkovskii, *Some new results on confinement in magnetic traps*, Nuclear Fusion (Austria) **Vol: Suppl. 2, Pt. 3** (1962). 54, 67

[118] D. E. Pritchard, *Cooling Neutral Atoms in a Magnetic Trap for Precision Spectroscopy*, Physical Review Letters **51** (1983), no. 15, 1336–1339. 54, 67

[119] M.-O. Mewes, M. R. Andrews, N. J. Van Druten, D. M. Kurn, D. S. Durfee, and W. Ketterle, *Bose-Einstein Condensation in a Tightly Confining dc Magnetic Trap*, Physical Review Letters **77** (1996), no. 3, 416–419. 54

[120] T. Bergeman, G. Erez, and H. Metcalf, *Magnetostatic trapping fields for neutral atoms*, Physical Review A **35** (1987), no. 4, 1535–1546. 56

[121] M. Keller, *In preparation*, Ph.D. thesis, University of Vienna. 66

[122] T. W. Hijmans, O. J. Luiten, I. D. Setija, and J. T. M. Walraven, *Optical cooling of atomic hydrogen in a magnetic trap*, JOSA B: Optical Physics **6** (1989), no. 11, 2235–2243. 70

[123] P. O. Schmidt, S. Hensler, J. Werner, T. Binhammer, A. Görlitz, and T. Pfau, *Doppler cooling of an optically dense cloud of magnetically trapped atoms*, JOSA B: Optical Physics **20** (2003), no. 5, 960–967. 70

[124] O. J. Luiten, M. W. Reynolds, and J. T. M. Walraven, *Kinetic theory of the evaporative cooling of a trapped gas*, Physical Review A **53** (1996), no. 1, 381–389. 72, 73, 75, 91

[125] P. Pinkse, A. Mosk, M. Weidemüller, M. W. Reynolds, T. W. Hijmans, and J. Walraven, *Adiabatically changing the phase-space density of a trapped Bose gas*, Physical Review Letters **78** (1997), no. 6, 990. 72

[126] W. Ketterle and N. J. van Druten, *Evaporative Cooling of Trapped Atoms*, Advances In Atomic, Molelcular, and Optical Physics **37** (1996), 181–236. 73

[127] J. T. M. Walraven, *Atomic hydrogen in magnetostatic traps*, Quantum Dynamics of Simple Systems (G. Oppo, S. Barnett, E. Riis, and M. Wilkinson, eds.), Scottish Graduate Series, Taylor & Francis, 1997. 76

[128] N. Herschbach, P. Tol, A. Tychkov, W. Hogervorst, and W. Vassen, *Magnetic trapping and evaporative cooling of metastable triplet helium*, Jounal of Optics B: Quantum and Semiclassical Optics **5** (2003), 65–74. 73

[129] A. S. Tychkov, T. Jeltes, J. M. McNamara, P. J. J. Tol, N. Herschbach, W. Hogervorst, and W. Vassen, *Metastable helium Bose-Einstein condensate with a large number of atoms*, Physical Review A **73** (2006), no. 3, 31603. 79, 85

[130] R. G. Dall and A. G. Truscott, *Bose–Einstein condensation of metastable helium in a bi-planar quadrupole Ioffe configuration trap*, Optics Communications **270** (2007), no. 2, 255–261.

[131] Q. Bouton, R. Chang, A. L. Hoendervanger, F. Nogrette, A. Aspect, C. I. Westbrook, and D. Clément, *Fast production of Bose-Einstein condensates of metastable Helium*, ArXiv e-prints (2015). 79

[132] I. Bloch, T. W. Hänsch, and T. Esslinger, *Atom laser with a cw output coupler*, Physical Review Letters **82** (1999), no. 15, 3008. 79, 86

[133] C. J. Pethick and H. Smith, *Bose-Einstein Condensation in Dilute Gases*, 2 ed., Cambridge University Press, New York, 2008. 79

[134] L. Pitaevskii and S. Stringari, *Bose-Einstein Condensation*, Oxford University Press, New York, 2003.

[135] Y. Castin, *Bose-einstein condensates in atomic gases: Simple theoretical results*, vol. 72, Springer Berlin Heidelberg, 2001. 79

[136] S. Giorgini, L. Pitaevskii, and S. Stringari, *Condensate fraction and critical temperature of a trapped interacting Bose gas*, Physical Review A **54** (1996), no. 6, R4633–R4636. 79

[137] G. Baym and C. Pethick, *Ground-State Properties of Magnetically Trapped Bose-Condensed Rubidium Gas*, Physical Review Letters **76** (1996), no. 1, 6–9. 79

[138] C. Gardiner, P. Zoller, R. Ballagh, and M. Davis, *Kinetics of Bose-Einstein Condensation in a Trap*, Physical Review Letters **79** (1997), no. 10, 1793–1796. 84

[139] M. Köhl, M. J. Davis, C. W. Gardiner, T. W. Hänsch, and T. Esslinger, *Growth of Bose-Einstein condensates from thermal vapor.*, Physical Review Letters **88** (2002), no. 8, 080402.

[140] S. Seidelin, O. Sirjean, J. V. Gomes, D. Boiron, C. I. Westbrook, and A. Aspect, *Using ion production to monitor the birth and death of a metastable helium Bose–Einstein condensate*, Journal of Optics B: Quantum and Semiclassical Optics **5** (2003), no. 2, S112.

[141] P. Ziń, A. Dragan, S. Charzyński, N. Herschbach, P. Tol, W. Hogervorst, and W. Vassen, *The effect of atomic transfer on the decay of a Bose Einstein condensate*, Journal of Physics B: Atomic, Molecular and Optical Physics **36** (2003), no. 8, L149–L154. 84

[142] E. A. Burt, R. W. Ghrist, C. J. Myatt, M. J. Holland, E. A. Cornell, and C. E. Wieman, *Coherence, Correlations, and Collisions: What One Learns about Bose-Einstein Condensates from Their Decay*, Physical Review Letters **79** (1997), no. 3, 337–340. 84

[143] R. J. Lewis-Swan and K. V. Kheruntsyan, *Proposal for demonstrating the Hong-Ou-Mandel effect with matter waves.*, Nature Communications **5** (2014), 3752. 89

[144] R. Colella, A. W. Overhauser, and S. A. Werner, *Observation of Gravitationally Induced Quantum Interference*, Physical Review Letters **34** (1975), no. 23, 1472–1474. 90

[145] M. Kasevich and S. Chu, *Atomic interferometry using stimulated Raman transitions*, Physical Review Letters **67** (1991), no. 2, 181–184. 90

[146] R. Fickler, R. Lapkiewicz, W. N. Plick, M. Krenn, C. Schaeff, S. Ramelow, and A. Zeilinger, *Quantum Entanglement of High Angular Momenta*, Science **338** (2012), no. 6107, 640–643. 90

[147] M. Andersen, C. Ryu, P. Cladé, V. Natarajan, A. Vaziri, K. Helmerson, and W. Phillips, *Quantized Rotation of Atoms from Photons with Orbital Angular Momentum*, Physical Review Letters **97** (2006), no. 17, 170406. 90

[148] W. Ketterle and S. Inouye, *Does Matter Wave Amplification Work for Fermions?*, Physical Review Letters **86** (2001), no. 19, 4203–4206. 90

[149] M. Moore and P. Meystre, *Atomic Four-Wave Mixing: Fermions versus Bosons*, Physical Review Letters **86** (2001), no. 19, 4199–4202. 90

Curriculum Vitae

Personal Information

Name:	Mateusz Leon Kotyrba

Education

Jun. 15	PhD in Physics, "Bose-Einstein condensation of metastable helium-4 for quantum entanglement experiments"
Feb. 10	MSc in Physics, "Metastable-Helium-4 Source For Cold-Atom Experiments"
Oct. 08	BSc in Physics, "Experimental investigation of Faraday effect in rubidium vapour"
Sep. 08 – Jun. 15	University of Vienna, Austria
Oct. 04 – Jul. 08	Jagiellonian University of Cracow, Poland

Miscellaneous

2015	Fellowship of the Sohmen Foundation
Jan. 15 – Apr. 2015	Visiting scientist at the Massachusetts Institute of Technology (MIT), Cambridge, USA
Sep. 2013	Organiser of the "CoQuS Summer School 2013"
Sep. 10 – Jun. 15	Teaching of diverse laboratory courses and exercises
Sep. 10 – Jun. 15	Fellow of the Doctoral Program on Complex Quantum Systems "CoQuS" (FWF)